

UC Santa Barbara

UC Santa Barbara Electronic Theses and Dissertations

Title

Mechanical and Biophysical Characterization of Structural Low-Complexity Marine Proteins

Permalink

<https://escholarship.org/uc/item/30z824hh>

Author

Wonderly, William Ruyle

Publication Date

2021

Peer reviewed|Thesis/dissertation

UNIVERSITY OF CALIFORNIA

Santa Barbara

**Mechanical and Biophysical Characterization of Structural Low-
Complexity Marine Proteins**

A dissertation submitted in partial satisfaction of the
requirements for the degree Doctor of Philosophy

in

Chemistry

by

William Ruyle Wonderly

Committee in charge:

Professor J. Herbert Waite, Chair

Professor Daniel E. Morse

Professor Joan-Emma Shea

Professor Javier Read de Alaniz

December 2021

The dissertation of William Ruyle Wonderly is approved.

Daniel E. Morse

Joan-Emma Shea

Javier Read de Alaniz

J. Herbert Waite, Committee Chair

December, 2021

Mechanical and Biophysical Characterization of Low-Complexity Marine Proteins

Copyright © 2021

by

William Ruyle Wonderly

ACKNOWLEDGEMENTS

I am grateful for every person I have met along the way – they all shaped who I am.

Thank you to my parents, Richard and Theresa, whose steadfast love and support has seen me through the many challenges I have faced.

Thank you, Danny, Katie, and their 5 children, for providing me a surrogate family in California.

Thank you to the members of Waite lab and those who are Waite lab adjacent: Eric (who will always be Ricky to me), Dariya, Marcela, Brad, Rubayn, Emma, Wei Wei, Dusty, Qiang, Razieh, Matt M., Menaka, Hong, and any others that I have forgotten for putting up with me during difficult times and always providing me with friendship. Similarly, I want to thank my housemates and wonderful friends Matt, Peter, Jeremy, Dan, and Greg.

Thank you to my committee for your valuable time and input.

Finally, thank you Herb. My time in your lab has been full of growth, both pleasant and painful. Words fail me to express my admiration and gratitude to you, either in a way that is accurately descriptive or effectively convincing.

WILLIAM RUYLE WONDERLY

Curriculum Vitae

EDUCATION

- Ph.D., Chemistry** Expected: Aug 2021
University of California, Santa Barbara (UCSB)
Advisor: Dr. Herb Waite
Dissertation: Mechanical and biophysical characterization of low-complexity marine proteins
- B.A., Mathematics and Chemistry, *summa cum laude*** June 2012
University of Puget Sound, Tacoma, Washington (UPS)
Thesis: Synthesis and phase behavior of oxadiazole based liquid crystals with a lateral fluorine substituent

HONORS AND AWARDS

- Phi Beta Kappa (Honors Society) member
Peter Wallerich Scholarship, UCSB
2008
Sprenger Science Award, UPS
2009
ACS Undergraduate Award in Analytical Chemistry
2010
ACS Student Affiliate Award for Outstanding Graduating Chemistry Major
2012
University of California Regents Special Fellowship 2013 - 2015

TEACHING EXPERIENCE

- Teaching Assistant, Department of Chemistry, UCSB** 2013 - 2021
Courses: General, Organic, Physical Chemistry, Introduction to Biology, Pharmacology Lab
- Department Tutor, Dept. of Chemistry, University of Puget Sound** 2011 - 2012
Tutored 10+ students weekly on various STEM topics
- Course Assistant, University of Puget Sound** 2011 - 2012
Courses: General & Physical Chemistry

PUBLICATIONS AND PRESENTATIONS

- **Wonderly, W. R.***; Cristiani, T. R.*; Cunha, K. C.*; Degen, G. D.; Shea, J. E.; Waite, J. H. Dueling Backbones: Comparing Peptoid and Peptide Analogues of a Mussel Adhesive Protein. *Macromolecules* **2020**, 53 (16), 6767–6779. *Authors contributed equally <https://doi.org/10.1021/acs.macromol.9b02715>.
- Gordon Research Conference on Bioinspired Materials; Melanin fibers inspired by *Glycera* jaws; Poster, June 2018
- The Society for Integrative & Comparative Biology Annual Meeting; *Between the Melanin Nanosheets with a Naked Polychaete*; Talk, January 2018
- Pinelo, L. F.; Klotz, E. R.; **Wonderly, W. R.**; Paulson, L. O.; Kettwich, S. C.; Kubelka, J.; Anderson, D. T. Solid Parahydrogen Infrared Matrix Isolation and Computational Studies of $\text{Li}_n\text{-(C}_2\text{H}_4)_m$ Complexes. *J. Phys. Chem. A* **2018**, 122 (4), 985–991.

<https://doi.org/10.1021/acs.jpca.7b11223>.

- Morales, D. P.; **Wonderly, W. R.**; Huang, X.; McAdams, M.; Chron, A. B.; Reich, N. O. Affinity-Based Assembly of Peptides on Plasmonic Nanoparticles Delivered Intracellularly with Light Activated Control. *Bioconjug. Chem.* **2017**, 28 (7), 1816–1820. <https://doi.org/10.1021/acs.bioconjchem.7b00276>.
- Nguyen, J.; **Wonderly, W.R.**; Tauscher, T.; Harkins, R.; Vita, F.; Portale, G.; Francescangeli, O.; Samulski, E. T.; Scharrer, E. The Effects of Lateral Halogen Substituents on the Low-Temperature Cybotactic Nematic Phase in Oxadiazole Based Bent-Core Liquid Crystals. *Liq. Cryst.* **2015**, 42 (12), 1754–1764. <https://doi.org/10.1080/02678292.2015.1085599>.
- **Wonderly, W. R.**; Anderson, D. T. Reactions of Atomic Hydrogen with Formic Acid and Carbon Monoxide in Solid Parahydrogen II: Deuterated Reaction Studies. *J. Phys. Chem. A* **2014**, 118 (36), 7653–7662. <https://doi.org/10.1021/jp502469p>.
- ACS National Conference in San Diego, CA; *Synthesis and Analysis of Halogen Containing Oxadiazole Based Liquid Crystals*; Poster, March 2012
- **Wonderly, W. R.**; Anderson, D. T. Transient HDO Rovibrational Satellite Peaks in Solid Parahydrogen: Evidence of Hydrogen Atoms or Vacancies? *Low Temp. Phys.* **2012**, 38 (8), 673–678. <https://doi.org/10.1063/1.4743736>.
- Kufeld, K. A.; **Wonderly, W. R.**; Paulson, L. O.; Kettwich, S. C.; Anderson, D. T. Transient H₂O Infrared Satellite Peaks Produced in UV Irradiated Formic Acid Doped Solid Parahydrogen. *J. Phys. Chem. Lett.* **2012**, 3 (3), 342–347. <https://doi.org/10.1021/jz201646a>.

Manuscripts In Preparation

- **Wonderly, W. R.***; Najafi, S; Areyano, M.; Shea, J. E.; Waite, J. H.; DeMartini, D.G. Mechanical Behavior of Octopus Egg Tethers Composed of Topologically Constrained EGF-Domains
- **Wonderly, W. R.***; Nguyen, T; Malollari, K.; DeMartini, D.G.; Delparastan, P.; Valois, E.; Messersmith P.B.; Helgeson, M; Waite, J. H. A multi-tasking polypeptide from bloodworm jaws: catalyst, template, and copolymer in film formation
- **Wonderly, W.R.**; Waite J.H.; Saranathan, V. Photonic crystal skin in the polychaete worm *Lumbrineris* sp.

ABSTRACT

Mechanical and Biophysical Characterization of Structural Low-Complexity Marine Proteins

by

William Ruyle Wonderly

Natural materials are often endowed with enviable properties and understanding the mechanisms from which these properties originate yields both fascinating fundamental science and crucial information for successful bioinspired engineering. Protein building blocks of natural materials are a principal source of bioinspiration and can be understood as sequence-specific polymers that come together to form complex 3-dimensional structures in order to serve a vast array of functions. Although the complexity of sequence and structure in typical folded proteins make bioinspired design challenging, there are examples of highly functional proteins whose sequences are extremely biased or repetitive, which may lead to simpler translation synthetically.

This work investigates the biochemical, molecular, and mechanical properties of proteins from three such load-bearing materials from marine organisms. In the first example from mussel holdfasts, the mechanical effects of the protein backbone are investigated by comparing the adhesive response of a series of low-complexity mussel-derived peptides with their poly-*N*-substituted glycine analogs, otherwise known as peptoids. The peptoids exhibit strikingly different surface deposition behavior, as they form dehydrated monolayers rather

than the hydrated multilayers formed by polypeptides. There is also divergent adhesive behavior, which we propose arises primarily from the differences in film hydration.

In the second, the major polymeric component of the lightweight, melanized, and wear-resistant jaws of *Glycera dibranchiata* is identified as a 22kDa protein dominated by two amino acids: 50% glycine and 30% histidine. We name it MultiTasking Protein (MTP) for the number of functions it displays *in vitro*. MTP shows high capacity Cu^{2+} binding, which in turn, triggers liquid-liquid phase separation. Phase separation also leads to the formation of viscous film at the air-water interface. We find that when this process co-occurs with melanin biogenesis, the films become more elastic than viscous, hence provide some insight into how *Glycera* jaws are formed *in situ*.

Third, the hitherto overlooked protective eggcase threads of *Octopus bimaculoides* are subjected to biochemical and mechanical analyses. The threads have a fibrous internal structure and are primarily composed of a single cystine-rich protein. This protein, which we name octovafibrin (octopus ovarian fibrous protein), is characterized by C-type lectin binding domains at the N- and C-termini, with core of 27 repeat epidermal growth factor (EGF)-like domains. Tensile testing reveals behavior akin to semicrystalline elastomers, and the experiments indicate the mechanical response is mediated by fiber rearrangement as well as distortion of the EGF-like domains.

Each study provides the groundwork for further inquiry and the basis for future low-complexity bioinspired synthetic mimics.

TABLE OF CONTENTS

<i>Chapter 1. Introduction</i>	1
A. Overview	1
B. Biomimetics	2
C. Low complexity proteins	3
D. Biological strengthening strategies	6
i. Non-covalent interactions	6
ii. Inorganic reinforcement.....	8
iii. Covalent crosslinking.....	10
E. Model system background	13
i. Marine mussel byssus	13
ii. Bloodworm jaws	18
iii. Octopus reproductive egg cases.....	21
G. Research outline	23
H. References	24
<i>Chapter 2: The effect of the protein backbone on mussel protein adhesion</i>	34
A. Abstract	34
B. Introduction	34
C. Materials & Methods	38
i. Materials.....	38
ii. Submonomer syntheses.....	38
iii. Peptoid synthesis.....	40
iv. Peptoid modification	40

v. Surface Forces Apparatus Measurements	41
vi. Molecular Dynamics Simulations	42
vii. Circular Dichroism.....	45
D. Results.....	45
i. Peptoid Design and Synthesis	45
ii. SFA Measurements	46
iii. Molecular Dynamics.....	51
D. Discussion	56
E. Conclusion	65
F. References.....	66
G. Supplemental figures for Chapter 2	71
<i>Chapter 3. The glycine/histidine rich structural polypeptide of Glycera jaws</i>	<i>80</i>
A. Abstract	80
B. Introduction	80
C. Materials & Methods	82
i. Amino acid analysis	82
ii. Transcriptome generation and assembly.....	82
iii. Validation with polymerase chain reaction and molecular cloning.....	83
iv. Recombinant protein expression and purification.....	84
v. Isothermal titration calorimetry.....	85
vi. Continuous wave electron paramagnetic resonance	85
vii. Cryogenic TEM.....	86
viii. Catechol oxidase activity assay	86
ix. Mass spectrometry	86
x. Film growth and fiber drawing.....	87

xi. Alkaline peroxide degradation and melanin quantification	87
xii. Scanning Electron Microscopy	88
xiii. Interfacial rheometry	88
xiv. Atomic force microscopy	89
xv. Tensile testing	89
C. Results.....	89
i. <i>Glycera</i> jaws, transcriptome, and protein sequence.....	89
ii. MTP structure and copper binding.....	92
iii. Structure of the Cu-MTP complex.....	94
iv. MTP coacervation	94
v. Dopa oxidation	96
vi. Interfacial assembly and viscoelasticity.....	97
vii. Fiber drawing and mechanics	100
D. Discussion	101
E. Conclusion	103
F. References.....	104
G. Supplemental figures for Chapter 3	108
<i>Chapter 4. The biochemistry and mechanics of octopus egg cases</i>	<i>112</i>
A. Abstract	112
B. Introduction	112
C. Materials & Methods	115
i. Egg thread collection and microscopy	115
ii. Biochemical analysis.....	117
iii. Mechanical testing	119
iv. Transparency measurements	119

v. Wide angle X-ray scattering.....	120
vi. Molecular modeling	120
D. Results.....	121
i. Specimen description	121
ii. Biochemical characterization.....	123
iii. Mechanical properties.....	126
E. Discussion	132
F. Conclusion	137
G. References	139
H. Supplementary figures for Chapter 4	143
<i>Chapter 5. Conclusions, future directions, and closing remarks.....</i>	<i>147</i>
A. Mussel adhesion.....	147
B. <i>Glycera</i> jaw	149
C. Octopus eggs	153
D. Final remarks.....	156
E. References.....	157

LIST OF FIGURES

Figure 2.1 Peptoid chemistry and experimental SFA setup	37
Figure 2.2 Adhesive and cohesive forces of peptoids and peptides	46
Figure 2.3 Representative force curves of peptoids.....	49
Figure 2.4 Effect of ionic strength on Dopa peptoid adhesion	51
Figure 2.5 REMD simulations of peptoid and peptide conformation	53
Figure 2.6 REMD simulations of hydrogen bonding	55
Figure 2.7 Model depicting peptoid adhesion vs. cohesion.....	64
Figure 2.S1 Compression and separation force curves for bare mica	71
Figure 2.S2 Compression force vs. distance profiles of asymmetrically deposited peptide.....	71
Figure 2.S3 Second and third most representative conformations of peptides and peptoids.....	72
Figure 2.S4 Peptoid secondary structure in presence of mica over time.....	73
Figure 2.S5 Number of peptoid residues adopting secondary structure in water and on mica.....	74
Figure 2.S6 Circular dichroism of Phe-peptide	75
Figure 2.S7 Circular dichroism of Tyr-peptide	75
Figure 2.S8 Phenolic hydrogen bonding	76
Figure 2.S9 Snapshots of the 3 most representative conformations on mica	77
Figure 2.S10 2D distribution of the radius R_g vs. R_{max}	78
Figure 2.S11 Dopa interaction with mica	79
Figure 3.1 Structure and protein analysis of <i>Glycera</i> jaw	91

Figure 3.2 <i>In vitro</i> characterization of copper binding to MTP.....	93
Figure 3.3 Copper induced coacervate phase transition	95
Figure 3.4 Oxidative properties of copper bound MTP.....	97
Figure 3.5 Interfacial activity of MTP and film formation.....	98
Figure 3.6 Interfacial film formation enables fiber drawing	101
Figure 3.7 Possible modes of MTP melanization depending on Dopa partitioning	102
Figure 3.S1 Solution conformation of MTP as a function of pH	108
Figure 3.S2 Copper dependence of MTP solution conformation	108
Figure 3.S3 Cryo-TEM of MTP in the absence of Cu ²⁺	109
Figure 3.S4 Time course of MTP-melanin monitored by SDS-PAGE	109
Figure 3.S5 Determination of melanin degradation products.....	110
Figure 3.S6 Observation of MTP-Melanin film under a light microscope.....	110
Figure 3.S7 SEM image of an MTP-melanin film	111
Figure 4.1 The EGF domain	114
Figure 4.2 Dissecting microscope images of <i>Octopus bimaculoides</i> eggs.....	121
Figure 4.3 Electron Microscopy images of octopus eggs.....	122
Figure 4.4 Sequence, structure, and modelling of octovafibrin.....	125
Figure 4.5 Mechanics and optical changes of threads under tensile loading.....	126
Figure 4.6 WAXS analysis of pristine and strained octopus threads	129
Figure 4.7 Mechanical effects of disulfide reduction	130
Figure 4.8 Cartoon model depicting molecular rearrangement and deformation during strain	135
Figure 4.S1 Identification and molecular weight determination of octovafibrin	143

Figure 4.S2 Typical characteristics of octopus threads	144
Figure 4.S3 Effect of EGTA treatment on the tensile behavior of threads.....	145
Figure 4.S4 Recovery of octopus threads	145
Figure 4.S5 Cyclic loading to increasing strain and stress relaxation of threads	146
Figure 5.1 Transcriptome sequence of a second glycine/histidine rich protein from <i>Glycera</i> jaws	151

LIST OF TABLES

Table 2.S1 Secondary structure predictions of the Phe and Tyr peptides	75
Table 2.S2 Numbers of clusters of likely conformation formed	76
Table 4.1 LC/MS/MS sequences of tryptic octovafibrin peptides	123
Table 4.2 Average toughness and hysteresis values of octopus threads.....	127

Chapter 1

Introduction

A. Overview

Biological materials have envios mechanical properties while utilizing a relatively small subset of all available materials. Biomimetics is an approach that investigates the material, design and/or processing conditions used by natural systems and leverages that knowledge to improve synthetic materials. One difficulty with the biomimetic approach is that nature can generate significantly more complex materials that humans are able to engineer. The ability of biology to synthesize large, sequence-specific polymers (proteins) is one example of currently unachievable biological complexity.

Fortunately, many proteins used in load-bearing applications are of low complexity or have seemingly random or highly repetitive sequences. This clear advantage afforded by discovering and investigating these types of proteins over more complex systems because low complexity are reminiscent of synthetic random or block copolymers. Collagen is perhaps the most extensively characterized low complexity protein and illustrates how fruitful the biomimetic approach can be.

The biological materials generated by these proteins achieve their materials properties through one, or a combination of, three broad mechanisms: non-covalent interactions, inorganic reinforcement, or covalent crosslinking.

Three systems composed of low complexity proteins that utilize these mechanisms to varying degrees are: the adhesive plaque proteins of marine mussels, bloodworm (*Glycera dibranchiata*) jaws, and the reproductive egg cases of the California two-spot octopus

(*Octopus bimaculoides*). Background to each of these systems as well as an outline of the research in this is provided.

B. Biomimetics

Biomimetics is an approach to technological progress that looks to nature for inspiration on how to respond to the ever-present need for creating new materials as well as improving processing techniques. It can additionally inform on ways of producing materials in a more efficient, cost effective, and sustainable manner because nature uses renewable materials that are processed under mild conditions. Furthermore, the structure they produce have optimized material properties that were developed over generations of adaptations in response to environmental pressures.

One feature often found in these systems is structural ordering at multiple length scales (structural hierarchy). This feature is responsible for their phenomenal mechanical properties, which, when density is taken into account, rival the performance of the highest performing man-made materials.¹

The fundamental structural polymers utilized by biological organisms for creating extracellular, load-bearing, materials are generally limited to proteins and polysaccharides.¹ To generate the final materials, these building blocks self-assemble into complex architectures with structural hierarchy over multiple length scales. Often, the proteins or polysaccharides can represent the bulk material of the structure, as with keratinous materials like horns and hooves.² At the opposite end of the spectrum, they can provide a template for the deposition for other materials, as is the case in the mineralization of abalone shells³ and sea sponge

spicules.⁴ In many cases the proteins, polysaccharides, and minerals come together to form complex composite systems as in the exoskeletons of crabs.⁵

One difficulty of biomimetics is the current lack of synthetic tools to synthesize large, sequence-specific polymers rapidly, at a large scale, and in a cost-effective manner. From a synthetic perspective, therefore, it is advantageous to look to protein systems that are of highly repetitive or of low complexity because they have similar characteristics to random or block copolymers. Fortunately, there are several examples of load-bearing proteins like this featured in biology. Among the most widely known are collagen, silk fibroin, and elastin.

C. Low complexity proteins

There is no single satisfactory definition of low complexity proteins. Attempts to provide one usually consider three general characteristics.⁶ The first is by the frequency distribution of the amino acids they use. In a low complexity protein, this distribution is skewed away from the “typical” distribution, meaning certain amino acids are present at an abnormally high rate. Unfortunately, there are no set standards for how skewed the composition must be for it to be considered low complexity. A second definition deals with the presence of repetitive sequences. Depending on the nature of the repeat sequence, this definition can overlap with the first. If the protein sequence is very short (the extreme case being a homo-repeat) the resulting sequence composition will be extremely biased. However, long structural repeats, which can be on the order of 50 residues in length,⁷ may or may not generate significant compositional bias. The third general description is based on protein structure. Although many low complexity proteins take on a random coil conformation certain structures can be formed as a result of biased content (such as a charged single α -helix⁸) or

repeat motifs (such as coiled coils⁹). The definition based on structure is, in effect, a result of the sequence. For this reason, we take “low complexity” to imply compositional bias or a high degree of repetition in the sequence.

The fact that many low complexity sequences have been found to be highly functional calls into question the traditional view that function is provided by a specific folded architecture, which is a result of a high complexity protein sequence. The fact that many hereditary diseases are linked to an increase in the number of repeat units of low complexity regions of proteins exemplifies their function.¹⁰ Also, low complexity regions of proteins are suggested to drive the important liquid-liquid phase separation events in cells.¹¹ This principle in particular has been used to engineer phase separating materials.¹² Other critical functions attributed to low complexity proteins include adhesion,¹³ molecular movement,¹⁴ and membrane interactions.¹⁵ Perhaps the most important and thoroughly characterized low complexity protein is collagen.

Collagens are a fundamental family of proteins that appear in all multicellular organisms. Indeed, collagen is the most abundant protein in mammals, constituting ~30% of all proteins by mass.¹⁶ Collagen is one of the oldest proteins detected, having been found in fossil specimens dated to the Jurassic period.¹⁷ The primary sequence of collagen is defined by the Gly-X-Y repeat sequence, where Gly is glycine, X is typically proline, and Y is typically hydroxyproline.¹⁸ For human collagen, this results in ~30% of the residues being glycine and ~22% either proline or hydroxyproline.¹⁹

There are at least 28 different types of collagens described in vertebrates,²⁰ designated by Roman numerals I-XXVIII, that are distinguished by their higher order structures and functions. All collagens take on a triple-helical ultrastructure.²¹ The Gly-X-Y repeat sequence

results in the individual molecules taking on left-handed polyproline II helices. Three molecules then assemble into a right-handed triple helix. Then, from this trimeric building block, collagens assemble to form a diverse set of hierarchical structures.

In rat tendon, for example, five type I collagen molecules assemble into a right handed “super twisted” microfibril, which further assemble in a quasi-hexagonal fashion.²² Type IV collagen uses end to end interactions to assemble into hexamers and generate the interlaced network of the glomerular basement membrane of kidneys.²³ Other assemblies include beaded fibrils of type VI collagen²⁴ and geometric arrays of types VIII and X collagen.²⁵

Even more impressive are the wide variety of functions collagen displays. Fibril forming collagens play a mechanical role in tissues, such as providing tensile strength to skin and ligaments²⁰ as well as contributing to the mechanical properties and mineralization of bone and teeth.²⁶ Additionally, collagens have been shown to participate in cell signaling, adhesion, organ development, and tissue repair.²⁷ Finally, collagens even assemble into complex arrays resulting in structural color.²⁸

Thus, the simple sequence, paired with the extensive scientific understanding of the structure and function of collagen, has led to numerous applications of collagen biomimetics. These applications include, but are not limited to, mineralization,²⁹ wound healing,³⁰ drug delivery,³¹ and tissue engineering.^{32,33}

While collagen may be the most well-known example, other low complexity proteins have yielded fruitful foundational and translational research. Two examples that have been reviewed extensively are the poly-alanine and Gly-rich regions of silk fibroin³⁴⁻³⁶ and the VPGXG repeats of elastin.³⁷⁻³⁹

The presence of low complexity proteins in load-bearing biological systems are only part of the equation to generate impressive materials properties. Although nature generates a wide range of apparently different materials the underlying molecular mechanisms responsible for providing structural support are often similar. Most of these mechanisms can be generally described as non-covalent interactions, inorganic reinforcement, or covalent crosslinking.

D. Biological strengthening strategies

i. Non-covalent interactions

Many load bearing protein systems utilize non-covalent interactions to bear load and dissipate energy. This approach is fundamentally tied to protein folding, as these non-covalent interactions are also what stabilize a proteins secondary and tertiary structure. Features of a protein's secondary structure, such as α -helices and β -sheets, are stabilized by intramolecular hydrogen bonds formed between amide hydrogens and carbonyl groups that are intrinsic to the protein backbone. In addition, the hydrophobic effect, the burial of hydrophobic residues in the core of a folded protein, plays an important role in protein folding and stability. A result of this is an increase in entropy because the hydrophobic residues are shielded from water molecules that would otherwise aggregate and order themselves around those residues. In this process the hydrophobic residues also accumulate a significant amount of van der Waals interactions that provide enthalpic stabilization.

The protein responsible for the mechanical properties of muscles, Titin, utilizes this approach. Titin exhibits excellent toughness due to the numerous (~300) folded immunoglobulin (Ig) and fibronectin-3 (Fn3) domains. These domains unfold when subjected

to load, meaning the intermolecular interactions stabilizing their β -sheets are broken which has the effect of dissipating energy.⁴⁰ Numerous single-molecule studies have shown the domains sequentially unfold to produce the characteristic sawtooth force-extension pattern.⁴¹ Non proteinaceous systems, such as cellulose⁴² can also be strengthened by extensive hydrogen bonding networks.

Nonpolar intermolecular interactions can also have dramatic effects on the mechanical properties of a biological material. Spider silks proteins, as mentioned previously, contain low-complexity alanine- and glycine-rich regions that form β -sheet crystallites. Increased alanine content is correlated to improved mechanical properties of the silks as a result of interactions between β -sheets mediated by hydrophobic alanine residues.⁴³

Many biological materials tailor their mechanical properties by altering the hydration of their load bearing structures. This principle is exquisitely expressed in the hardened beaks of Humboldt squid. Squid beaks are very robust, with hardness and modulus values exceeding those of most industrial polymers.⁴⁴ They are composites of chitin, proteins, low molecular weight catechols, and water, each of which are deposited in a gradient fashion. Perhaps unsurprisingly, many of the proteins involved in the beak are of low complexity, with glycine, alanine, and histidine rich domains.⁴⁵ Perhaps the most impressive aspect of squid beaks is the mechanical gradient they form to interface the very hard beak tip with the much softer (~200 times less stiff) tissue at the base of the beak.

Although significant crosslinking is present in squid beaks, the primary driver of this transition appears to be, in fact, water content. This explanation is confirmed by the fact that freeze-dried beaks have nearly uniform mechanical properties.⁴⁶ Beak dehydration is likely achieved both through the incorporation of catechols⁴⁷ as well as protein coacervation.⁴⁵ The

underlying reason linking dehydration and stiffness in squid beaks is unclear but similar observations relating catechols, crosslinks, dehydration, and mechanical properties have been made in insect cuticles.⁴⁸⁻⁵¹ The dehydration-based explanation is that the removal of water facilitates denser packing resulting in stronger intermolecular interactions.⁵² For insect cuticles, however, there are substantive arguments that the mechanical properties arise from the crosslinks themselves and will be discussed later.

ii. Inorganic reinforcement

A diverse number of organisms incorporate inorganic materials to reinforce their load-bearing structures. This process can be broadly divided into two approaches: mineralization and metallization.

The incorporation of minerals into biological structures has been extensively studied and is generally referred to as biomineralization. In biomineralization cellular structures deposit proteins which, in turn, induce and template the precipitation of minerals. In these structures, minerals are responsible for the hardness and stiffness, whereas the presence of proteins provides toughness.⁵³ One of the most famous examples of biomineralization are the nacreous layers of mollusk shells.

Nacre is composed of ~95% calcium carbonate and ~5% of the mass is attributed to an organic matrix of macromolecules. It has a “brick and mortar” architecture where “bricks” of 5-15 μm aragonitic CaCO_3 tablets held together by thin (~0.5 μm) “mortar” which is viscoelastic organic matrix⁵⁴ that is at partially responsible for the templating and growth of the mineral phase.⁵⁵

The major organic components in nacre are chitin and a suite of proteins, many of which are appropriately of low complexity. In general, the proteins are differentiated by their solubility in EDTA. The major protein components of the insoluble fraction, which comprises the material in between aragonite tablets, are rich in alanine and glycine residues and bear close resemblance to the low complexity domains of silk fibroin.⁵⁶ The soluble proteins, on the other hand, are present within the mineralized tablets and are characterized by low complexity sequences rich in acidic residues like aspartate.⁵⁷

The presence of the organic matrix in biomineralized tissues can have profound effects on their mechanical properties. In nacre, the presence of the organic layer between aragonite tablets are necessary to reduce the brittleness and provide fracture toughness 3-4 orders of magnitude greater than aragonite alone.⁵⁸ The toughening is afforded by the interstitial organic layers which alter crack propagation by various mechanisms including crack blunting, microcrack formation, crack bridging, or inducing pull out of the plates.^{59,60} In a similar fashion, the organic components of bone provide toughening mechanisms to the otherwise brittle hydroxyapatite.⁶¹

The other process, metallization, occurs when natural structures incorporate metal ions to improve their mechanical properties, providing increased toughness.⁶² The incorporation of metal ions into a material induces in the formation of metal coordinate bonds. These bonds form when ligands, which in proteins are typically aspartate, glutamate, or histidine (His) residues, donate electrons to the metal cation. The advantages of metal coordinate bonds, discussed by Degtyar, *et al.*,⁶³ include their intermediate bond strength, reversibility, and their sensitivity to stimuli such as pH. These characteristics are exemplified to varying degrees by different metallized biological structures.

Marine mussels use metal coordinate bonds to increase the toughness of their byssal threads. The collagenous molecules that make up the bulk of the threads have flanking His-rich regions that facilitate the formation of a network of metal-coordinate crosslinks by binding to Cu, Zn, and Ni ions. These metal coordination sites act as sacrificial bonds and break under strain. This dissipates energy and, because metal coordinate bonds are stronger than hydrogen bonds, relatively few are needed to create a significant effect. Furthermore, the reversibility of these bonds allows for self-healing properties.

The jaws of the marine worm *Nereis virens* are assemblies of His-rich proteins reinforced with Zn^{2+} ions. Regions with high Zn^{2+} content have significantly higher hardness and modulus values.⁶⁴ In the case of *Nereis* jaws, treatment with ethylene diamine tetraacetic acid (EDTA) successfully removes the Zn^{2+} ions, yielding a softer material. In addition, subsequent incubation with zinc chloride successfully reversed this process. Although there is no specific mechanism by which Zn^{2+} hardens this material, similar correlations are observed in spider fangs⁶⁵ suggesting it is a broadly applicable strategy. Furthermore, this strategy was used to improve the mechanical performance of imidazole containing polymers.⁶⁶

iii. Covalent crosslinking

The final strategy to discuss is covalent crosslinking. Covalent bonds, the sharing of electrons between two atoms, are also the strongest of the interactions discussed so far. Covalent crosslinking is then the formation of a covalent bond between polymer chain sections, the result of which is a 3-dimensional network. The introduction of crosslinks to these systems generally has the effect of increasing chemical stability as well as the materials

mechanical properties, but often at the expense of reduced extensibility.^{67,68} This strategy is utilized across nearly all of biology.

Invertebrate arthropod cuticles have proven to be very rich systems for the study of biological crosslinking. The cuticle generally refers to the outermost layers of an insect's exoskeleton and fulfills critical functions. In addition to preventing water loss, the cuticle facilitates locomotion and provides a hard shell for defense. Thus, the mechanical properties of insect cuticles are highly tunable with Young's modulus values ranging from 1kPa to 20 GPa,⁶⁹ which is all the more impressive given their low density. Like the squid beak, insect cuticles are composed of chitin, proteins, low molecular weight catechols, and water. Although dehydration was previously mentioned as a major factor in the hardening of these structures, the predominant theory is that the mechanical properties are a result of crosslink formation.

Crosslinking in insect cuticles is thought to be effected by the incorporation of the precursor catechols *N*-acetyldopamine (NADA) and *N*- β -Alanyldopamine (NBAD).⁷⁰ The catechol groups in these molecules are readily oxidized leading to the formation highly reactive quinone methide intermediates that can rapidly react with nucleophilic groups to create crosslinks. The most experimental evidence shows crosslinks form with histidine and lysine residues, but there is also evidence glycine, alanine, and tyrosine can participate.^{71,72} In addition, solid state NMR indicates both the formation of catechol-catechol crosslinks⁷³ as well as catechol mediated protein-chitin interactions.⁷⁴

Crosslinking is also an important aspect of vertebrate protein mechanics. For example it is essential to the mechanical resilience of collagen fibrils.²⁷ In fibrous collagens, most crosslinking is facilitated by lysyl oxidase, which converts the amine groups of lysine into

aldehydes, that then can spontaneously react with aldehydes or amine groups on adjacent fibrils.⁷⁵ These crosslinks then facilitate the transmission of force between fibrils to distribute load and prevent slippage.²² Collagen can contain other types of crosslinks, such as disulfide bonds in type VI collagen.⁷⁶ Interestingly, invertebrate collagens can utilize dramatically different chemistry, such as dityrosine crosslinks in cuticular collagen of *Caenorhabditis elegans*.⁷⁷ Others still, such as cuticular collagen of *Nereis virent*, apparently lack crosslinks and likely need to rely on extensive glycosylation and enormous molecular weight (1.5 MDa).⁷⁸

Finally, crosslinking is important for the function of bacteria as well as plants. Bacterial cell walls, which define cell shape and provide mechanical support, crosslinks large polysaccharide chains with short peptides.⁷⁹ Plant cell walls bear some similarity to insect cuticles in that they use phenolic compounds to form an aromatic network (lignin) with crosslinks to polysaccharides and glycoproteins. The chemistry in this process is extremely complex and reviewed elsewhere.⁸⁰

With the relationships between bioinspired design, low complexity proteins, and post-translational hardening mechanisms outlined, the advantages of characterizing such systems are clear. Brief introductions are provided for the three systems investigated in this thesis: the adhesive proteins of the marine mussel byssus, the sclerotized jaws of the bloodworm, and the viscoelastic egg case of octopuses.

E. Model system background

i. Marine mussel byssus

The intertidal zone, i.e. the area of beach covered by the ocean at high tide and exposed by low tide, is home to a large diversity of life. There are many advantages to living in this area: the waves constantly both replenish nutrients and remove waste, while abundant sunlight allows for the growth of ample vegetation. At the same time life in the intertidal zone has disadvantages: the organisms must be able to tolerate the potential of dehydration/rehydration cycles, they may need to be able to defend against both marine and terrestrial predators, and the waves generate constant lift and drag threatening the dislodgement of one's home. Marine mussels are one organism that has successfully adapted to this environment.

Mussels are bivalves, meaning they are equipped with two hard, mineralized shells meeting at a hinge. This geometry allows the shells to open and enable filter feeding, but also clamp shut to stay hydrated at low tide as well as provide defense. Mussels have also developed a holdfast, referred to as the byssus, to mediate adhesion to a substrate in a wet environment as well as mitigate mechanical forces imparted by wave action. As a model system, the mussel byssus has provided inspiration for strategies to form strong adhesive interactions in the presence of foulants such as liquids, salts, biofilms, and general corrosion. Most of the research into the byssus has focused on the two extra-shellular components of the byssus: 1) the threads, which, at the proximal end fuse together in a stem and root themselves in tissue of the mussel, whereas at the distal end they interface with 2) the adhesive plaque, which interacts with the substrate.

Mussel threads exhibit amazing mechanical properties. Most importantly they have a high modulus of 500MPa and can extend to over twice their initial length. These properties combine to create a material with a toughness of 45MJ/m³ – similar to that of Kevlar.⁸¹ Ultrastructurally, threads are composed of a fibrous core that is surrounded by a stiff outer cuticle. The core is a semicrystalline assembly of collagenous proteins embedded in a separate viscoelastic matrix. The collagenous proteins, referred to as preCols, are particularly intriguing in that they are a fusion of three low complexity domains. For example, the preCol localized to the distal region of threads has a central collagenous domain flanked on either side by silk-like domains and His-rich domains at the C- and N-termini.⁸² The matrix is composed of Thread Matrix Protein (TMP), which is identified by two von Willebrand factor type A domains and may play a role in the assembly, stability, and interconnectivity of the preCols.⁸³

The cuticle has distinct two-phase architecture where granular structures are embedded in an amorphous matrix. The cuticle has been implicated in energy dissipation⁸⁴ as well as self-healing properties.⁸⁵ The granules are understood to be condensates of mussel foot protein (mfp-1) bound to iron.⁸⁶ Mfp-1 is a large repetitive protein whose features vary between species, but generally is rich in tyrosine that are often converted to 3,4-dihydroxyphenylalanine (Dopa), proline that are often converted to *trans*-4-hydroxyproline or *trans*-2,3-*cis*-3,4-dihydroxyproline, and lysine.⁸⁷ Currently, the composition of the amorphous matrix is unclear. The most recent work suggests that the granular structures are much softer and more effectively retain water during drying cycles than the matrix material, allowing the granules to provide necessary plasticity and deformability and prevent

embrittlement.⁸⁸ Recently, a thiol-rich layer has been characterized between the cuticle and core that both mediates their mechanical interaction and prevent oxidation.⁸⁹

The adhesive plaques have a spatulate shape and their internal architecture is foam-like. The cuticle forms a continuous coat with the plaques, but the transition from tread to plaque is marked by penetration of collagen fibers into the foamy architecture. Two proteins appear to be unique to the core of the plaque.⁹⁰ Mussel foot protein-2 (mfp-2) is an abundant protein whose sequence is defined by 11 epidermal growth factor (EGF) domain repeats and thought to make up the plaque core. Mussel foot protein-4 (mfp-4) is primarily localized to the thread-plaque interface and, by virtue of a sequence rich in histidine, is hypothesized to bridge interactions between the preCols and the plaque.⁹¹

Perhaps the most celebrated characteristic of mussel plaques is their ability to form strong adhesive interactions with a variety of substrates. Three proteins have been localized to the plaque-substrate interface.⁹² The most abundant interfacial protein is mussel foot protein-3 (mfp-3). Mfp-3 represents a group of small (5-7.5kDa) proteins that can be subdivided into *fast* (mfp-3f) and *slow* (mfp-3s) families based on their electrophoretic mobility.⁹³ Both families are low complexity being composed almost entirely of glycine, asparagine, tryptophan, and lysine. Tyrosine and asparagine residues are also extensively modified to form Dopa and 4-hydroxyarginine, respectively. Depending on the variant, each of these moieties can represent up to 20% of the total protein sequence.⁹⁴ The low complexity sequence results in a disordered solution structure⁹⁵ which becomes more ordered when exposed to hydrophobic surfaces⁹⁶ or high pH.⁹⁷

Mussel foot protein-5 (mfp-5) is also a relatively small (9kDa) and relatively low in abundance when compared to mfp-3.⁹² It has a sequence strongly biased toward glycine,

lysine, tyrosine, and serine. Additionally, most tyrosine are modified to Dopa and most serine are phosphorylated.⁹⁸ The isolation of mfp-5 has proven to be difficult meaning much less is known about its secondary structure. The relatively high glycine content would suggest intrinsic disorder, although it is probable that it can form surface and solution dependent structures like mfp-3.

The third known protein present at the interface is mussel foot protein-6 (mfp-6). Of the three interfacial proteins, mfp-6 is the largest at ~11.5 kDa. It similarly displays sequence bias towards lysine, tyrosine, and glycine, but differs in that it has few Dopa modifications and has significant (~11 mol%) cysteine content, most of which are present in this protein as thiols.⁹⁹

Experiments with the surface forces apparatus (SFA) have elucidated the adhesive capabilities and mechanisms of the interfacial proteins. Although films of mfp-3 generate significant adhesion energies¹⁰⁰ of -2.5 mJ/m², mfp-5 is considered the champion of adhesion, yielding adhesion energies in excess of -13mJ/m².¹⁰¹ To put this in context, this value surpasses that of biotin-streptavidin, a ligand-receptor pair known very high binding energy.¹⁰² Partly based on the observation that adhesion energy of these proteins appears to be correlated with Dopa content,¹⁰³ many of the mechanisms put forth to explain their adhesion have relied on Dopa's multifunctionality.

Indeed, single-molecule atomic force microscopy (AFM) experiments showed that, when bound to metal oxide surfaces, a catechol moiety can reversibly register pull-off forces in excess of 500pN.¹⁰⁴ This study, along with later SFA investigations, revealed that Dopa can facilitate reversible adhesion through the formation of metal coordination bonds¹⁰⁵ and bidentate hydrogen bonds.¹⁰⁶ All of this led to many synthetic mussel-inspired polymers that

largely rely on catechol incorporation. However, few of these have proven to be successful because they represent an oversimplification of mussel adhesion, reducing it to the presence of catechol groups.

One critical aspect often overlooked are the redox properties of Dopa. Dopa is extremely sensitive to oxidation, which can be brought about by either exposure to alkaline pH, or by the addition of an oxidizing agent such as sodium periodate. Catechol groups oxidize to form quinones, which are unable to form the same stable coordination bonds or act as hydrogen bond donors. Quinones do, however, allow for rapid covalent crosslinking which may affect cohesion.¹⁰¹ The importance of redox chemistry is highlighted by the fact that the maximum adhesion values for the mfp's are achieved at low pH. Modulating redox behavior is the main responsibility of mfp-6. Thiols in mfp-6 act as a reservoir of electrons that can be used to rescue oxidized Dopa moieties¹⁰⁷ and recover adhesion.¹⁰⁰

Further studies have investigated the role other characteristics may play in adhesion. One key contributor is the presence of lysine, whose charged ammonium group displaces hydrated surface cations to enable Dopa-surface interactions.¹⁰⁸ Coacervation, a phenomenon in which macromolecules undergo liquid-liquid phase separation, is also an important strategy utilized by mussels. Mussel-derived coacervates are shown to have high polymer/protein concentration while maintaining low viscosity which facilitates material transport through cellular architectures.¹⁰⁹ They are generally denser than water and have low surface energy indicating their surface coating ability.¹¹⁰ Recently, mfp-3 and -6 were shown to coacervate and act in symphony to keep mfp-5 reduced.¹¹¹

Mussel adhesion is a complex process meaning there are many more avenues left undiscussed here, and even more left to pursue that can provide a clearer picture of how these organisms create maintain their robust holdfast.

ii. Bloodworm jaws

Glycera dibranchiata is a marine polychaete worm. It is equipped with an eversible proboscis that has four black jaws used to grasp, bite, and inject venom. They are colloquially known as bloodworms due to their red appearance and are commonly used as bait for saltwater fishing. They are most frequently encountered in the muddy sediment of the intertidal zone, where they burrow through the sand and mud to scavenge for food and to stay hidden from possible predators.

Glycera jaws need to be mechanically robust enough to puncture the integument of its victim. It is highly likely that *Glycera* uses its proboscis as a tool to propagate cracks through the sediment to facilitate movement and form its burrow, in a fashion similar to the closely related *Hemipodia simplex*.¹¹² Doing so means that the jaws must be resistant to constant exposure to the abrasion from the surrounding sediment. As a result, there has been significant interest in the structure, composition, and mechanical properties of *Glycera* jaws.

Jaw mechanical properties

Initial studies characterizing the composition of *Glycera* jaws detected that approximately half of the dry mass of the jaws is represented by proteins¹¹³ whose average amino acid composition is dominated by glycine (~60%) and histidine (~24%).¹¹⁴ In addition to protein, the jaws were found to contain a chemically robust material that is resistant to

treatment with acid¹¹⁵ or base.¹¹⁶ Finally, copper was detected at an unusually high level of 2.5% by mass.¹¹⁵

It was the presence of copper that led to groundbreaking study characterizing the structure and mechanical properties of *Glycera* jaws.¹¹⁷ The copper was shown to be mineralized in the rare form of polycrystalline atacamite ($\text{Cu}_2(\text{Cl}(\text{OH})_3)$) fibers primarily localized to the jaw tips. Nanoindentation measurements revealed the jaws have average hardness (H) and elastic modulus (E) values of 1.11 GPa and 15.16 GPa, respectively. Furthermore, when using the quantity H^3/E^2 as an indicator, they indicate the jaws have impressive wear resistance.¹¹⁸ Using this metric *Glycera* jaws appear to have comparable wear resistance properties to dentin and enamel⁴⁴ despite only being sparsely mineralized. These realizations led to a number of studies to further investigate the mechanical, biochemical, and ultrastructural properties of *Glycera* jaws.

Moses, *et al*, showed that after being subjected to extensive hydrolysis in 6M HCl jaws are reduced to ~40% of their initial mass but only shrink to 85% of their original volume. Also, the residue left behind maintains the black coloration and shape of the jaws. Through a combination of infrared (IR) spectroscopy, solid state ^{13}C -NMR resonance, and laser desorption ionization time of flight mass spectroscopy, the chemically robust black residue that comprises nearly 40% of the jaw mass was identified, surprisingly, as melanin.¹¹⁹ This study also used TEM to show that the melanin is deposited as 200 nm thick sheets that are orthogonally arranged to the long axis of the jaw. Given that natural melanin is synthesized as a dispersion of sub micrometer particles,¹²⁰ the presence of melanin at the length scale of the jaw (millimeters) is unprecedented. *Glycera* jaws appear to be the only organism known

to utilize melanin as a load-bearing material, aside from possibly certain fungi whose cell walls contain melanin.¹²¹

These observations laid the groundwork for a series of studies^{122–124} characterizing the individual mechanical contributions of melanin and copper to the jaws. After hydrolysis, the jaws retain hardness and modulus values approximately half that of untreated jaws,¹²² which confirms that melanin provides a robust mechanical framework. Moreover, scratch test analyses on jaw cross-sections showed that there is a strong relationship between the mechanical properties and the presence of copper ions.¹²³ The authors discovered that there are thin (several microns) layers rich in copper ions flanking the mineralized layers of the jaw that display the best wear resistance. The presence of atacamite mineral diminished the hardness and modulus of the jaw, and the worst properties were found in the core of the jaw which is devoid of either copper ions or mineral.

One glaring question that remains is regarding the protein component of the jaw. As mentioned before, amino acid analysis indicates that protein comprises ~40% of the dry weight of the jaws and that the protein fraction is rich in glycine (~60%) and histidine (~30%). Preliminary work indicated the presence of a ~30kDa protein of low complexity, containing high levels of Gly (~40%) and His (~20%), but yields were insufficient for direct sequencing.¹²⁵ Indeed, previous work showed that the protein component is tightly bound to the melanin component, and that this is most likely facilitated through the histidine residues which are resistant to liberation via hydrolysis.¹²⁶

The interest in the protein was further stoked by the discovery of the major structural protein (Nvjp-1) in *Nereis virens* jaws.¹²⁷ Nvjp-1 was found to have a sequence rich in glycine (36%) and histidine (27%) that, upon binding to zinc, forms β -sheet structures and assembles

into amyloid-like fibrils. However, there are significant differences between *Glycera* and *Nereis* jaws. Primarily, *Nereis* jaws do not feature any melanin content and secondly *Nereis* jaws are completely unmineralized and utilize zinc rather than copper ions. Thus, numerous questions regarding the sequence, structure, and function of the *Glycera* jaw protein in both the jaw synthesis and mechanics remain.

iii. Octopus reproductive egg cases

Egg cases can perform a diverse array of functions including protecting against environmental factors such as predation,¹²⁸ desiccation,¹²⁹ mechanical disruption¹³⁰ and microbial fouling¹³¹ in addition to providing guidance to the developing embryo.¹³² Therefore, studies on the encasements used by oviparous (egg laying) animals have the potential to inform on strategies to engineer fibrous scaffolds for biomedical applications.

The California two spot octopus (*Octopus bimaculoides*) is one potential model system. They are incirrate octopuses native to the Pacific Ocean that encase their developing progeny in protective egg cases. Octopus reproduction begins when the male octopus deposits sperm packets into the oviducal gland of the female octopus, where they are stored until the female octopus decides to lay her eggs. Then, eggs are released from the ovary of the octopus whereupon they travel through the proximal oviduct before reaching the oviducal gland. There, they are fertilized and coated in a secretion before travelling through the distal oviduct and exiting the mother. The source of the egg case protein is either the embryo itself or the oviducal gland.¹³³ The egg has an elongated ovoid shape that is equipped with a 3-5cm long thread on one end. The eggs are then fitted to a central cement stalk and attached to a substrate. The mother octopus then tends to her eggs for the remainder of her life, a processes that can

take over a year.¹³⁴ Very little is known regarding the biochemistry or mechanics of this material, only that egg cases of similar species, *Octopus vulgaris*, have a fibrous internal structure.¹³⁵ Fruitful work on other fibrous egg capsules provides encouragement for studying this system.

Praying mantis offer one example as they protect their eggs by secreting a hardened protein mass called the ootheca. The ootheca is composed of coiled-coil proteins that assemble into a highly ordered helicoidal structure.^{136,137} This system has provided insights into liquid-crystalline assembly and were found to be hardened *via* a combination of hydrogen bonding and covalent crosslinking.¹³⁸ Recombinant proteins derived from Praying mantis were also used as design templates for fabricating biomimetic materials.¹³⁹

The egg capsules of marine snails (whelks) have also proven to be a fascinating system. They are proteinaceous and form a tough, multilaminate, elastomeric material in that it that exhibits high extensibility, hysteresis, and rapid strain recovery which, taken together, indicates its ability to act as a shock absorber.¹³⁰ Laminae are constructed of fibers that are, in turn, assemblies of proteins with coiled-coil structures.¹⁴⁰ The material behavior of whelk egg capsules is interesting because unlike other typical elastomers its behavior is *not* governed by entropic factors.¹⁴¹ Instead, as the material is strained the coiled-coil proteins undergo a transition from α -helix to β -sheet that dissipates energy and is also rapidly reversible. This provides a novel approach to the design of impact absorbing materials. Thus, there are important gaps in knowledge surrounding the octopus egg capsules, particularly with regards to the molecular composition and basic mechanical properties.

G. Research outline

The research in this dissertation is designed to understand key components of each model system outlined in the previous section.

First, the difficulty in translating principles ascertained from studying mussel adhesion into synthetic systems leads to the question: is the protein backbone itself a contributor to the behavior of mfps? To answer this question adhesion testing and molecular dynamics simulations are performed on a set of sequence-specific peptidomimic molecules based on mussel peptides. The results are then compared to results derived from their peptide analogs. Understanding this can be extended to inform on potential backbone effects in other intrinsically disordered proteins.

Second, the identity of the low-complexity protein utilized in the jaws of *Glycera dibranchiata* is identified. Furthermore, *in vitro* characterization of recombinant protein illustrates its multifunctional nature.

Third, the reproductive egg threads from *Octopus bimaculoides* are characterized. In particular, the major structural protein is identified both *in situ* and *in silico*, the internal structure is described, and the tensile behavior measured.

Finally, a summary of conclusions is presented along with future directions of study.

H. References

- (1) Vincent, J. F. V. Biomimetics - A Review. *Proc. Inst. Mech. Eng. Part H J. Eng. Med.* **2009**, *223* (8), 919–939. <https://doi.org/10.1243/09544119JEIM561>.
- (2) McKittrick, J.; Chen, P. Y.; Bodde, S. G.; Yang, W.; Novitskaya, E. E.; Meyers, M. A. The Structure, Functions, and Mechanical Properties of Keratin. *Jom* **2012**, *64* (4), 449–468. <https://doi.org/10.1007/s11837-012-0302-8>.
- (3) Belcher, A. M.; Wu, X. H.; Christensen, R. J.; Hansma, P. K.; Stucky, G. D.; Morse, D. E. Control of Crystal Phase Switching and Orientation by Soluble Mollusc-Shell Proteins. *Nature* **1996**, *381* (6577), 56–58. <https://doi.org/10.1038/381056a0>.
- (4) Weaver, J. C.; Morse, D. E. Molecular Biology of Demosponge Axial Filaments and Their Roles in Biosilicification. *Microsc. Res. Tech.* **2003**, *62* (4), 356–367. <https://doi.org/10.1002/jemt.10401>.
- (5) Andersen, S. O. Exoskeletal Proteins from the Crab, Cancer Pagurus. *Comp. Biochem. Physiol. - A Mol. Integr. Physiol.* **1999**, *123* (2), 203–211. [https://doi.org/10.1016/S1095-6433\(99\)00051-3](https://doi.org/10.1016/S1095-6433(99)00051-3).
- (6) Mier, P.; Paladin, L.; Tamana, S.; Petrosian, S.; Hajdu-Soltész, B.; Urbanek, A.; Gruca, A.; Plewczynski, D.; Grynberg, M.; Bernadó, P.; Gáspári, Z.; Ouzounis, C. A.; Promponas, V. J.; Kajava, A. V.; Hancock, J. M.; Tosatto, S. C. E.; Dosztanyi, Z.; Andrade-Navarro, M. A. Disentangling the Complexity of Low Complexity Proteins - THESISINTRO. *Brief. Bioinform.* **2020**, *21* (2), 458–472. <https://doi.org/10.1093/bib/bbz007>.
- (7) Kajava, A. V. Tandem Repeats in Proteins: From Sequence to Structure. *Journal of Structural Biology.* 2012, pp 279–288. <https://doi.org/10.1016/j.jsb.2011.08.009>.
- (8) Knight, P. J.; Thirumurugan, K.; Xu, Y.; Wang, F.; Kalverda, A. P.; Stafford, W. F.; Sellers, J. R.; Peckham, M. The Predicted Coiled-Coil Domain of Myosin 10 Forms a Novel Elongated Domain That Lengthens the Head. *J. Biol. Chem.* **2005**, *280* (41), 34702–34708. <https://doi.org/10.1074/jbc.M504887200>.
- (9) Lupas, A. N.; Bassler, J. Coiled Coils – A Model System for the 21st Century. *Trends Biochem. Sci.* **2017**, *42* (2), 130–140. <https://doi.org/10.1016/j.tibs.2016.10.007>.
- (10) Mirkin, S. M. Expandable DNA Repeats and Human Disease. *Nature* **2007**, *447* (7147), 932–940. <https://doi.org/10.1038/nature05977>.
- (11) Martin, E. W.; Mittag, T. Relationship of Sequence and Phase Separation in Protein Low-Complexity Regions. *Biochemistry* **2018**, *57* (17), 2478–2487. <https://doi.org/10.1021/acs.biochem.8b00008>.
- (12) Cui, M.; Wang, X.; An, B.; Zhang, C.; Gui, X.; Li, K.; Li, Y.; Ge, P.; Zhang, J.; Liu, C.; Zhong, C. Exploiting Mammalian Low-Complexity Domains for Liquid-Liquid Phase Separation–Driven Underwater Adhesive Coatings. *Sci. Adv.* **2019**, *5* (8), 1–13. <https://doi.org/10.1126/sciadv.aax3155>.
- (13) So, C. R.; Fears, K. P.; Leary, D. H.; Scancella, J. M.; Wang, Z.; Liu, J. L.; Orihuela, B.; Rittschof, D.; Spillmann, C. M.; Wahl, K. J. Sequence Basis of Barnacle Cement Nanostructure Is Defined by Proteins with Silk Homology. *Sci. Rep.* **2016**, *6*, 1–14. <https://doi.org/10.1038/srep36219>.
- (14) Brewer, S.; Tolley, M.; Trayer, I. P.; Barr, G. C.; Dorman, C. J.; Hannavy, K.; Higgins, C. F.; Evans, J. S.; Levine, B. A.; Wormald, M. R. Structure and Function of X-Pro Dipeptide Repeats in the TonB Proteins of *Salmonella Typhimurium* and

- Escherichia Coli. *J. Mol. Biol.* **1990**, *216* (4), 883–895.
[https://doi.org/10.1016/S0022-2836\(99\)80008-4](https://doi.org/10.1016/S0022-2836(99)80008-4).
- (15) Robison, A. D.; Sun, S.; Poyton, M. F.; Johnson, G. A.; Pellois, J. P.; Jungwirth, P.; Vazdar, M.; Cremer, P. S. Polyarginine Interacts More Strongly and Cooperatively than Polylysine with Phospholipid Bilayers. *J. Phys. Chem. B* **2016**, *120* (35), 9287–9296. <https://doi.org/10.1021/acs.jpcc.6b05604>.
- (16) Ricard-Blum, S. The Collagen Family. *Cold Spring Harb. Perspect. Biol.* **2011**, *3* (1), 1–19. <https://doi.org/10.1101/cshperspect.a004978>.
- (17) Lee, Y. C.; Chiang, C. C.; Huang, P. Y.; Chung, C. Y.; Huang, T. D.; Wang, C. C.; Chen, C. I.; Chang, R. S.; Liao, C. H.; Reisz, R. R. Evidence of Preserved Collagen in an Early Jurassic Sauropodomorph Dinosaur Revealed by Synchrotron FTIR Microspectroscopy. *Nat. Commun.* **2017**, *8*, 2–9.
<https://doi.org/10.1038/ncomms14220>.
- (18) Shoulders, M. D.; Raines, R. T. Collagen Structure and Stability. *Annu. Rev. Biochem.* **2009**, *78*, 929–958.
<https://doi.org/10.1146/annurev.biochem.77.032207.120833>.
- (19) Ramshaw, J. A. M.; Shah, N. K.; Brodsky, B. Gly-X-Y Tripeptide Frequencies in Collagen: A Context for Host-Guest Triple-Helical Peptides. *J. Struct. Biol.* **1998**, *122* (1–2), 86–91. <https://doi.org/10.1006/jsbi.1998.3977>.
- (20) Kadler, K. E.; Baldock, C.; Bella, J.; Boot-Handford, R. P. Collagens at a Glance. *J. Cell Sci.* **2007**, *120* (12), 1955–1958. <https://doi.org/10.1242/jcs.03453>.
- (21) Brodsky, B.; Ramshaw, J. A. M. The Collagen Triple-Helix Structure. *Matrix Biol.* **1997**, *15* (8–9), 545–554. [https://doi.org/10.1016/S0945-053X\(97\)90030-5](https://doi.org/10.1016/S0945-053X(97)90030-5).
- (22) Orgel, J. P. R. O.; Irving, T. C.; Miller, A.; Wess, T. J. Microfibrillar Structure of Type I Collagen in Situ. *Proc. Natl. Acad. Sci. U. S. A.* **2006**, *103* (24), 9001–9005.
<https://doi.org/10.1073/pnas.0502718103>.
- (23) Naylor, R. W.; Morais, M. R. P. T.; Lennon, R. Complexities of the Glomerular Basement Membrane. *Nat. Rev. Nephrol.* **2021**, *17* (2), 112–127.
<https://doi.org/10.1038/s41581-020-0329-y>.
- (24) Lampe, A. K.; Bushby, K. M. D. Collagen VI Related Muscle Disorders. *J. Med. Genet.* **2005**, *42* (9), 673–685. <https://doi.org/10.1136/jmg.2002.002311>.
- (25) Knupp, C.; Squire, J. M. Molecular Packing in Network-Forming Collagens. *ScientificWorldJournal.* **2003**, *3*, 558–577. <https://doi.org/10.1100/tsw.2003.40>.
- (26) Knott, L.; Bailey, A. J. Collagen Cross-Links in Mineralizing Tissues: A Review of Their Chemistry, Function, and Clinical Relevance. *Bone* **1998**, *22* (3), 181–187.
[https://doi.org/10.1016/S8756-3282\(97\)00279-2](https://doi.org/10.1016/S8756-3282(97)00279-2).
- (27) Gelse, K.; Pöschl, E.; Aigner, T. Collagens - Structure, Function, and Biosynthesis. *Adv. Drug Deliv. Rev.* **2003**, *55* (12), 1531–1546.
<https://doi.org/10.1016/j.addr.2003.08.002>.
- (28) Prum, R. O.; Torres, R. H. Structural Colouration of Mammalian Skin: Convergent Evolution of Coherently Scattering Dermal Collagen Arrays. *J. Exp. Biol.* **2004**, *207* (12), 2157–2172. <https://doi.org/10.1242/jeb.00989>.
- (29) Gu, L.; Kim, Y. K.; Liu, Y.; Ryou, H.; Wimmer, C. E.; Dai, L.; Arola, D. D.; Looney, S. W.; Pashley, D. H.; Tay, F. R. Biomimetic Analogs for Collagen Biomineralization. *J. Dent. Res.* **2011**, *90* (1), 82–87.
<https://doi.org/10.1177/0022034510385241>.

- (30) Chattopadhyay, S.; Raines, R. T. Review Collagen-Based Biomaterials for Wound Healing. *Biopolymers* **2014**, *101* (8), 821–833. <https://doi.org/10.1002/bip.22486>.
- (31) Friess, W. Collagen - Biomaterial for Drug Delivery. *Eur. J. Pharm. Biopharm.* **1998**, *45* (2), 113–136. [https://doi.org/10.1016/S0939-6411\(98\)00017-4](https://doi.org/10.1016/S0939-6411(98)00017-4).
- (32) Woolfson, D. N. Building Fibrous Biomaterials from Alpha-Helical and Collagen-like Coiled-Coil Peptides. *Biopolymers* **2010**, *94* (1), 118–127. <https://doi.org/10.1002/bip.21345>.
- (33) Cen, L.; Liu, W.; Cui, L.; Zhang, W.; Cao, Y. Collagen Tissue Engineering: Development of Novel Biomaterials and Applications. *Pediatr. Res.* **2008**, *63* (5), 492–496. <https://doi.org/10.1203/PDR.0b013e31816c5bc3>.
- (34) Widhe, M.; Johansson, J.; Hedhammar, M.; Rising, A. Invited Review: Current Progress and Limitations of Spider Silk for Biomedical Applications. *Biopolymers* **2012**, *97* (6), 468–478. <https://doi.org/10.1002/bip.21715>.
- (35) López Barreiro, D.; Yeo, J.; Tarakanova, A.; Martin-Martinez, F. J.; Buehler, M. J. Multiscale Modeling of Silk and Silk-Based Biomaterials—A Review. *Macromol. Biosci.* **2019**, *19* (3), 1–9. <https://doi.org/10.1002/mabi.201800253>.
- (36) Lefèvre, T.; Auger, M. Spider Silk as a Blueprint for Greener Materials: A Review. *Int. Mater. Rev.* **2016**, *61* (2), 127–153. <https://doi.org/10.1080/09506608.2016.1148894>.
- (37) Simnick, A. J.; Lim, D. W.; Chow, D.; Chilkoti, A. Biomedical and Biotechnological Applications of Elastin-like Polypeptides. *Polym. Rev.* **2007**, *47* (1), 121–154. <https://doi.org/10.1080/15583720601109594>.
- (38) Varanko, A. K.; Su, J. C.; Chilkoti, A. Elastin-Like Polypeptides for Biomedical Applications. *Annu. Rev. Biomed. Eng.* **2020**, *22*, 343–369. <https://doi.org/10.1146/annurev-bioeng-092419-061127>.
- (39) Saxena, R.; Nanjan, M. J. Elastin-like Polypeptides and Their Applications in Anticancer Drug Delivery Systems: A Review. *Drug Deliv.* **2015**, *22* (2), 156–167. <https://doi.org/10.3109/10717544.2013.853210>.
- (40) Tskhovrebova, L.; Trinick, J.; Sleep, J. A.; Simmons, R. M. Elasticity and Unfolding of Single Molecules of the Giant Muscle Protein Titin. *Nature* **1997**, *387* (6630), 308–312. <https://doi.org/10.1038/387308a0>.
- (41) Oberhauser, A. F.; Hansma, P. K.; Carrion-Vazquez, M.; Fernandez, J. M. Stepwise Unfolding of Titin under Force-Clamp Atomic Force Microscopy. *Proc. Natl. Acad. Sci. U. S. A.* **2001**, *98* (2), 468–472. <https://doi.org/10.1073/pnas.98.2.468>.
- (42) Meyers, M. A.; Chen, P. Y.; Lin, A. Y. M.; Seki, Y. Biological Materials: Structure and Mechanical Properties. *Prog. Mater. Sci.* **2008**, *53* (1), 1–206. <https://doi.org/10.1016/j.pmatsci.2007.05.002>.
- (43) Hayashi, C. Y.; Shipley, N. H.; Lewis, R. V. Hypotheses That Correlate the Sequence, Structure, and Mechanical Properties of Spider Silk Proteins. *Int. J. Biol. Macromol.* **1999**, *24* (2–3), 271–275. [https://doi.org/10.1016/S0141-8130\(98\)00089-0](https://doi.org/10.1016/S0141-8130(98)00089-0).
- (44) Broomell, C. C.; Khan, R. K.; Moses, D. N.; Miserez, A.; Pontin, M. G.; Stucky, G. D.; Zok, F. W.; Waite, J. H. Mineral Minimization in Nature’s Alternative Teeth. *J. R. Soc. Interface* **2007**, *4* (12), 19–31. <https://doi.org/10.1098/rsif.2006.0153>.
- (45) Tan, Y.; Hoon, S.; Guerette, P. A.; Wei, W.; Ghadban, A.; Hao, C.; Miserez, A.; Waite, J. H. Infiltration of Chitin by Protein Coacervates Defines the Squid Beak

- Mechanical Gradient. *Nat. Chem. Biol.* **2015**, *11* (7), 488–495.
<https://doi.org/10.1038/nchembio.1833>.
- (46) Miserez, A.; Schneberk, T.; Sun, C.; Zok, F. W.; Waite, J. H. The Transition from Stiff to Compliant Materials in Squid Beaks. *Science (80-.)*. **2008**, *319* (5871), 1816–1819. <https://doi.org/10.1126/science.1154117>.
- (47) Miserez, A.; Rubin, D.; Waite, J. H. Cross-Linking Chemistry of Squid Beak. *J. Biol. Chem.* **2010**, *285* (49), 38115–38124. <https://doi.org/10.1074/jbc.M110.161174>.
- (48) Klocke, D.; Schmitz, H. Water as a Major Modulator of the Mechanical Properties of Insect Cuticle. *Acta Biomater.* **2011**, *7* (7), 2935–2942.
<https://doi.org/10.1016/j.actbio.2011.04.004>.
- (49) Dirks, J. H.; Taylor, D. Fracture Toughness of Locust Cuticle. *J. Exp. Biol.* **2012**, *215* (9), 1502–1508. <https://doi.org/10.1242/jeb.068221>.
- (50) Barbakadze, N.; Enders, S.; Gorb, S.; Arzt, E. Local Mechanical Properties of the Head Articulation Cuticle in the Beetle *Pachnoda Marginata* (Coleoptera, Scarabaeidae). *J. Exp. Biol.* **2006**, *209* (4), 722–730.
<https://doi.org/10.1242/jeb.02065>.
- (51) Vincent, J. F. V. Arthropod Cuticle: A Natural Composite Shell System. *Compos. Part A Appl. Sci. Manuf.* **2002**, *33* (10), 1311–1315. [https://doi.org/10.1016/S1359-835X\(02\)00167-7](https://doi.org/10.1016/S1359-835X(02)00167-7).
- (52) Hillerton, J. E.; Vincent, J. F. V. The Stabilisation of Insect Cuticles. *J. Insect Physiol.* **1979**, *25* (12). [https://doi.org/10.1016/0022-1910\(79\)90109-4](https://doi.org/10.1016/0022-1910(79)90109-4).
- (53) Zhang, N.; Chen, Y. Molecular Origin of the Sawtooth Behavior and the Toughness of Nacre. *Mater. Sci. Eng. C* **2012**, *32* (6), 1542–1547.
<https://doi.org/10.1016/j.msec.2012.04.040>.
- (54) Ji, B.; Gao, H. Mechanical Properties of Nanostructure of Biological Materials. *J. Mech. Phys. Solids* **2004**, *52* (9), 1963–1990.
<https://doi.org/10.1016/j.jmps.2004.03.006>.
- (55) Heinemann, F.; Launspach, M.; Gries, K.; Fritz, M. Gastropod Nacre: Structure, Properties and Growth - Biological, Chemical and Physical Basics. *Biophys. Chem.* **2011**, *153* (2–3), 126–153. <https://doi.org/10.1016/j.bpc.2010.11.003>.
- (56) Weiner, S.; Traub, W. Macromolecules in Mollusc Shells and Their Functions in Biomineralization. *Philos. Trans. R. Soc. London, Ser. B*, **1984**, *304*, 425–434.
<https://doi.org/10.1098/rstb.1984.0036>.
- (57) Weiner, S.; Hood, L. Soluble Protein of the Organic Matrix of Mollusk Shells: A Potential Template for Shell Formation. *Science (80-.)*. **1975**, *190* (4218), 987–989.
<https://doi.org/10.1126/science.1188379>.
- (58) Currey, J. D. Mechanical Properties of Mother of Pearl in Tension. *Proc. R. Soc. London. Ser. B. Biol. Sci.* **1977**, *196* (1125), 443–463.
<https://doi.org/10.1098/rspb.1977.0050>.
- (59) Sarikaya, M. An Introduction to Biomimetics: A Structural Viewpoint. *Microsc. Res. Tech.* **1994**, *27* (5), 360–375. <https://doi.org/10.1002/jemt.1070270503>.
- (60) Sarikaya, M.; Gunnison, K. E.; Yasrebi, M.; Aksay, I. A. Mechanical Property-Microstructural Relationships in Abalone Shell. *MRS Proc.* **1989**, *174*, 109.
<https://doi.org/10.1557/PROC-174-109>.
- (61) Launey, M. E.; Buehler, M. J.; Ritchie, R. O. *On the Mechanistic Origins of Toughness in Bone*; 2010; Vol. 40. <https://doi.org/10.1146/annurev-matsci-070909->

- 104427.
- (62) Khare, E.; Holten-Andersen, N.; Buehler, M. J. Transition-Metal Coordinate Bonds for Bioinspired Macromolecules with Tunable Mechanical Properties. *Nat. Rev. Mater.* **2021**, *6* (5), 421–436. <https://doi.org/10.1038/s41578-020-00270-z>.
 - (63) Degtyar, E.; Harrington, M. J.; Politi, Y.; Fratzl, P. The Mechanical Role of Metal Ions in Biogenic Protein-Based Materials. *Angew. Chemie - Int. Ed.* **2014**, *53* (45), 12026–12044. <https://doi.org/10.1002/anie.201404272>.
 - (64) Broomell, C. C.; Mattoni, M. A.; Zok, F. W.; Waite, J. H. Critical Role of Zinc in Hardening of Nereis Jaws. *J. Exp. Biol.* **2006**, *209* (16), 3219–3225. <https://doi.org/10.1242/jeb.02373>.
 - (65) Politi, Y.; Priewasser, M.; Pippel, E.; Zaslansky, P.; Hartmann, J.; Siegel, S.; Li, C.; Barth, F. G.; Fratzl, P. A Spider's Fang: How to Design an Injection Needle Using Chitin-Based Composite Material. *Adv. Funct. Mater.* **2012**, *22* (12), 2519–2528. <https://doi.org/10.1002/adfm.201200063>.
 - (66) Srivastava, A.; Holten-Andersen, N.; Stucky, G. D.; Waite, J. H. Ragworm Jaw-Inspired Metal Ion Cross-Linking for Improved Mechanical Properties of Polymer Blends. *Biomacromolecules* **2008**, *9* (10), 2873–2880. <https://doi.org/10.1021/bm8006659>.
 - (67) Bhattacharya, A.; Ray, P. Basic Features and Techniques. In *Polymer Grafting and Crosslinking*; John Wiley & Sons, Inc.: Hoboken, NJ, USA, 2009; pp 7–64. <https://doi.org/10.1002/9780470414811.ch2>.
 - (68) Creton, C. 50th Anniversary Perspective: Networks and Gels: Soft but Dynamic and Tough. *Macromolecules* **2017**, *50* (21), 8297–8316. <https://doi.org/10.1021/acs.macromol.7b01698>.
 - (69) Vincent, J. F. V.; Wegst, U. G. K. Design and Mechanical Properties of Insect Cuticle. *Arthropod Struct. Dev.* **2004**, *33* (3), 187–199. <https://doi.org/10.1016/j.asd.2004.05.006>.
 - (70) Andersen, S. O.; Peter, M. G.; Roepstorff, P. Cuticular Sclerotization in Insects. *Comp. Biochem. Physiol. - B Biochem. Mol. Biol.* **1996**, *113* (4), 689–705. [https://doi.org/10.1016/0305-0491\(95\)02089-6](https://doi.org/10.1016/0305-0491(95)02089-6).
 - (71) Andersen, S. O. Involvement of Tyrosine Residues, N-Terminal Amino Acids, and β -Alanine in Insect Cuticular Sclerotization. *Insect Biochem. Mol. Biol.* **2007**, *37* (9), 969–974. <https://doi.org/10.1016/j.ibmb.2007.05.002>.
 - (72) Andersen, S. O.; Roepstorff, P. Aspects of Cuticular Sclerotization in the Locust, *Scistocerca Gregaria*, and the Beetle, *Tenebrio Molitor*. *Insect Biochem. Mol. Biol.* **2007**, *37* (3), 223–234. <https://doi.org/10.1016/j.ibmb.2006.11.006>.
 - (73) Merritt, M. E.; Christensen, A. M.; Kramer, K. J.; Hopkins, T. L.; Schaefer, J. Detection of Intercatechol Cross-Links in Insect Cuticle by Solid-State Carbon-13 and Nitrogen-15 NMR. *J. Am. Chem. Soc.* **1996**, *118* (45), 11278–11282. <https://doi.org/10.1021/ja961621o>.
 - (74) Schaefer, J.; Kramer, K. J.; Garbow, J. R.; Jacob, G. S.; Stejskal, E. O.; Hopkins, T. L.; Speirs, R. D. Aromatic Cross-Links in Insect Cuticle: Detection by Solid-State ^{13}C and ^{15}N NMR. *Science* (80-.). **1987**, *235* (4793), 1200–1204. <https://doi.org/10.1126/science.3823880>.
 - (75) Kagan, H. M.; Trackman, P. C. Properties and Function of Lysyl Oxidase. *Am. J. Respir. Cell Mol. Biol.* **1991**, *5* (3), 206–210. <https://doi.org/10.1165/ajrcmb/5.3.206>.

- (76) Wu, J. J.; Eyre, D. R.; Slayter, H. S. Type VI Collagen of the Intervertebral Disc. Biochemical and Electron-Microscopic Characterization of the Native Protein. *Biochem. J.* **1987**, *248* (2), 373–381. <https://doi.org/10.1042/bj2480373>.
- (77) Yang, J.; Kramer, J. M. Proteolytic Processing of Caenorhabditis Elegans SQT-1 Cuticle Collagen Is Inhibited in Right Roller Mutants Whereas Cross-Linking Is Inhibited in Left Roller Mutants. *J. Biol. Chem.* **1999**, *274* (46), 32744–32749. <https://doi.org/10.1074/jbc.274.46.32744>.
- (78) Murray, L. W.; Tanzer, M. L.; Cooke, P. Nereis Cuticle Collagen: Relationship of Fiber Ultrastructure to Biochemical and Biophysical Properties. *J. Ultrastructure Res.* **1981**, *76* (1), 27–45. [https://doi.org/10.1016/S0022-5320\(81\)80048-2](https://doi.org/10.1016/S0022-5320(81)80048-2).
- (79) Vollmer, W.; Blanot, D.; De Pedro, M. A. Peptidoglycan Structure and Architecture. *FEMS Microbiol. Rev.* **2008**, *32* (2), 149–167. <https://doi.org/10.1111/j.1574-6976.2007.00094.x>.
- (80) Mnich, E.; Bjarnholt, N.; Eudes, A.; Harholt, J.; Holland, C.; Jørgensen, B.; Larsen, F. H.; Liu, M.; Manat, R.; Meyer, A. S.; Mikkelsen, J. D.; Motawia, M. S.; Muschiol, J.; Møller, B. L.; Møller, S. R.; Perzon, A.; Petersen, B. L.; Ravn, J. L.; Ulvskov, P. Phenolic Cross-Links: Building and de-Constructing the Plant Cell Wall. *Nat. Prod. Rep.* **2020**, *37* (7), 919–961. <https://doi.org/10.1039/c9np00028c>.
- (81) Gosline, J.; Lillie, M.; Carrington, E.; Guerette, P.; Ortlepp, C.; Savage, K. Elastic Proteins: Biological Roles and Mechanical Properties. *Philos. Trans. R. Soc. B Biol. Sci.* **2002**, *357* (1418), 121–132. <https://doi.org/10.1098/rstb.2001.1022>.
- (82) Vaccaro, E.; Waite, J. H. Yield and Post-Yield Behavior of Mussel Byssal Thread: A Self-Healing Biomolecular Material. *Biomacromolecules* **2001**, *2* (3), 906–911. <https://doi.org/10.1021/bm0100514>.
- (83) Suhre, M. H.; Gertz, M.; Steegborn, C.; Scheibel, T. Structural and Functional Features of a Collagen-Binding Matrix Protein from the Mussel Byssus. *Nat. Commun.* **2014**, *5*, 3392. <https://doi.org/10.1038/ncomms4392>.
- (84) Holten-Andersen, N.; Fantner, G. E.; Hohlbauch, S.; Waite, J. H.; Zok, F. W. Protective Coatings on Extensible Biofibres. *Nat. Mater.* **2007**, *6* (9), 669–672. <https://doi.org/10.1038/nmat1956>.
- (85) Harrington, M. J.; Masic, A.; Holten-Andersen, N.; Waite, J. H.; Fratzl, P. Iron-Clad Fibers: A Metal-Based Biological Strategy for Hard Flexible Coatings. *Science* **2010**, *328* (5975), 216–220. <https://doi.org/10.1126/science.1181044>.
- (86) Holten-Andersen, N.; Zhao, H.; Waite, J. H. Stiff Coatings on Compliant Biofibers: The Cuticle of Mytilus Californianus Byssal Threads. *Biochemistry* **2009**, *48* (12), 2752–2759. <https://doi.org/10.1021/bi900018m>.
- (87) Das, S.; Miller, D. R.; Kaufman, Y.; Martinez Rodriguez, N. R.; Pallaoro, A.; Harrington, M. J.; Gylys, M.; Israelachvili, J. N.; Waite, J. H. Tough Coating Proteins: Subtle Sequence Variation Modulates Cohesion. *Biomacromolecules* **2015**, *16* (3), 1002–1008. <https://doi.org/10.1021/bm501893y>.
- (88) Monnier, C. A.; DeMartini, D. G.; Waite, J. H. Intertidal Exposure Favors the Soft-Studded Armor of Adaptive Mussel Coatings. *Nat. Commun.* **2018**, *9* (1), 1–9. <https://doi.org/10.1038/s41467-018-05952-5>.
- (89) Valois, E.; Hoffman, C.; Demartini, D. G.; Waite, J. H. The Thiol-Rich Interlayer in the Shell/Core Architecture of Mussel Byssal Threads. *Langmuir* **2019**, *35* (48), 15985–15991. <https://doi.org/10.1021/acs.langmuir.9b01844>.

- (90) Waite, J. H. Mussel Adhesion - Essential Footwork. *J. Exp. Biol.* **2017**, *220* (4), 517–530. <https://doi.org/10.1242/jeb.134056>.
- (91) Zhao, H.; Waite, J. H. Proteins in Load-Bearing Junctions: The Histidine-Rich Metal-Binding Protein of Mussel Byssus. *Biochemistry* **2006**, *45* (47), 14223–14231. <https://doi.org/10.1021/bi061677n>.
- (92) Lee, B. P.; Messersmith, P. B.; Israelachvili, J. N.; Waite, J. H. Mussel-Inspired Adhesives and Coatings. *Annu. Rev. Mater. Res.* **2011**, *41*, 99–132. <https://doi.org/10.1146/annurev-matsci-062910-100429>.
- (93) Florioli; von Langen J; Waite. Marine Surfaces and the Expression of Specific Byssal Adhesive Protein Variants in Mytilus. *Mar. Biotechnol. (NY)*. **2000**, *2* (4), 352–363.
- (94) Papov, V. V.; Diamond, T. V.; Biemann, K.; Waite, J. H. Hydroxyarginine-Containing Polyphenolic Proteins in the Adhesive Plaques of the Marine Mussel Mytilus Edulis. *J. Biol. Chem.* **1995**, *270* (34), 20183–20192. <https://doi.org/10.1074/jbc.270.34.20183>.
- (95) Hwang, D. S.; Waite, J. H. Three Intrinsically Unstructured Mussel Adhesive Proteins, Mfp-1, Mfp-2, and Mfp-3: Analysis by Circular Dichroism. *Protein Science*. **2012**, pp 1689–1695. <https://doi.org/10.1002/pro.2147>.
- (96) Even, M. A.; Wang, J.; Chen, Z. Structural Information of Mussel Adhesive Protein Mefp-3 Acquired at Various Polymer/Mefp-3 Solution Interfaces. *Langmuir* **2008**, *24* (11), 5795–5801. <https://doi.org/10.1021/la800138x>.
- (97) Mirshafian, R.; Wei, W.; Israelachvili, J. N.; Waite, J. H. α,β -Dehydro-Dopa: A Hidden Participant in Mussel Adhesion. *Biochemistry* **2016**, *55* (5), 743–750. <https://doi.org/10.1021/acs.biochem.5b01177>.
- (98) Lu, Q.; Danner, E.; Waite, J. H.; Israelachvili, J. N.; Zeng, H.; Hwang, D. S. Adhesion of Mussel Foot Proteins to Different Substrate Surfaces. *J. R. Soc. Interface* **2013**, *10* (79). <https://doi.org/10.1098/rsif.2012.0759>.
- (99) Nicklisch, S. C. T.; Spahn, J. E.; Zhou, H.; Gruian, C. M.; Waite, J. H. Redox Capacity of an Extracellular Matrix Protein Associated with Adhesion in Mytilus Californianus. *Biochemistry* **2016**, *55* (13), 2022–2030. <https://doi.org/10.1021/acs.biochem.6b00044>.
- (100) Yu, J.; Wei, W.; Danner, E.; Israelachvili, J. N.; Waite, J. H. Effects of Interfacial Redox in Mussel Adhesive Protein Films on Mica. *Adv. Mater.* **2011**, *23* (20), 2362–2366. <https://doi.org/10.1002/adma.201003580>.
- (101) Danner, E. W.; Kan, Y.; Hammer, M. U.; Israelachvili, J. N.; Waite, J. H. Adhesion of Mussel Foot Protein Mefp-5 to Mica: An Underwater Superglue. *Biochemistry* **2012**, *51* (33), 6511–6518. <https://doi.org/10.1021/bi3002538>.
- (102) Helm, C. A.; Knoll, W.; Israelachvili, J. N. Measurement of Ligand-Receptor Interactions. *Proc. Natl. Acad. Sci. U. S. A.* **1991**, *88* (18), 8169–8173. <https://doi.org/10.1073/pnas.88.18.8169>.
- (103) Anderson, T. H.; Yu, J.; Estrada, A.; Hammer, M. U.; Waite, J. H.; Israelachvili, J. N. The Contribution of DOPA to Substrate-Peptide Adhesion and Internal Cohesion of Mussel-Inspired Synthetic Peptide Films. *Adv. Funct. Mater.* **2010**, *20* (23), 4196–4205. <https://doi.org/10.1002/adfm.201000932>.
- (104) Lee, H.; Scherer, N. F.; Messersmith, P. B. Single-Molecule Mechanics of Mussel Adhesion. *Proc. Natl. Acad. Sci. U. S. A.* **2006**, *103* (35), 12999–13003.

- <https://doi.org/10.1073/pnas.0605552103>.
- (105) Yu, J.; Wei, W.; Menyo, M. S.; Masic, A.; Waite, J. H.; Israelachvili, J. N. Adhesion of Mussel Foot Protein-3 to TiO₂ Surfaces: The Effect of PH. *Biomacromolecules* **2013**, *14* (4), 1072–1077. <https://doi.org/10.1021/bm301908y>.
- (106) Yu, J.; Wei, W.; Danner, E.; Ashley, R. K.; Israelachvili, J. N.; Waite, J. H. Mussel Protein Adhesion Depends on Interprotein Thiol-Mediated Redox Modulation. *Nat. Chem. Biol.* **2011**, *7* (9), 588–590. <https://doi.org/10.1038/nchembio.630>.
- (107) Miller, D. R.; Spahn, J. E.; Waite, J. H. The Staying Power of Adhesion-Associated Antioxidant Activity in *Mytilus Californianus*. *J. R. Soc. Interface* **2015**, *12* (111), 20150614. <https://doi.org/10.1098/rsif.2015.0614>.
- (108) Maier, G. P.; Rapp, M. V.; Waite, J. H.; Israelachvili, J. N.; Butler, A. Adaptive Synergy between Catechol and Lysine Promotes Wet Adhesion by Surface Salt Displacement. *Science (80-.)*. **2015**, *349* (6248), 628–632. <https://doi.org/10.1126/science.aab0556>.
- (109) Hwang, D. S.; Zeng, H.; Srivastava, A.; Krogstad, D. V.; Tirrell, M.; Israelachvili, J. N.; Waite, J. H. Viscosity and Interfacial Properties in a Mussel-Inspired Adhesive Coacervate. *Soft Matter* **2010**, *6* (14), 3232. <https://doi.org/10.1039/c002632h>.
- (110) Wei, W.; Tan, Y.; Martinez Rodriguez, N. R.; Yu, J.; Israelachvili, J. N.; Waite, J. H. A Mussel-Derived One Component Adhesive Coacervate. *Acta Biomater.* **2014**, *10* (4), 1663–1670. <https://doi.org/10.1016/j.actbio.2013.09.007>.
- (111) Valois, E.; Mirshafian, R.; Waite, J. H.; Waite, J. H. Phase-Dependent Redox Insulation in Mussel Adhesion. *Sci. Adv.* **2020**, *6* (23), 1–8. <https://doi.org/10.1126/sciadv.aaz6486>.
- (112) Murphy, E. A. K.; Dorgan, K. M. Burrow Extension with a Proboscis: Mechanics of Burrowing by the Glycerid *Hemipodus Simplex*. *J. Exp. Biol.* **2011**, *214* (6), 1017–1027. <https://doi.org/10.1242/jeb.051227>.
- (113) Michel, C.; Fonze-Vignaux, M.-T.; Voss-Foucart, M. F. Donnees Nouvelles Sur La Morphologie, l'histochimie et La Composition Chimique Des Mâchoires de *Glycera Convolvata* Keferstein (Annelide, Polychete). *Bull. Biol. Fr. la Belgique* **1973**, *107*, 301–321.
- (114) Voss-Foucart, M. F.; Fonce-Vignaux, M. T.; Jeuniaux, C. Systematic Characters of Some Polychaetes (Annelida) at the Level of the Chemical Composition of the Jaws. *Biochem. Syst. Ecol.* **1973**, *1* (2), 119–122. [https://doi.org/10.1016/0305-1978\(73\)90025-2](https://doi.org/10.1016/0305-1978(73)90025-2).
- (115) Gibbs, P. E.; Bryan, G. W. Copper-the Major Metal Component of Glycerid Polychaete Jaws. *J. Mar. Biol. Assoc. United Kingdom* **1980**, *60* (1), 205–214. <https://doi.org/10.1017/S0025315400024267>.
- (116) Colbath, G. K. Jaw Mineralogy in Eunician Polychaetes (Annelida). *Micropaleontology* **1986**, *32* (2), 186. <https://doi.org/10.2307/1485632>.
- (117) Lichtenegger, H. C.; Schöberl, T.; Bartl, M. H.; Waite, H.; Stucky, G. D. High Abrasion Resistance with Sparse Mineralization: Copper Biomineral in Worm Jaws. *Science* **2002**, *298* (5592), 389–392. <https://doi.org/10.1126/science.1075433>.
- (118) Bhushan, B. *Principles and Applications to Tribology*; John Wiley & Sons, Ltd: The Atrium, Southern Gate, Chichester, West Sussex, PO19 8SQ, UK, 2013. <https://doi.org/10.1002/9781118403020>.
- (119) Moses, D. N.; Harreld, J. H.; Stucky, G. D.; Waite, J. H. Melanin and *Glycera* Jaws.

- J. Biol. Chem.* **2006**, *281* (46), 34826–34832.
<https://doi.org/10.1074/jbc.M603429200>.
- (120) Clancy, C. M. R.; Simon, J. D. Ultrastructural Organization of Eumelanin from *Sepia Officinalis* Measured by Atomic Force Microscopy. *Biochemistry* **2001**, *40* (44), 13353–13360. <https://doi.org/10.1021/bi010786t>.
- (121) Money, N. P.; Caesar-TonThat, T.-C.; Frederick, B.; Henson, J. M. Melanin Synthesis Is Associated with Changes in Hyphopodial Turgor, Permeability, and Wall Rigidity In *Gaeumannomyces Graminis* var. *Graminis*. *Fungal Genet. Biol.* **1998**, *24* (1–2), 240–251. <https://doi.org/10.1006/fgbi.1998.1052>.
- (122) Moses, D. N.; Mattoni, M. A.; Slack, N. L.; Waite, J. H.; Zok, F. W. Role of Melanin in Mechanical Properties of Glycera Jaws. *Acta Biomater.* **2006**, *2* (5), 521–530. <https://doi.org/10.1016/j.actbio.2006.05.002>.
- (123) Pontin, M. G.; Moses, D. N.; Waite, J. H.; Zok, F. W. A Nonmineralized Approach to Abrasion-Resistant Biomaterials. *Proc. Natl. Acad. Sci. U. S. A.* **2007**, *104* (34), 13559–13564. <https://doi.org/10.1073/pnas.0702034104>.
- (124) Moses, D. N.; Pontin, M. G.; Waite, J. H.; Zok, F. W. Effects of Hydration on Mechanical Properties of a Highly Sclerotized Tissue. *Biophys. J.* **2008**, *94* (8), 3266–3272. <https://doi.org/10.1529/biophysj.107.120790>.
- (125) Dana Novak Moses. Structure, Biochemistry, and Mechanical Properties of Glycera Marine Worm Jaws. **2007**, No. September, 177.
- (126) Moses, D. N.; Harreld, J. H.; Stucky, G. D.; Waite, J. H. Melanin and Glycera Jaws. *J. Biol. Chem.* **2006**, *281* (46), 34826–34832.
<https://doi.org/10.1074/jbc.M603429200>.
- (127) Broomell, C. C.; Chase, S. F.; Laue, T.; Waite, J. H. Cutting Edge Structural Protein from the Jaws of *Nereis Virens*. *Biomacromolecules* **2008**, *9* (6), 1669–1677. <https://doi.org/10.1021/bm800200a>.
- (128) Bovill, W. D.; Downes, B. J.; Lancaster, J. Caddisfly Egg Mass Morphology Mediates Egg Predation: Potential Costs to Individuals and Populations. *Freshw. Biol.* **2015**, *60* (2), 360–372. <https://doi.org/10.1111/fwb.12497>.
- (129) Rezende, G. L.; Martins, A. J.; Gentile, C.; Farnesi, L. C.; Pelajo-Machado, M.; Peixoto, A. A.; Valle, D. Embryonic Desiccation Resistance in *Aedes Aegypti*: Presumptive Role of the Chitinized Serosal Cuticle. *BMC Dev. Biol.* **2008**, *8*, 1–14. <https://doi.org/10.1186/1471-213X-8-82>.
- (130) Rapoport, H. S.; Shadwick, R. E. Mechanical Characterization of an Unusual Elastic Biomaterial from the Egg Capsules of Marine Snails (*Busycon* Spp.). *Biomacromolecules* **2002**, *3* (1), 42–50. <https://doi.org/10.1021/bm0155470>.
- (131) Thomason, J. C.; Davenport, J.; Rogerson, A. Antifouling Performance of the Embryo and Eggcase of the Dogfish *Scyliorhinus Canicula*. *J. Mar. Biol. Assoc. United Kingdom* **1994**, *74* (4), 823–836. <https://doi.org/10.1017/s002531540009007x>.
- (132) Bisgrove, B. W.; Andrews, M. E.; Raff, R. A. Fibropellins, Products of an EGF Repeat-Containing Gene, Form a Unique Extracellular Matrix Structure That Surrounds the Sea Urchin Embryo. *Dev. Biol.* **1991**, *146* (1), 89–99. [https://doi.org/10.1016/0012-1606\(91\)90449-D](https://doi.org/10.1016/0012-1606(91)90449-D).
- (133) Boletzky, S. Encapsulation of Cephalopod Embryos - a Search for Functional Correlations. *Am. Malacol. Bull.* **1986**, *4*, 217–227.
- (134) Sinn, D. L.; Perrin, N. A.; Mather, J. A.; Anderson, R. C. Early Temperamental Traits

- in an Octopus (*Octopus Bimaculoides*). *J. Comp. Psychol.* **2001**, *115* (4), 351–364. <https://doi.org/10.1037/0735-7036.115.4.351>.
- (135) Boletzky, S. Nos Connaissances Actuelles Sur Le Développement Des Octopodes. *Vie Milieu* **1978**, *28/2*, 85–120.
- (136) Neville, A. C. The Physics of Helicoids. *Phys. Bull.* **1986**, *37* (2), 74–76. <https://doi.org/10.1088/0031-9112/37/2/028>.
- (137) Bullough, P. A.; Tulloch, P. A. High-Resolution Spot-Scan Electron Microscopy of Microcrystals of an α -Helical Coiled-Coil Protein. *J. Mol. Biol.* **1990**, *215* (1), 161–173. [https://doi.org/10.1016/S0022-2836\(05\)80101-9](https://doi.org/10.1016/S0022-2836(05)80101-9).
- (138) Neville, A. C. Cholesteric Proteins. *Mol. Cryst. Liq. Cryst.* **1981**, *76* (3–4), 279–286. <https://doi.org/10.1080/00268948108076161>.
- (139) Walker, A. A.; Weisman, S.; Kameda, T.; Sutherland, T. D. Natural Templates for Coiled-Coil Biomaterials from Praying Mantis Egg Cases. *Biomacromolecules* **2012**, *13* (12), 4264–4272. <https://doi.org/10.1021/bm301570v>.
- (140) Rapoport, H. S.; Shadwick, R. E. Reversibly Labile, Sclerotization-Induced Elastic Properties in a Keratin Analog from Marine Snails: Whelk Egg Capsule Biopolymer (WECB). *J. Exp. Biol.* **2007**, *210* (1), 12–26. <https://doi.org/10.1242/jeb.02613>.
- (141) Miserez, A.; Wasko, S. S.; Carpenter, C. F.; Waite, J. H. Non-Entropic and Reversible Long-Range Deformation of an Encapsulating Bioelastomer. *Nat. Mater.* **2009**, *8* (11), 910–916. <https://doi.org/10.1038/nmat2547>.

CHAPTER 2

The effect of the protein backbone on mussel protein adhesion

Reproduced with permission from: Wonderly, W. R.; Cristiani, T. R.; Cunha, K. C.; Degen, G. D.; Shea, J. E.; Waite, J. H. Dueling Backbones: Comparing Peptoid and Peptide Analogues of a Mussel Adhesive Protein. *Macromolecules* **2020**, *53* (16), 6767–6779.

A. Abstract

Ensembles of amino acid side chains often dominate the interfacial interactions of intrinsically disordered proteins, however, backbone contributions are far from negligible. Using a combination of nanoscale force measurements and molecular dynamics simulations, we demonstrated with analogous mussel-mimetic adhesive peptides and peptoids 34-residues long that highly divergent adhesive/cohesive outcomes can be achieved on mica surfaces by altering backbone chemistry only. The Phe, Tyr and Dopa peptoid variants used in this study deposited as dehydrated and incompressible films that facilitated analysis of peptoid side chain contributions to adhesion and cohesion. For example, whereas Phe and Dopa peptoids exhibited similar cohesion, Dopa peptoids were ~3 times more adhesive than Phe peptoids on mica. Compared with the peptides, Phe peptoid achieved only ~20% of Phe-peptide adhesion, but the Dopa peptoids were >2-fold more adhesive than the Dopa peptides. Cation- π interactions accounted for some but not all of the cohesive interactions. Our results were corroborated by molecular dynamics simulations and highlight the importance of backbone chemistry and the potential of peptoids or peptoid/peptide hybrids as wet adhesives and primers.

B. Introduction

Marine mussels produce a tough byssus to adhere to rocky substrates in habitats along turbulent wind- and wave-swept seashores.¹ Biochemical and molecular analysis of byssal

adhesive plaques has shown that mussel foot peptides and/or proteins (Mfps) particularly rich in two amino acids, 3,4-dihydroxyphenylalanine (Dopa) and lysine (Lys) are commonly localized at the interface between each plaque and the underlying substratum.^{1,2} The catecholic and cationic side-chains of these residues work separately and in synergy to maximize both adhesion and cohesion. We define adhesion as bonding between the adhesive polymer and the underlying surface, whereas cohesion refers to bonds within the adhesive. Adhesion and cohesion can result from many interactions, including charge-charge interactions between Lys and negative surface charges, mono- and bi-dentate hydrogen bonding between Dopa and surface oxides, metal chelation between Dopa and surface transition metals, cation- π bonding between Lys and aromatic side chains, oxidative coupling between Dopa and other residues, hydrophobic interactions, and π - π coupling.^{1,3-5} Although numerous studies have shown that native adhesive proteins display diverse adhesive/cohesive interactions on various polymer, mineral and oxide surfaces,^{4,6-14} the desire for simple mechanistic insights has driven the design and testing of adhesive analogs of reduced complexity. In this way, mussel-inspired peptides and other small molecules have been utilized to investigate the relative importance of each of the above-listed intermolecular interactions. Largely absent has been an exploration of contributions by peptide backbone chemistry and structure to intermolecular adhesive forces. Although the peptide sequences relevant to the mussel system are intrinsically disordered,¹⁵ the peptide backbone inherently influences intra- and intermolecular interactions, enabling transient β -sheet-like structures, restricting backbone conformational freedom, and allowing backbone H-bonding to appropriate amino acid side chains.

Our study was prompted by a previous report¹⁶ that concluded counterintuitively that the adhesive performance of mussel foot peptide (Mfp) mimics was largely due to cohesive effects. The authors used an Mfp-5-derived sequence that was adjusted to 3 increasing steps in aromatic ring hydroxylation (Fig. 2.1) and measured the adhesion forces required to separate atomically smooth mica surfaces coated with these molecules under acidic pH (~3) and high ionic strength (> 250 mM) regimes. Peptides containing phenylalanine (Phe), tyrosine (Tyr), or 3,4-dihydroxyphenylalanine (Dopa) (Fig. 2.1B) consistently adsorbed as multilayer films and all forces measured were cohesive. Surprisingly, the Phe-peptides exhibited the strongest cohesive interactions. The Tyr- and Dopa-containing homologs though similar in performance, achieved only a third of the Phe cohesion. Based on these results as well as solution NMR of the peptides, they concluded that cation- π interactions are largely responsible for cohesion, and that cohesion is reduced in the cases of Tyr and Dopa by entropically unfavorable steric contributions of hydroxyl groups. In this report, we explore the role of backbone chemistry and structure in the adhesive/cohesive interactions of the mussel adhesive mimetic sequences. Accordingly, we synthesized peptoid analogs (Fig. 2.1A) of the previously studied peptides and measured their surface interactions with mica using the surface forces apparatus (SFA) (Fig. 2.1C).

Peptoids differ from peptides by relocating the side chains from the α -carbon to the amide nitrogen (Fig. 2.1A, B). This change leads to an achiral α -carbon, removes amide hydrogens (and therefore the potential for backbone hydrogen bond donation), and weakens the electron delocalization in the polyamide backbone bonds, giving the backbone more conformational freedom.^{17,18} The lack of an amide hydrogen bond donor in peptoids prohibits the formation of backbone-stabilized secondary structures such as α -helices and β -sheets.

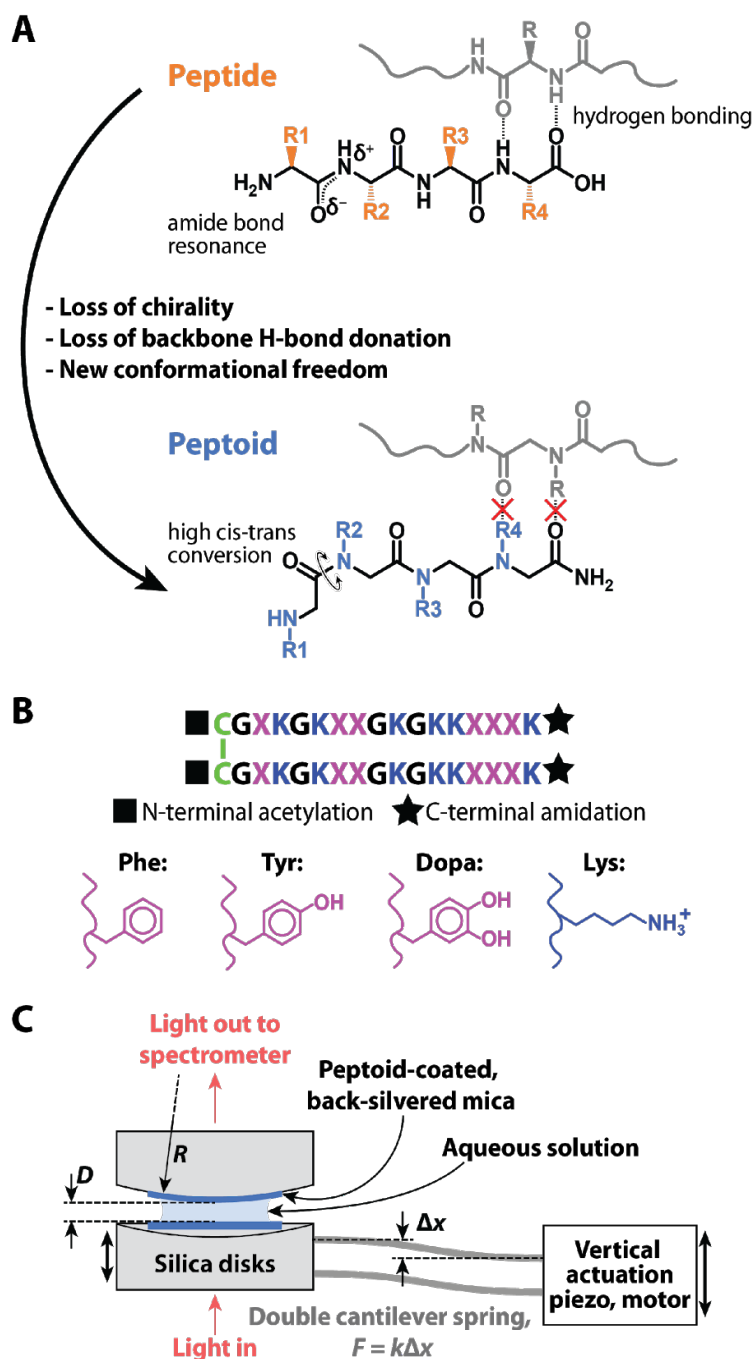


Figure 2.1 Peptoid chemistry and experimental SFA setup. A) A chemical description illustrating the differences between generic peptide (*top*) and peptoid (*bottom*) molecules. B) The sequence relevant to all peptides and peptoids discussed in this manuscript. For each molecule, the “X” position in the sequence can be either Phe, Tyr, or Dopa (*purple*) and is internally consistent for each molecule tested. A cystine linkage, used to double the peptoid molecular weight, is depicted by C-C (*green*). The lysine side chain is depicted in blue and the glycine side chain (G) is simply -H. C) Schematic of the SFA 2000 used to measure force vs. distance profiles.

We observed differences between the adhesion/cohesion strengths of asymmetrically- and symmetrically-deposited peptoid films resulting from the absence of backbone hydrogen bonding groups. Our SFA results indicate peptoid films are less hydrated which we attribute to the increased backbone hydrophobicity. These results are corroborated with molecular

dynamics (MD) simulations of both the peptide and peptoid molecules in solution and at mica surfaces.

C. Materials & Methods

i. Materials

Triethylamine (TEA), methyl trifluoroacetate (MeTFA), pyridinium p-toluenesulfonate (PPTS), triisopropylsilane (TIPS), and methanol, potassium nitrate, acetic acid, dimethylformamide (DMF), anhydrous sodium sulfate, mushroom tyrosinase (3,000 U/mg), N-*t*-boc-1,4-diaminobutane, and all Fmoc-protected amino acids were purchased from Sigma Aldrich and used as received. Ethyl acetate (EtOAc), tetrahydrofuran (THF), and dichloromethane (DCM) were purchased from VWR. Lithium hydroxide, 4-hydroxybenzylamine, 3,4-dihydro-2H-pyran (DHP), bromoacetic acid, trifluoroacetic acid (TFA), and benzylamine were purchased from ACROS Organics. Diisopropylcarbodiimide (DIC) was purchased from Chem-Impex International, Inc. Rink amide resin was purchased from Novabiochem. All materials and solvents were purchased to be either reagent or HPLC grade, respectively. The peptides used in this study were prepared exactly as described in previous investigations.^{12,16}

ii. Submonomer syntheses:

Tfa protection of 4-hydroxybenzylamine. 4-hydroxybenzylamine (25 g, 203 mmol) and TEA (85 mL, 609mmol) were added to methanol and stirred for 10 minutes until fully dissolved. Me-TFA (52 g, 406mmol) was then slowly added over a period of 20 min, and the reaction mixture was stirred at room temperature overnight. Reaction completion was determined by ninhydrin. The solvent was removed via rotary evaporation. The residue was

treated with 1N HCl (100 mL) and extracted with ethyl acetate (3x75 mL). The organic layer was washed with 1N HCl (100 mL), brine (100mL), dried over Na₂SO₄, filtered, and the solvent removed to afford a brown solid (40 g, 88%).

THP protection of Tfa-4-hydroxybenzylamine. Tfa-4-hydroxybenzylamine (40 g, 183 mmol) and PPTS (6.28g, 25mmol) were added to a 1000mL round bottom flask and dissolved with DCM (250mL). DHP (42.7g, 507.5 mmol) was added over a 20 min period *via* an addition funnel. After 1 hour of stirring the reaction mixture at room temperature a white precipitate formed. The reaction was stirred over night at room temperature. The reaction mixture was cooled to -20°C and the white, crystalline precipitate was removed by filtration and washed with cold DCM and dried under high vacuum yielding the product as white crystals (30.6 g, 101 mmol, 55% yield). ¹H NMR (400 MHz CHCl₃): δ(ppm) 7.23 (d, J=8.6Hz, 2H), 7.06 (d, J=8.6Hz, 2H), 5.44 (t, J=3.1Hz,1H), 4.47 (d, J=5.9Hz, 2H), 2.00 (m, 1H), 1.87 (m, 2H), 1.66 (m, 3H).

Tfa-deprotection. Lithium hydroxide (2.75g, 57.5 mmol) dissolved in 100mL H₂O was added to a stirring solution of Tfa/THP protected 4-hydroxybenzylamine (17.5g, 57.7mmol) dissolved in THF (200mL) in a 1000 mL round bottom flask. The reaction was stirred for 3 hours, after which the THF was removed by rotary evaporation. Water (50 mL) was added, and the aqueous solution was extracted with ethyl acetate (3x100mL). The organic layers were combined, washed with water, dried over Na₂SO₄ and evaporated down to a yellow oil (9.54 g, 80%). ¹H NMR (400 MHz CHCl₃): δ (ppm) 7.2 (d, J=8.6Hz, 2H), 7.01 (d, J=8.6, 2H), 5.39 (t, J=3.1Hz, 1H), 3.89 (m, 1H), 3.77 (s, 2H), 3.58 (m, 1H), 1.99 (m, 1H), 1.84 (m, 2H), 1.63 (m, 3H).

iii. Peptoid synthesis:

Peptoids were synthesized using a Symphony X automated peptide synthesizer on a 50 μ M scale using Rink amide resin (0.64mmol/g). Peptoid coupling was as in previously published procedures.¹⁹ Bromoacetylation was achieved by treatment with DIC (0.8 M in DMF) and bromoacetic acid (0.8 M in DMF), and displacements by treatment with 1M amine concentration. THP protected 4-hydroxybenzylamine, benzylamine, and N-*t*-boc-1,4-diaminobutane were used as tyrosine, phenylalanine, and lysine mimics, respectively. Glycine and cysteine were incorporated using standard Fmoc solid-phase synthesis procedures.²⁰ Couplings were performed using a solution of Fmoc-protected amino acid (0.8 M in DMF) and DIC (0.8 M in DMF) for 20 min. The Fmoc protecting group was removed by treating the resin with a 20% piperidine solution in DMF for 10 min. The N-termini of oligomers were acetylated on resin by treatment with a solution of acetic anhydride (3 parts) and pyridine (2 parts) for 30 minutes. Peptoids were cleaved from the resin by treatment with 95:2.5:2.5 TFA/H₂O/TIPS for 30 minutes. Solvent was removed from cleaved peptoids using a Biotage V-10 evaporator, and the crude peptoids were dissolved in 5% acetonitrile. Purification was achieved using reverse-phase HPLC with a C18 semipreparative column at a flow rate of 10mL/min.

iv. Peptoid modification.

Peptoids were dimerized with disulfide linkages as described previously.¹⁶ Monomers (1 mg) were dissolved in 0.1 M phosphate buffer (1mL, pH=7) and NaIO₄ was added (10 μ L, 5mg/mL). The solution was shaken for 20 minutes, filtered, and injected onto a reverse-phase HPLC using a C18 column and purified with a linear gradient of aqueous acetonitrile (5 –

70%). Protein elution was monitored at 280 nm and the peak fractions were analyzed by matrix-assisted laser desorption ionization mass spectrometry (MALDI-MS).

The Tyr peptoid was modified by mushroom tyrosinase to obtain the Dopa peptoid¹². The peptoid containing the tyrosine mimic (1 mg) was dissolved in a 100mM phosphate/50mM borate buffer (1 mL, pH=7). Mushroom tyrosinase (0.3 mg) was added and the solution bubbled with oxygen for 4 hours, after which the reaction was stopped by the addition of glacial acetic acid (50 μ L). This solution was then filtered, purified by reverse-phase HPLC, and analyzed with MALDI-MS as described for the dimerization process. Fractions containing the most Dopa residues (10-13) were frozen, lyophilized, and resuspended in 100 mM acetic acid (Sigma-Aldrich) buffer (pH = 2.5) to ~1 mg/mL and stored at -80°C°.

v. Surface Forces Apparatus Measurements:

Standard SFA procedures were used to measure force vs. distance profiles, normalized by the contact radius ($F(D)/R$) as previously detailed.²¹ Before each experiment, the thickness of the mica was measured in air. Subsequently, a peptoid film was established on one (asymmetrical deposition) or both (symmetrical deposition) of the mica surfaces. To deposit a peptoid film, the mica surface was removed from the SFA in a laminar flow cabinet and exposed to 3 mL of 250 mM KNO₃, 100 mM acetic acid (pH 2.5-2.8) solutions. Subsequently, 15 μ L of a 1 mg/mL peptoid solution in 100 mM acetic acid was diluted into the 3 mL salt solution and the surface was incubated for 20-30 min. The surface was then flushed with generous amounts (5-10 mL) of peptoid-free salt solution and transferred back into the SFA, carefully kept wetted by a droplet of solution. Therefore, symmetrical deposition resulted in contact between peptoid films on each surface, while asymmetrical deposition resulted in contact between a peptoid film and a bare mica surface. These experimental conditions were

chosen to identically match those used by Gebbie *et al.*¹⁶ The two surfaces (Figure 2.1C) were then brought into molecular contact at nm/s velocities, generating the ‘Compression’ curves of force-distance profiles. After compression, the surfaces were retracted at nm/s velocities following a ~5 min total contact time. During separation, the double cantilever springs (Figure 2.1C) progressively accumulate tensile stress until the surfaces abruptly jump apart to distances > 500 nm. The jump distance multiplied by the cantilever spring constant, k , measures the force of adhesion (or cohesion), F_{ad} , between the surfaces. For comparison between experiments, F_{ad} is normalized by the measured contact radius of the interacting surfaces for each experiment. Because of the mixed adhesive/cohesive failure modes in these systems, F_{ad} is not normalized to an adhesion energy by either the Derjaguin approximation²¹ or the Johnson-Kendall-Roberts (JKR) theory of adhesion.²²

vi. Molecular Dynamics Simulations

The simulations were performed using the software GROMACS 2018²³. The GROMOS 53A6 force field²⁴ was used for the peptides and a new set of parameters consistent with the GROMOS 53A6 peptide force field was developed for the peptoids (Cunha, K. C.; Shea, J. E.; unpublished data, Supporting Review Only). The mica model consisted of a single layer of *muscovite-2M₁* ($KAl_2(Si_3Al)O_{10}(OH)_2$)²⁵ comprised of 5,120 atoms and the INTERFACE force field parameters used for the surface²⁶. Atomic point charges for the catechol hydroxyl groups were estimated by a RESP fitting²⁷ from calculations using MP2/6-31G** within NWChem 6.1²⁸, as described earlier²⁹. After solvation, the energy was optimized using up to 100,000 steps of the steepest descent algorithm.

Simulations in bulk water: The starting structure for the molecular dynamics simulations consisted of the peptoid/peptide molecules in SPC water molecules model³⁰ with

12 Cl⁻ ions for neutral charge. The initial systems consisted of the extended peptoid/peptide structures in a cubic simulation box (10x10x10 nm). After 20 ns of simulation, the final (and more compact) structure was placed into a smaller box (6x6x6 nm) to run for 1 μ s. Periodic boundary conditions were used in the x , y and z axes with the NPT ensemble. The LINCS method³¹ was used to constrain bonds involving all atoms. The Leapfrog algorithm³² was used with a time step of 2-fs. Long-range electrostatic interactions were treated using the PME method³³ and short-range electrostatics and van der Waals interactions were computed within the cutoff radii of 1.2 nm and updated every 10 steps with the cut-off scheme Verlet. The temperature was kept at 300 K using the Nose-Hoover scheme³⁴ and 0.5 ps as a time constant for coupling, using the isothermal compressibility of $4.5 \cdot 10^{-5} \text{ bar}^{-1}$. Two groups were used to couple temperature separately: one containing the peptide/peptoid and another one with the remaining atoms. The Parrinello-Rahman barostat^{35,36} was used to couple pressure at 1 bar isotropically with a time constant of 2.0 ps. The center of mass motion was removed at every 100 steps. Other variables were kept at their default values in the Gromacs package.

The last frame of the 1 μ s simulation was used as the initial frame of the REMD simulation, which consisted of 64 replicas. Initially, each replica was heated in NVT simulations for 5 ns using the v-rescale scheme³⁴ with a relaxation time of 0.1 ps. A temperature range of 294 to 500 K was used, with on average an exchange rate between adjacent replicas of 25%, calculated at the initial 10 ns of simulation. The exchanges between replicas were attempted every 3 ps. The REMD simulations were performed for 500 ns at NVT, using the Nose-Hoover scheme³⁴ and 1 ps as a time constant. A cut-off of 1 nm was used for the short-range electrostatics and the *pair list* update was automatically set to 100 steps. The center of mass motion was removed at every 500 steps.

Simulations on mica The structure obtained from the 1 μ s simulation of each peptoid/peptide molecule in bulk water was used as the starting structure in these REMD simulations. The structures were placed at a minimum distance of about 1.5 nm away from mica. The systems were solvated with SPC water model molecules³⁰ with 244 K^+ ions in a box size of 8.71108x7.56629x8.00000. Initially, the systems were slowly heated to 300 K in NVT simulations for 1 ns, using the v-rescale scheme³⁴ with a relaxation time of 0.1 ps. Followed by a second equilibration to have each of the 80 replicas of the systems at a temperature ranging from about 295 to 470 K. The temperatures were chosen to have an average exchange rate of 25% between adjacent replicas, calculated during 1 ns of simulation. The exchanges between replicas were attempted every 3 ps. The REMD simulations were performed for 500 ns at NVT. During all those simulations the mica atoms (except hydrogen) were held stationary. Other conditions for these REMD simulations are the same as described for the REMD simulations in bulk water.

Simulation Analysis The GROMACS tools `g_mindist`, `g_hbond`, `g_pairdist`, `g_gyration`, and `g_cluster` were used to measure the number of contacts between Lys and mica; hydrogen bonding; the backbone maximum distances (R_{max}); the radius of gyration (R_g) and to cluster the structures of peptides/peptoids. The clusters criteria were: RMSD cutoff of 1.4 Å for the backbone atoms (excluding the tip residues), using the algorithm described by Daura *et al.*³⁷

Hydrogen bond cutoffs were: 3.5 Å for the distance Donor – Acceptor and 30° for the angle Hydrogen - Donor - Acceptor. The secondary structure contents were calculated by DSSP.^{38,39} Molecular representations were generated by Visual Molecular Dynamics (VMD) 1.9.4.⁴⁰

vii. Circular Dichroism

CD spectra were collected on a JASCO J-1500 circular dichroism spectrometer at 25°C with a scan range of 200-250 nm, scan speed of 20 nm/min, digital integration time of 8s, and with 3 scans being averaged. Solutions of Phe and Tyr-peptide dimers were prepared at a concentration of 20µM in 10mM AcOH and experiments were run using a 0.5 mm pathlength quartz cuvette. To estimate secondary structure content the peptide spectra were decomposed using the BeStSel algorithm.⁴¹

D. Results

i. Peptoid Design and Synthesis

To facilitate comparison with the peptides reported by Gebbie *et al.*,¹⁶ we synthesized matching peptoids for the distinctive adhesive sequence *i.e.* GYK GKYYGK GK KYYK (res# 30-45 in mfp-5⁴²) with one Cys added at the N-terminus for peptide coupling. Each peptoid sequence consists of the peptoid analogs for the amino acids lysine (Lys), glycine (Gly), and counterparts to each of phenylalanine (Phe), tyrosine (Tyr) or 3,4-dihydroxyphenylalanine (Dopa). The Cys-S-S-Cys linkage served to lengthen the construct as in the previous peptide study.¹⁶ The locations and quantities of the Gly, Cys, Lys, and aromatic amino acids are conserved among the three peptoids (Fig. 2.1B). The high charge content of the peptoid sequences, afforded by a ~35 mol% Lys composition, allows these molecules to displace hydrated K⁺ on mica surfaces⁴³ and form multiple coulombic surface interactions per peptoid molecule, thereby bonding them to the mica surface. The aromatic side chains (Phe, Tyr, Dopa) were included to mediate other interactions such as hydrophobic interactions, cation- π complexation, π - π interactions, and hydrogen bonding (in the case of Tyr and Dopa).

ii. SFA Measurements

Mica surfaces, such as those schematically depicted in Fig. 2.1C, are minimally adhesive ($F_{ad}/R < 2$ mN/m, Fig. 2.2) when exposed to the 250mM KNO₃, 100mM acetic acid solutions used in this study (high salt conditions), and separated at several nm/s. The separation force increased after deposition of each Phe, Tyr, or Dopa peptoid variant. The blue bars in Figure 2.2 show the separation forces mediated by each peptoid. Solid bars correspond to peptoids deposited asymmetrically onto one mica surface only (Fig. 2.2, inset, left), whereas

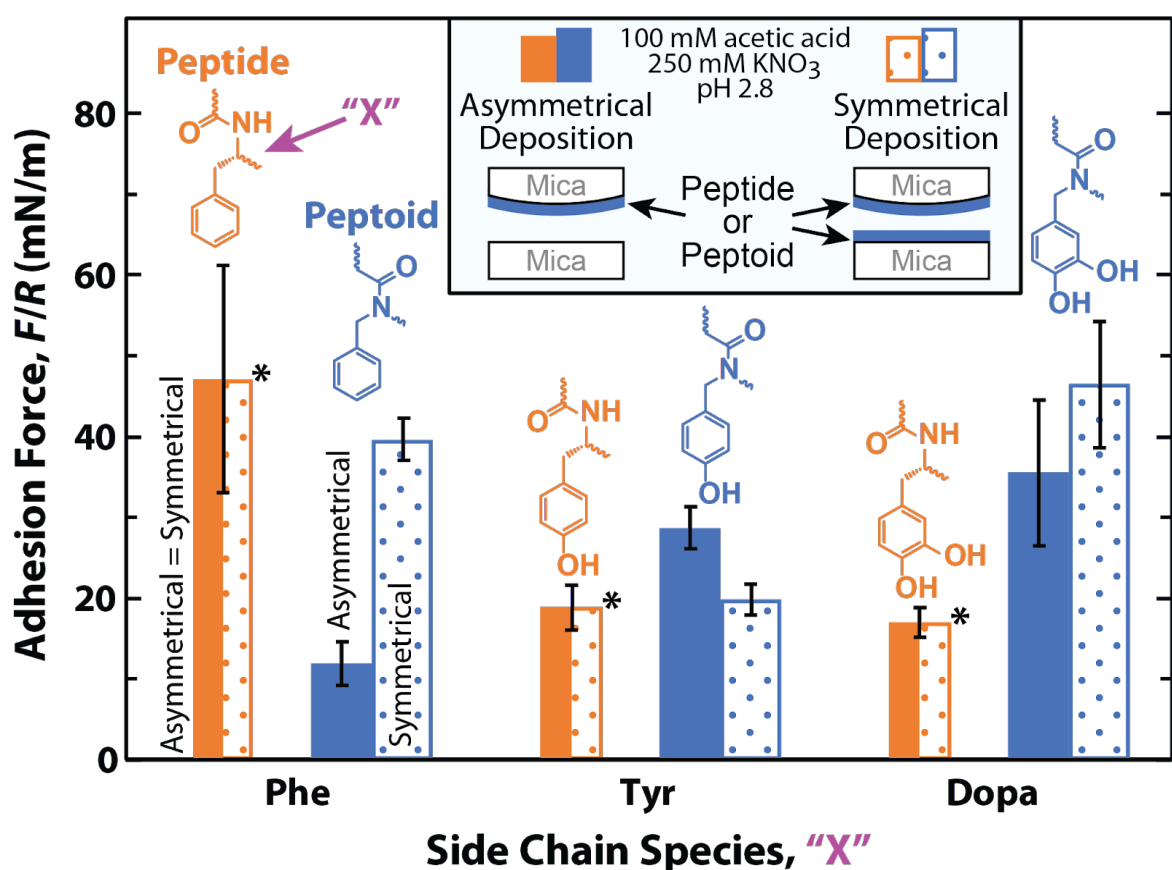


Figure 2.2. Adhesive and cohesive forces of peptoids and peptides. Adhesive and cohesive forces between asymmetric (*solid bars*) and symmetric (*dotted bars*) films on mica surfaces in the SFA comparing peptide (orange) and peptoid (blue) films. Error bars denote means with standard deviations. Inset shows test configurations with the background solution conditions. The aromatic residue present in each peptide/peptoid variant is illustrated above each set of bars. To allow for comparison between datasets, the peptoid experiments were conducted under conditions identical to those of the previous peptide experiments. *Adapted from Gebbie *et al.*

dotted bars correspond to peptoids deposited symmetrically onto both mica surfaces (Fig. 2.2, inset, right). The Dopa peptoid separation force did not depend on the deposition method, that is, asymmetric and symmetric deposition of the Dopa peptoid resulted in the same separation force. However, the forces mediated by the Phe and Tyr peptoids did depend on deposition symmetry: a film of Phe peptoid deposited asymmetrically mediated lower separation force than films of Phe peptoid deposited symmetrically, and a film of Tyr peptoid deposited asymmetrically mediated a larger separation force than symmetric Tyr peptoid films.

By comparison, the orange bars in Figure 2.2 show separation forces mediated by the peptide analogs studied by Gebbie *et al.*¹⁶ Because these peptides never deposit as monomolecular films the separation forces did not depend on the deposition method. Each bar is shown as both solid and dotted to indicate that asymmetric or symmetric depositions had the same outcome.

Overall, the range of observed peptoid forces is similar to the reported peptide forces. However, whereas measured separation forces (F) in the peptides *decreased* with increasing hydroxylation i.e. $F_{\text{Phe}} > F_{\text{Tyr}} \geq F_{\text{Dopa}}$, in the asymmetric peptoid films, the opposite trend occurred: $F_{\text{Phe}} < F_{\text{Tyr}} < F_{\text{Dopa}}$. In particular, the separation force measured for the asymmetrically deposited Phe peptoid was only ~25% of measured Phe-peptide force, whereas the Dopa peptoids were at least two-fold more adhesive than the Dopa peptides.

Peptoids deposited symmetrically showed a different trend: Phe peptoid separation forces did not differ significantly from those of the Phe peptide. Similarly, the separation force measured for the Tyr peptoid was not significantly different from the force measured for the Tyr peptide. However, symmetric Dopa peptoid films >2-fold higher separation forces than the corresponding Dopa peptide.

In addition to the values for the adhesive/cohesive forces, the force vs. distance profiles ($F(D)/R$) revealed that the peptoids adsorbed as minimally compressible films. Because our deposition technique (see Methods section) required removal of mica surfaces from the SFA, a specific film thickness at maximal compression (a film's hard wall) was not measurable. However, the relative behavior of the films while under compression was quite accurate. Representative compression runs for each peptoid are depicted in Figure 2.3A and the curves are shifted along the abscissa for clearer comparison of their shapes and profiles. The slopes for the three peptoids are nearly identical and are uniformly steeper than either those of the peptoid-free salt solution (Fig. 2.S1) or those measured for the peptide films (Fig. 2.S2), which were found to be diffuse and hydrated multilayers.¹⁶ This suggests that the peptoids form more compact and less hydrated films than their peptide counterparts.

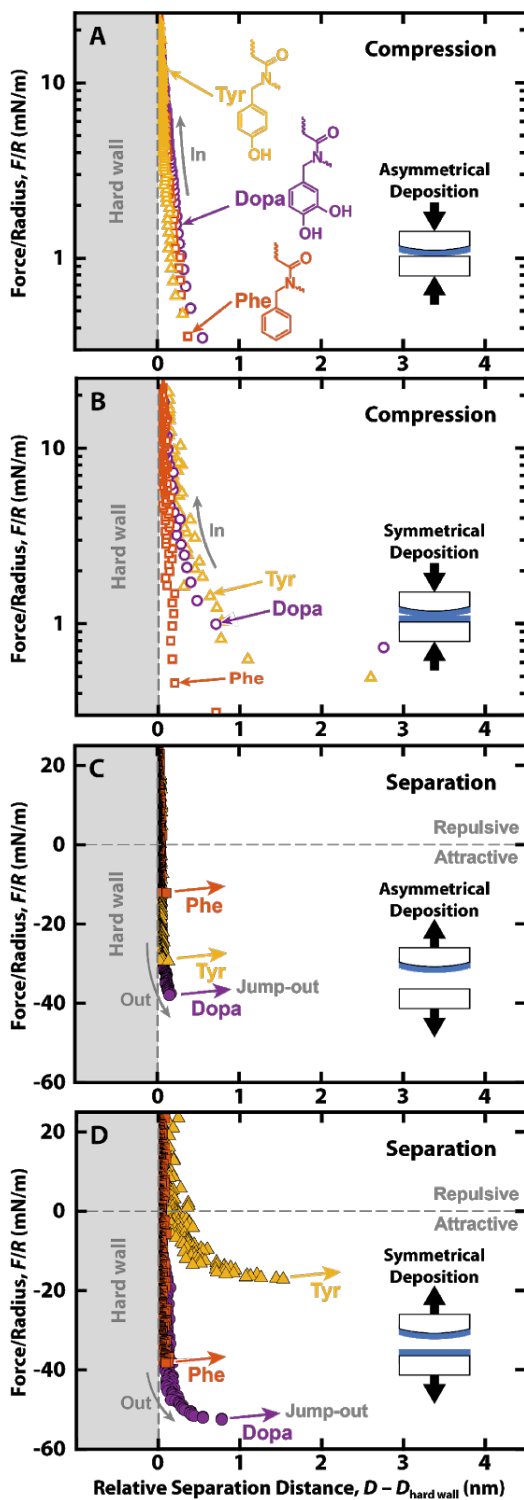


Figure 2.3. Representative force curves of peptoids. Peptoid molecules reveal low compressibility and low hydration. The force versus distance profiles for Phenylalanine, Tyrosine, and Dopa peptoids show behavior when the molecules were deposited in an asymmetrical fashion (A,C) as well as in a symmetrical fashion (B,D) between mica surfaces. We were unable to determine absolute peptoid film thicknesses from the hard-wall distance ($D_{\text{hard-wall}}$), and we therefore present relative distances, $D - D_{\text{hard-wall}}$, near maximum compression, in order to provide meaningful alternative comparisons. The compression curves (A, B) are represented with a log scale on the ordinate axis to highlight exponential features reminiscent of double-layer and hydration decay lengths.

Symmetric peptoid films were slightly more compressible (Fig. 2.3B) perhaps because more peptoid material was deposited. Representative separation/decompression runs for the same molecules are shown in Figure 2.3C-D. The separation curves show small amounts of bridging between the surfaces before separation, commonly observed for polymeric molecules.

The surface and molecular binding properties of Dopa-containing peptides are greatly influenced by the H-bonding and cation- π tendencies of Dopa. By extension, similar tendencies are expected for peptoids but need to be tested. By exposing symmetric Dopa peptoid films in the SFA to solutions of constant pH with increasing ionic strength, we controlled electrostatic screening. If the Dopa peptoids failed cohesively at high ionic strengths, then cohesive forces would likely be cation- π interactions, which, consistent with other coulombic forces, depend on ionic strength.⁴⁴ Figure 2.4 shows the dependence of Dopa peptoid adhesion force on ionic strength. In these experiments, the Dopa peptoid was deposited using a KNO₃-free solution. The KNO₃ concentration was then incrementally increased by flushing the intervening capillary between the mica surfaces with 3-5 ml of peptoid-free solution to a new KNO₃ concentration and allowed to equilibrate for >30 min. The adhesive strength of the Dopa peptoid at all conditions remained remarkably similar to that of bare mica surfaces in KNO₃-free solution. Because of this, we also measured the adhesion of bare mica at all salt concentrations. The data are plotted normalized to the bare mica adhesion force without KNO₃ to minimize the effect of geometrical differences on adhesion strength between the contact points. The adhesive performance of the Dopa peptoid between mica surfaces decreased more slowly than that of bare mica surfaces, reaching about 50% of its 0 mM KNO₃ value when finally equilibrated to 250 mM KNO₃ (Fig. 2.4). To rule out surface contamination as the cause of adhesion loss with increasing salt concentration in

the bare mica experiments, reversibility was tested for both mica-mica replicates by flushing the surfaces with alternating 0 M and 250 M KNO_3 solutions. The first bare mica replicate (dark gray) showed reproducible adhesion reversibility over two cycles while the second replicate (light gray) only partially recovered the initial 0 M adhesion force.

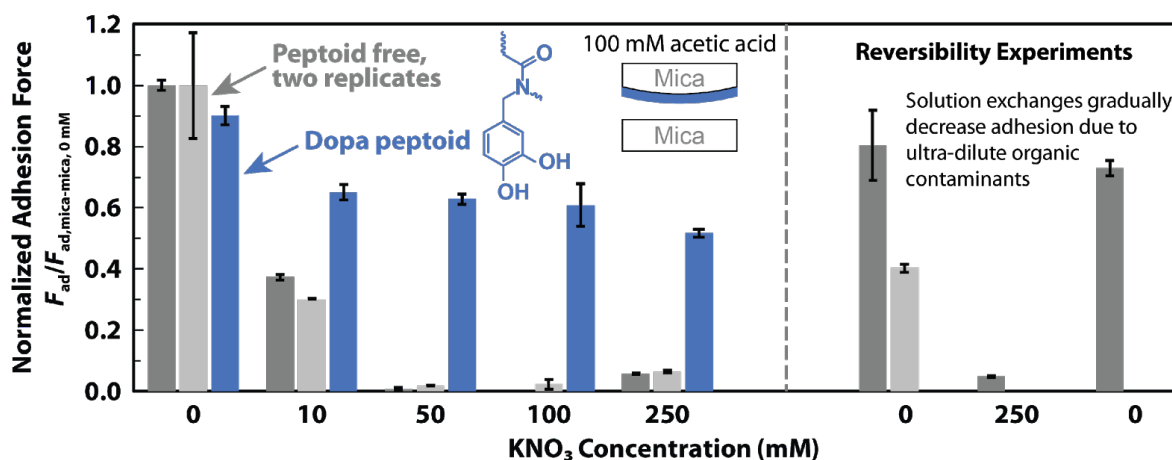


Figure 2.4. Effect of ionic strength on Dopa peptoid adhesion. Adhesion forces for asymmetrically deposited Dopa peptoid films in 100 mM acetic acid and 0, 10, 50, 100, and 250 mM KNO_3 (blue bars) compared with the adhesion forces for peptoid-free mica surfaces (two replicates at the same conditions are represented by two separate sets of light and dark gray bars). Experiments of the same color bars are chronological (*l to r*), with solution changes between each set of measurements. In each case, the measured F_{ad} is normalized by the force of adhesion for the bare mica surfaces (before peptoid deposition) in 100 mM acetic acid without KNO_3 . The ‘Reversibility Experiments’ demonstrate that partial recovery of the KNO_3 -free bare-mica adhesion is possible over multiple cycles between high and low salt conditions.

iii. Molecular Dynamics

To gain insight into the adhesion mechanisms, we performed REMD simulations of each paired peptide/peptoid in bulk water and on mica surfaces. Figure 2.5A shows a snapshot of the most likely conformation adopted by each molecule in bulk water, with the other top 3 structures shown in the supplementary Figure 2.S3. In each panel, the probability that the molecule adopts a conformation belonging to the most populated cluster is given in the upper

left-hand corner. Overall, the most representative structures adopted by either peptides or peptoids leads to the exposure of the Lys residues to solution. Figure 2.5B shows the distribution of the radius of gyration (R_g) versus the maximum distance (R_{max}) between any of the backbone atoms. The lower R_g and R_{max} observed for peptoids indicates more compact structures. The Phe peptoid adopted structures that attempt to bury hydrophobic phenylalanine rings and expose the Lys residues, while the Dopa peptoid favors the maximum exposure of Dopa and Lys residues, leading to the most compact structure of all three peptoid variants (Fig. 2.5B). Peptoids are primarily random-coils, whereas the peptides showed some regions of stable β -sheets (Fig. 2.5A and supp. Fig. 2.S4 and 2.S5) and present higher values for R_g and R_{max} as a consequence of forming β -sheets. We performed CD spectroscopy on the Phe and Tyr peptides to investigate their secondary structure (Supp. Fig. 2.S6 and 2.S7). The spectra for Phe and Tyr showed positive ellipticity at 220 and 230 nm, respectively, and the ellipticity became negative at lower wavelengths. The solution spectra are consistent with right-hand twisted β -sheets⁴¹. The secondary structure prediction of each peptide generated by the BeStSel algorithm indicates both peptides have significant antiparallel β -sheet content (Supp. Table 2.S1) which agrees with our simulations (Fig. 2.5A, 2,5B).

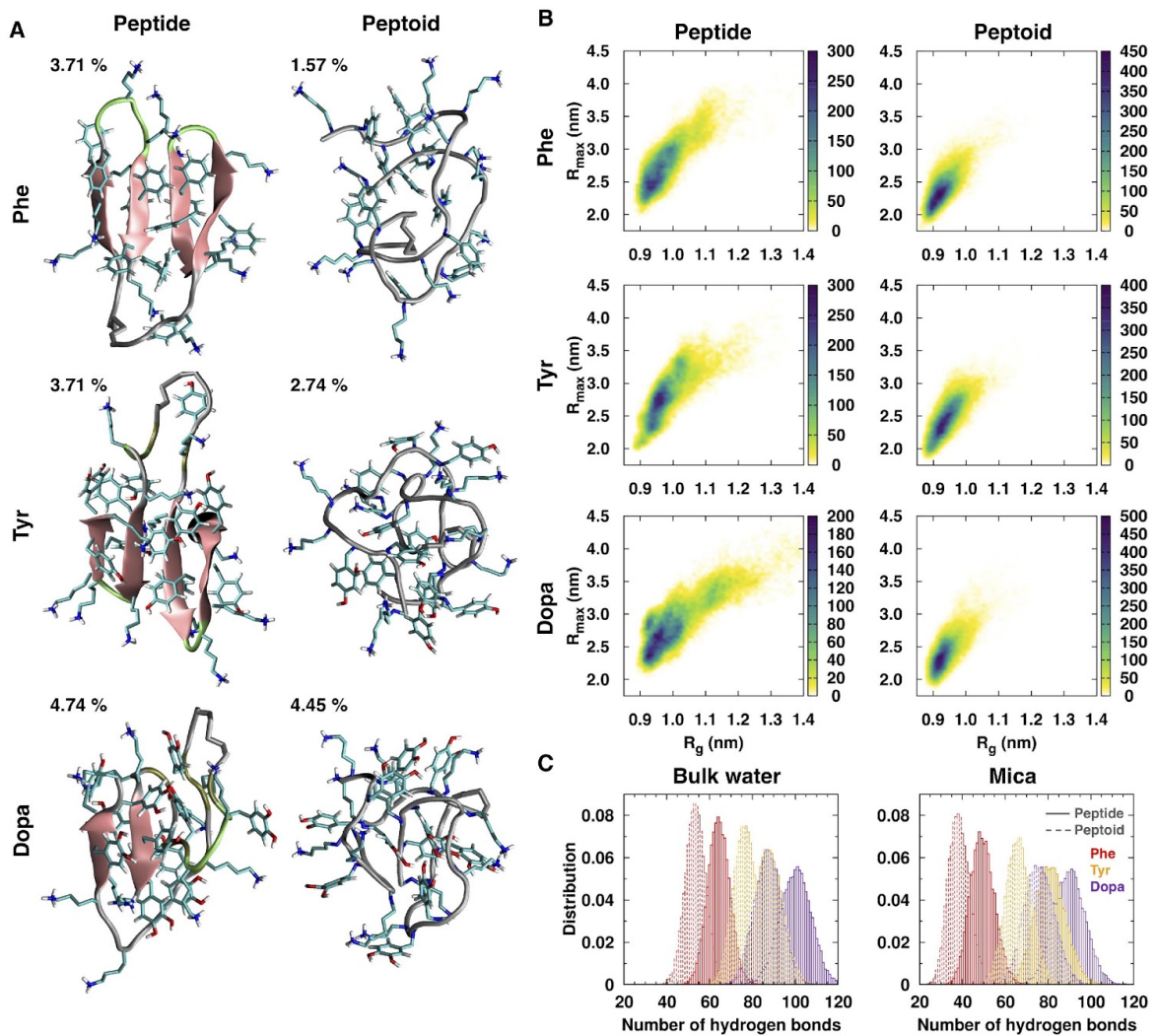


Figure 2.5. REMD simulations of peptoid and peptide conformation. A) Shown are the most representative conformations of all peptide and peptoid homologues in bulk water. The percentage of structures present in the most populated cluster are shown in the *top left*. (a total of 15,000 structures were analyzed). The secondary structure is shown (*pink*) with β -sheet formation indicated by wide arrows pointing from the N- to C-terminal. β -sheet formation is seen only in the peptide backbones. Atoms are color coded as N: *blue*; H: *white*; C: *cyan*; O: *red*. B) 2D Distribution of the radius of gyration vs. the maximum distance measured within any backbone atoms. C) Normalized histogram of the number of hydrogen bonds in between the water molecules and the peptides/peptoids in bulk water (left) and on mica (right). All analyses were done for every 20 ps for the last 300 ns of simulations.

The Phe and Tyr peptoids present smaller probabilities for the most representative clusters and large numbers of clusters of likely conformations (Supp. Table 2.S2), indicating that they sample a larger conformational space and their structures are broadly distributed

among their clusters than the peptides. Although peptides have a higher number of hydrogen bonds, likely due to the secondary amines of peptoids (supp. Fig. S4; S5 and Fig. 2.6C), the Dopa peptoid showed several clusters and the probability for its most representative cluster was comparable with the ones observed for peptides (Fig. 2.5A and supp. Table. 2.S2). This is likely due to hydrophobic interactions within the backbone and the heightened exposure of Dopa and Lys to the solvent. We also examined peptoid vs peptide hydration in solution and found each peptoid to be less hydrated than its peptide counterpart (Fig. 2.5C).

To provide insight into the molecular scale forces driving adsorption we modeled the structure of the peptides and peptoids on a mica surface and monitored the number of phenolic and Lys side-chains in close proximity with the surface. More Lys residues were recruited to the surface than phenolic groups (Fig. 2.6A, B and Supp. Fig. 2.S8). A snapshot of the most likely conformation adopted by each molecule is shown in Fig. 2.6A, and the top 3 structures are shown in supplementary Fig. 2.S9. The probability that the molecule adopts a conformation belonging to the most populated cluster is listed in the upper left-hand corner of Fig. 2.6A. Compared with the simulations without mica, the lower number of total clusters (Supp. Table 2.S2) and the higher probabilities of the most stable cluster in each simulation indicate that the bound structures are more stable than in bulk water.

Fig. 2.6B shows the distributions of the number of Lys recruited to the surface and radius of gyration along the z-axis, which reflects the spread over the surface plane (x-y plane). The Dopa peptide recruited the fewest Lys residues to the surface and presented the lowest values for $R_{g(z)}$. The Dopa peptide also had low R_g and R_{max} (Supp. Fig. 2.S10), indicating a compact conformation on mica. This behavior can be explained in terms of the peptide's higher intramolecular hydrogen bonding (Fig. 2.6C) and hydrophilicity. The Phe and Tyr

peptides and Dopa peptoid spread on the surface with roughly 11 Lys residues on the mica. The Phe peptoid showed between 10-12 Lys residues on the surface and lower $R_{g(z)}$ values, reflecting its compact structures (also see distribution of R_g vs R_{max} in Supp. Fig. 2.S10).

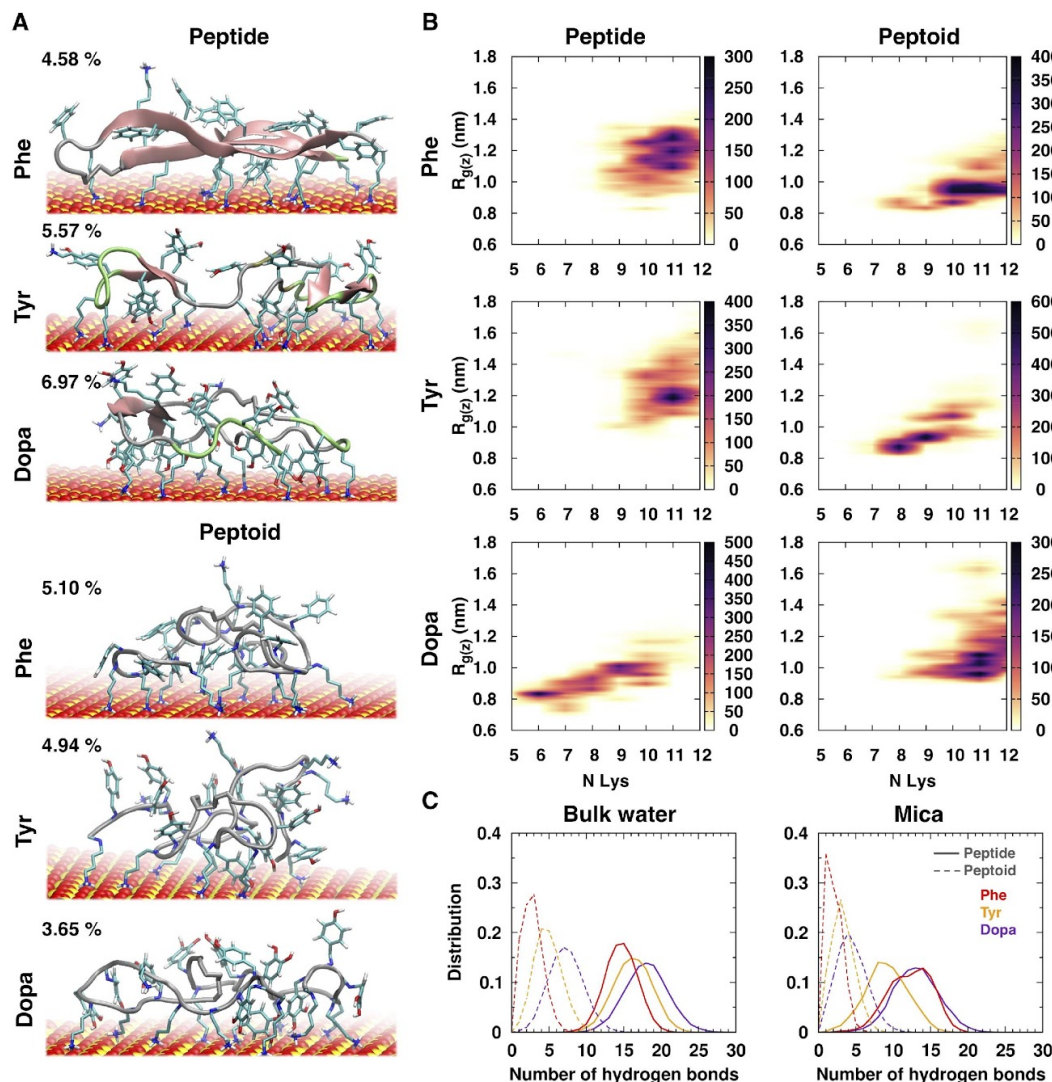


Figure 2.6. REMD simulations of hydrogen bonding. A) Shown are the most representative conformations of all peptide and peptoid homologues in the presence of water. The percentage of structures present in the most populated cluster is shown in the *top left* (a total of 15,000 structures were analyzed). The secondary structure is shown (*pink*) with β -sheet formation indicated by wide arrows having an N- to C-terminal orientation. Atoms are color coded as N: *blue*; H: *white*; C: *cyan*; Si: *yellow*; O: *red*; Al: *orange*. B) 2D Distribution of the number of Lys close to mica ($r < 3 \text{ \AA}$) vs. the radius of gyration along z-axis. C) Normalized histogram of the number of intra-molecular hydrogen bonds in bulk water and on mica surface. All analyses were done for every 20 ps for the last 300 ns of simulations.

Following surface adsorption, all molecules showed reduced hydrogen bonding with the solvent (Fig. 2.5C). Of the adhesive peptides and peptoids considered, the Dopa and Tyr peptides were the most hydrated. Of note is that the secondary structures of Tyr and Dopa peptide unfold most with just a few residues stabilizing β -sheets, whereas the Phe peptides only partially unfold, retaining some secondary structure (Supp. Figures 2.S4; 2.S5).

Considering the results obtained by the SFA experiments, the lower cohesion observed for Dopa peptide is correlated with higher hydration and intramolecular interactions, and its adoption of a compact structure. Similarly, the higher cohesion forces measured for the Phe- and Dopa peptoids can be explained in terms of their lower hydration, lack of backbone-mediated intramolecular hydrogen bonds, and their ability to spread over the surface, which exposes the aromatic groups.

Given the complexity of the experimental system with many more molecules, longer time scales, and the myriad of aggregate-forming binding states for peptides/peptoids, we acknowledge that MD simulations have limitations. However, the simulations give us important insights about the mechanisms involved in the adhesion process. Our simulations and experiments concur to the extent that the higher flexibility of peptoids and their inability to form secondary structures provide a barrier against multilayer formation. In addition, the lower hydration of peptoids and their compact structures is consistent with their relative behavior to peptide films.

D. Discussion

Most synthetic mussel-inspired adhesive polymers lack mussel-specific sequences and a polypeptide backbone.^{45,46} Consequently, how backbone chemistry impacts adhesion in mussel-inspired systems is rarely investigated. Our results show that even when specific

sequences are maintained, subtle changes in backbone chemistry can result in profoundly different adhesive behaviors. We attribute these differences between peptoids and peptides to differences in adsorption. Whereas peptides deposit as multilayers, our results suggest that peptoids deposit on mica surfaces as monomolecular films or nearly so. As a result, asymmetric and symmetric deposition can result in different failure modes and separation forces.

The dependence of the separation forces on the deposition method for Phe and Tyr peptoids gives an indication of the failure mode. The separation force for symmetric Phe was 3-fold greater than for asymmetric Phe, and the separation force for symmetric Tyr was $\sim 2/3$ that of asymmetric Tyr. We propose that the changing forces correspond to changing failure modes, namely, asymmetric deposition resulted in adhesive failure, whereas symmetric deposition resulted in cohesive failure. The influence of film symmetry on the failure mode implies that the Phe and Tyr peptoids adsorb as monolayers where a monolayer is defined as a film that is on average one molecule thick. Each of the previously studied peptides deposited as monolayers and failed cohesively, regardless of deposition symmetry. In that case, the separation force would be independent of the deposition method, as reported by Gebbie *et al.*¹⁶ If, like the peptides, peptoids deposited as multilayers, then cohesive failure would be expected after both asymmetrical and symmetrical deposition. In that case, the separation force measured for the peptoids would also be independent of the deposition method. In that case, the separation force would be independent of the deposition method, as reported by Gebbie *et al.*¹⁶

That Phe and Tyr peptoids adsorb as monolayers is further supported by the compressibility of the adsorbed peptoid films. The relatively steep slopes of the force-distance

curves upon compression are consistent with less hydrated peptoid monolayers adsorbed to mica, in contrast with the previously studied peptides that formed hydrated multilayers (Fig. 2.3A,B, Fig. 2.S2). Our simulations show that the peptoids have significantly fewer water molecules than the analogous peptides in their first hydration layer (Fig. 2.5C), consistent with differing levels of hydration between peptoid and peptide films.

Finally, the separation forces for Phe peptoids deposited symmetrically are the same as the Phe peptides. Similarly, Tyr peptoids deposited symmetrically yield the same separation force as the Tyr peptides. These similarities suggest that the functional groups determine the strength of cohesive interactions between the macromolecules and support the assertion that symmetric deposition of Phe and Tyr peptoids results in cohesive failure, like the analogous Phe and Tyr peptides. Given the consistency between the symmetrically deposited Phe and Tyr peptoid with their analogous peptides, the molecular nature of the interactions is assumed to be the same for each class of molecule – namely a combination of hydrophobic interactions, hydrogen bonding (in Tyr species), and a significant contribution of cation- π interactions which decay with increasing side-chain ring hydroxylation. Figure 2.7 depicts a model of these interactions for the Phe and Dopa peptoids.

In contrast with the deposition-dependence of the separation forces for Phe and Tyr peptoids, the separation forces mediated by Dopa peptoids after asymmetric and symmetric deposition were the same. Furthermore, both symmetric and asymmetric deposition of Dopa peptoids resulted in significantly higher separation forces than the force mediated by the analogous Dopa peptide. We propose two explanation for this behavior. First, adhesive bridging contributes to the performance of the Dopa peptoid films, irrespective of the deposition method. Such adhesive failure, even after symmetric deposition, is possible if the

binding functionalities (likely Dopa hydroxyls and lysyl pendant amines) on one surface penetrate the film on the other surface and bind to the underlying mica layer (Fig. 2.7, bottom right). In that situation, some of the individual peptoid molecules bind to both surfaces, guaranteeing adhesive contributions to the failure mechanism. Similar behavior has been seen previously in a study of small molecules with similar catechol and amine binding functionalities.⁴⁷ This scenario is more likely for the Dopa peptoid than either of the other species for two reasons i) the available Dopa-mica binding interactions are more energetically favorable than Phe-mica or Tyr-mica interactions, ii) the REMD simulations demonstrate that Dopa peptoids extend slightly further from the mica surface than Phe and Tyr peptoids (Fig. 2.6B). An adhesive component of failure strongly suggests that the Dopa peptoid adsorbs as monolayers on the mica surface (Fig. 2.7, bottom left), since multilayers would present a steric barrier to the formation of bridging interactions. That Dopa peptoids adsorb as monolayers is further supported by the similar compression profiles of Dopa, Tyr, and Phe peptoids in either deposition method.

Second, we note that the separation force for Dopa peptoids deposited symmetrically likely includes some contribution from cohesive interactions in addition to adhesive bridging interactions, and that the cohesive interactions are strengthened relative to the Dopa peptide due to the dehydrated state of the peptoid films. The diminished hydration in Dopa peptoid films means there are fewer water molecules to compete for hydrogen bonding with the catechol moieties. This enables stable bidentate hydrogen bonds to rapidly form between catechol side chains (Fig. 2.7), which have previously been shown to produce strong cohesive interactions.^{48,49} Reduced hydration in combination with the lack of intramolecular hydrogen bonds allowed the Dopa peptoid to better spread over the surface, leaving the side chains more

available to form cohesive and adhesive interactions, as observed in our simulations. The proposed ability of the Dopa peptoid monolayers to form both strong bridging adhesive interactions (unlike the peptide multilayers), and strong cohesive interactions due to the peptoid dehydration, are consistent with the greater separation forces measured for peptoids than peptides after both symmetric and asymmetric deposition.

The formation of dehydrated monolayers rather than hydrated multilayers may be understood as follows: The reduced number of interactions between peptoids and water molecules through hydrogen bonds (Fig. 2.5C) is expected because removal of the amide hydrogen results in a more hydrophobic backbone that also lacks intramolecular hydrogen bonding. Additionally, increased conformational freedom allows peptoids to adopt more compact structures having collapsed backbones. We found that Phe peptide adopts β -sheet conformations both in solution and when presented with a mica surface that may contribute to multilayer formation.^{50,51} Phe and Tyr peptides spread over the mica surface and orient most of their aromatics rings upward, which could favor the stacking of molecules. In addition, the larger number of conformational clusters generated by the peptoids on mica is evidence of their flexibility and disorder, which in turn obstructs the formation of diffuse, hydrated, multilayers.

The dependence of the separation force mediated by the Dopa peptoid on the solution ionic strength also provides information about the relative magnitudes of interactions responsible for adhesion. At the highest salt concentration tested (250 mM KNO₃), forces due to coulombic interactions are expected to be significantly reduced. Possible adhesive interactions include Dopa hydrogen bonding to the mica surface, complexation of aluminum atoms in the mica lattice by Dopa, and Lys-mica bridging, of which only the Lys-mica

interactions would depend strongly on ionic strength. Previous results from MD simulations showed that bi-dentate interaction between Dopa residue and mica is a strong interaction that persists throughout the simulation and presents an average length comparable to a coordination bond length, leading to a hydrogen bond lifetime about 20 times higher than the one observed for the Dopa-surface interaction mediated by water molecules or Lys residues (Supp Fig. 2.S11). Possible cohesive forces include cation- π interactions, hydrophobic interactions, quadrupole interactions, and Dopa-Dopa hydrogen bonding between the peptoid films. Covalent adhesive and cohesive interactions like oxidative quinone coupling and Dopa coordination bonding can be ruled out based on the reversible separation forces measured in our experiments. Because increasing ionic strength reduced the separation force by up to half (Fig. 2.4), we conclude that non-Coulombic interactions contribute to approximately half the separation forces, consistent with earlier reports asserting the importance of electrostatic interactions¹² and Dopa-mediated bidentate H-bonds⁵² for adhesion of mussel proteins.

These conclusions about the adsorption behaviors, failure modes, and likely interactions for films of peptoids and peptides account for the trends in separation forces presented in Figure 2.2. We find that for peptoids deposited asymmetrically, the separation force increases with increasing ring hydroxylation from Phe to Tyr to Dopa, consistent with the contribution of hydrogen bonds generating adhesive and cohesive interactions. In the case of the Phe peptoid with the most Lys committed to binding the first surface, an asymmetric Phe peptoid film presents a hydrophobic, Phe-rich face to the second mica surface and forms few hydrogen bonds, resulting in weak adhesion (Fig. 2.6A). Asymmetrically deposited Tyr and Dopa peptoids mediate greater adhesion due to the ability of the Tyr and Dopa sidechains to form hydrogen bonds, as well as the greater number of unbound Lys available to bind to the other

mica surface (Fig. 2.6C). The Dopa substituted peptoid yielded strong separation forces for both symmetric and asymmetric deposition due to a combination of adhesive bridging interactions and enhanced cohesion due to dehydration.

In contrast, Gebbie *et al.* found decreasing separation force with increasing ring hydroxylation, but the separation forces reported in that work corresponded to cohesive failure rather than adhesive failure and are consistent with the cohesive forces measured here for symmetrically deposited Phe and Tyr peptoids. The relatively strong cohesion of the Phe macromolecules likely resulted from the geometry: with Lys down on mica and Phe up toward solvent in films on both surfaces, the peptoid and peptide films cohere via hydrophobic interactions and π - π coupling between phenyl groups, and cation- π bonding between phenyl groups and lysine groups not bound to the mica surface. The hydroxyl group in the Tyr peptoid and peptide is expected to lower the strength of hydrophobic and cation- π interactions.¹⁶ Finally, the multilayers of the Dopa peptide inhibit bridging adhesion and the presence of water interferes with the formation of stronger interactions as discussed above.

It is not surprising that the incorporation of Dopa into different polymer systems may produce variable results. Mfp-5 is a surface primer whose sequence is rich in Dopa (up to 30-mol%),¹ and proteins such as this have inspired numerous synthetic catechol-functionalized adhesive polymers. The synthetic systems have met with variable success in part because they may not recapitulate the context or conditions present in the mussel plaque. Dopa is a reactive side-chain *in vitro* but in the adhesive plaques Dopa redox is maintained regardless of the ambient solution conditions.⁵³ The protein cohort forming the adhesive plaque is deposited as a coacervate phase at low pH <5.⁹ Protein coacervates resemble peptoids in that during liquid-liquid phase separation both release significant H₂O.⁵⁴ This is also consistent

with work suggesting that Dopa residues in Mfp-3 variants are shielded from the aqueous phase by being nested in a hydrophobic environment.⁵⁵ In a similar fashion, the peptoids used in this study, unlike their peptide counterparts, deposit with a lower degree of hydration and consequently enable strong Dopa-mediated adhesion and cohesion despite having the same sequence of functional groups and an analogous polyamide backbone. It must be emphasized that mica was the only substrate used in this study and that the basic region of mfp-5 (characterized by high Dopa, Lysine, and Glycine) was the only sequence tested. Other domains in mfp-5 have different charge characteristics with lower adhesion on mica.¹²

The peptoids used in this study showed very different adsorption behavior from their peptide counterparts, and a different balance of adhesion and cohesion, despite having the same sequence of functional groups and an analogous polyamide backbone. These results demonstrate that small changes in backbone structure and hydration influence molecular conformations, adsorption, and ultimately adhesive function, and provide insight into the design rules and processing conditions for optimizing the performance of mussel-inspired adhesives.

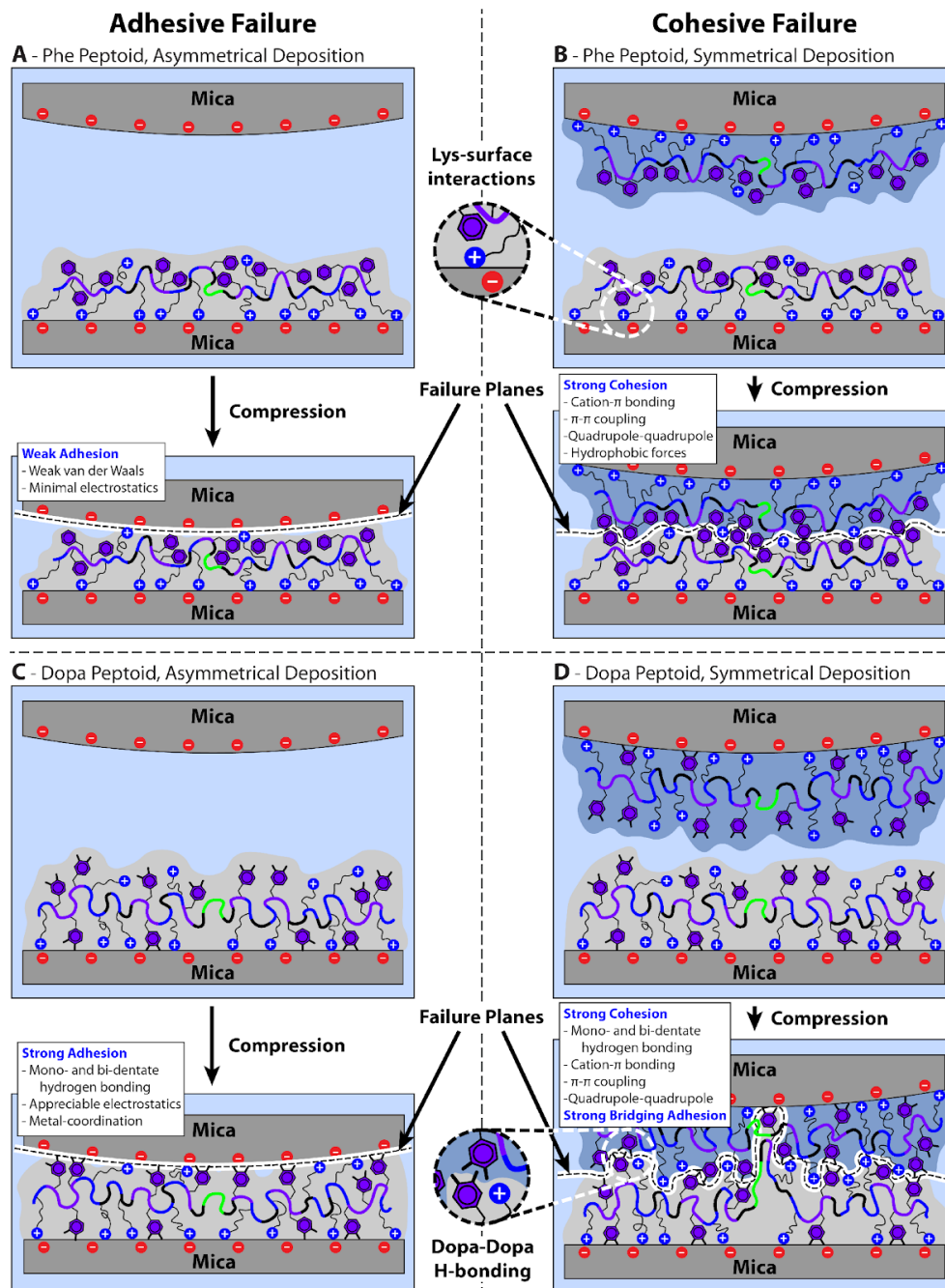


Figure 2.7. Model depicting peptoid adhesion vs. cohesion. Scheme of peptoid films before and after compression for asymmetrical deposition of the Phe peptoid (A), symmetrical deposition of the Phe peptoid (B), asymmetrical deposition of the Dopa peptoid (C), symmetrical deposition of the Dopa peptoid (D). In all cases, asymmetrical deposition leads to adhesive failure. Symmetrical deposition results in cohesive failure for Phe peptoids (and Tyr peptoids, not depicted) and a combination of cohesive/adhesive failure for Dopa peptoids. Failure planes are indicated by black dashed lines overlaid onto solid white lines. The “boundaries” of each peptoid molecule are indicated with either blue or gray shaded regions. The important interactions at each failure plane are indicated in the white boxes above each ‘compressed’ pair of surfaces.

E. Conclusion

We have established that mussel-inspired peptoids having high aromatic, lysine, and glycine contents can achieve cohesive strengths comparable with those of analogous peptides and proteins from which they derive. Our investigation has shown that even a subtle change in backbone chemistry can generate profound effects on the behavior and performance of mussel-inspired adhesives. Increased backbone hydrophobicity and inability to form stable secondary structure allow the peptoids to better deposit as thin incompressible films of reduced hydration than peptides of similar sequence. Following asymmetric film deposition, peptoid adhesive strength is positively correlated with increasing ring hydroxylation due to increased flexibility and hydrogen bonding. In symmetric films, the Phe and Tyr peptoids exhibited similar cohesion forces as their peptide analogs. The Dopa peptoid, however, shows greater cohesion than its peptide counterpart due to film dehydration, lower backbone-mediated intramolecular hydrogen bonding and surface spreading ability. This emphasizes the importance of processing conditions when designing mussel-inspired adhesives.

Peptoid molecules have potential to improve applications for wet adhesion. Though peptides may be classified as ‘intrinsically disordered’, the backbone chemistry and structure may still influence their molecular properties. If such backbone interactions are undesirable for specific applications, such as selective surface priming, peptoid molecules can be used to maintain side chain function without the complication of backbone interactions. Then, intermolecular ordering can be engineered through specific side-chain interactions to tailor a peptoid structure based on a desired function.

F. References

- (1) Lee, B. P.; Messersmith, P. B.; Israelachvili, J. N.; Waite, J. H. Mussel-Inspired Adhesives and Coatings. *Annu. Rev. Mater. Res.* **2011**, *41*, 99–132. <https://doi.org/10.1146/annurev-matsci-062910-100429>.
- (2) Florioli; von Langen J; Waite. Marine Surfaces and the Expression of Specific Byssal Adhesive Protein Variants in *Mytilus*. *Mar. Biotechnol. (NY)*. **2000**, *2* (4), 352–363.
- (3) Hofman, A. H.; van Hees, I. A.; Yang, J.; Kamperman, M. Bioinspired Underwater Adhesives by Using the Supramolecular Toolbox. *Adv. Mater.* **2018**, *30* (19), 1704640. <https://doi.org/10.1002/adma.201704640>.
- (4) Lee, H.; Scherer, N. F.; Messersmith, P. B. Single-Molecule Mechanics of Mussel Adhesion. *Proc. Natl. Acad. Sci. U. S. A.* **2006**, *103* (35), 12999–13003. <https://doi.org/10.1073/pnas.0605552103>.
- (5) Kord Forooshani, P.; Lee, B. P. Recent Approaches in Designing Bioadhesive Materials Inspired by Mussel Adhesive Protein. *J. Polym. Sci. Part A Polym. Chem.* **2017**, *55* (1), 9–33. <https://doi.org/10.1002/pola.28368>.
- (6) Kim, S.; Faghihnejad, A.; Lee, Y.; Jho, Y. S.; Zeng, H.; Hwang, D. S. Cation- π Interaction in DOPA-Deficient Mussel Adhesive Protein Mfp-1. *J. Mater. Chem. B* **2015**, *3* (5), 738–743. <https://doi.org/10.1039/c4tb01646g>.
- (7) Das, S.; Rodriguez, N. R. M.; Wei, W.; Waite, J. H.; Israelachvili, J. N. *Peptide Length and Dopa Determine Iron-Mediated Cohesion of Mussel Foot Proteins*; Wiley-Blackwell, 2015; Vol. 25, pp 5840–5847. <https://doi.org/10.1002/adfm.201502256>.
- (8) Yu, J.; Wei, W.; Menyo, M. S.; Masic, A.; Waite, J. H.; Israelachvili, J. N. Adhesion of Mussel Foot Protein-3 to TiO₂ Surfaces: The Effect of PH. *Biomacromolecules* **2013**, *14* (4), 1072–1077. <https://doi.org/10.1021/bm301908y>.
- (9) Rodriguez, N. R. M.; Das, S.; Kaufman, Y.; Israelachvili, J. N.; Waite, J. H. Interfacial PH during Mussel Adhesive Plaque Formation. *Biofouling* **2015**, *31* (2), 221–227. <https://doi.org/10.1080/08927014.2015.1026337>.
- (10) Lu, Q.; Danner, E.; Waite, J. H.; Israelachvili, J. N.; Zeng, H.; Hwang, D. S. Adhesion of Mussel Foot Proteins to Different Substrate Surfaces. *J. R. Soc. Interface* **2013**, *10* (79). <https://doi.org/10.1098/rsif.2012.0759>.
- (11) Levine, Z. A.; Rapp, M. V; Wei, W.; Mullen, R. G.; Wu, C.; Zerze, G. H.; Mittal, J.; Waite, J. H.; Israelachvili, J. N.; Shea, J.-E. Surface Force Measurements and Simulations of Mussel-Derived Peptide Adhesives on Wet Organic Surfaces. *Proc. Natl. Acad. Sci.* **2016**, *113* (16), 4332–4337. <https://doi.org/10.1073/pnas.1603065113>.
- (12) Wei, W.; Yu, J.; Gebbie, M. A.; Tan, Y.; Martinez Rodriguez, N. R.; Israelachvili, J. N.; Waite, J. H. Bridging Adhesion of Mussel-Inspired Peptides: Role of Charge,

- Chain Length, and Surface Type. *Langmuir* **2015**, *31* (3), 1105–1112.
<https://doi.org/10.1021/la504316q>.
- (13) Rapp, M. V.; Maier, G. P.; Dobbs, H. A.; Higdon, N. J.; Waite, J. H.; Butler, A.; Israelachvili, J. N. Defining the Catechol-Cation Synergy for Enhanced Wet Adhesion to Mineral Surfaces. *J. Am. Chem. Soc.* **2016**, *138* (29), 9013–9016.
<https://doi.org/10.1021/jacs.6b03453>.
- (14) Yu, J.; Kan, Y.; Rapp, M.; Danner, E.; Wei, W.; Das, S.; Miller, D. R.; Chen, Y.; Waite, J. H.; Israelachvili, J. N. Adaptive Hydrophobic and Hydrophilic Interactions of Mussel Foot Proteins with Organic Thin Films. *Proc. Natl. Acad. Sci. U. S. A.* **2013**, *110* (39), 15680–15685. <https://doi.org/10.1073/pnas.1315015110>.
- (15) Hwang, D. S.; Waite, J. H. Three Intrinsically Unstructured Mussel Adhesive Proteins, Mfp-1, Mfp-2, and Mfp-3: Analysis by Circular Dichroism. *Protein Science*. 2012, pp 1689–1695. <https://doi.org/10.1002/pro.2147>.
- (16) Gebbie, M. A.; Wei, W.; Schrader, A. M.; Cristiani, T. R.; Dobbs, H. A.; Idso, M.; Chmelka, B. F.; Waite, J. H.; Israelachvili, J. N. Tuning Underwater Adhesion with Cation– π Interactions. *Nat. Chem.* **2017**, *9* (5), 473–479.
<https://doi.org/10.1038/nchem.2720>.
- (17) Kirshenbaum, K.; Barron, A. E.; Goldsmith, R. A.; Armand, P.; Bradley, E. K.; Truong, K. T. V.; Dill, K. A.; Cohen, F. E.; Zuckermann, R. N. Sequence-Specific Polypeptoids: A Diverse Family of Heteropolymers with Stable Secondary Structure. *Proc. Natl. Acad. Sci. U. S. A.* **1998**, *95* (8), 4303–4308.
<https://doi.org/10.1073/pnas.95.8.4303>.
- (18) Huang, K.; Wu, C. W.; Sanborn, T. J.; Patch, J. A.; Kirshenbaum, K.; Zuckermann, R. N.; Barron, A. E.; Radhakrishnan, I. A Threaded Loop Conformation Adopted by a Family of Peptoid Nonamers. *J. Am. Chem. Soc.* **2006**, *128* (5), 1733–1738.
<https://doi.org/10.1021/ja0574318>.
- (19) Tran, H.; Gael, S. L.; Connolly, M. D.; Zuckermann, R. N. Solid-Phase Submonomer Synthesis of Peptoid Polymers and Their Self-Assembly into Highly-Ordered Nanosheets. *J. Vis. Exp.* **2011**, No. 57. <https://doi.org/10.3791/3373>.
- (20) Wellings, D. A.; Atherton, E. [4] Standard Fmoc Protocols. In *Methods in Enzymology*; Academic Press, 1997; Vol. 289, pp 44–67.
[https://doi.org/10.1016/S0076-6879\(97\)89043-X](https://doi.org/10.1016/S0076-6879(97)89043-X).
- (21) Israelachvili, J.; Min, Y.; Akbulut, M.; Alig, A.; Carver, G.; Greene, W.; Kristiansen, K.; Meyer, E.; Pesika, N.; Rosenberg, K.; Zeng, H. Recent Advances in the Surface Forces Apparatus (SFA) Technique. *Reports Prog. Phys.* **2010**, *73* (3), 036601.
<https://doi.org/10.1088/0034-4885/73/3/036601>.
- (22) Johnson, K. L.; Kendall, K.; Roberts, A. D. Surface Energy and the Contact of Elastic Solids. *Proc. R. Soc. A Math. Phys. Eng. Sci.* **1971**, *324* (1558), 301–313.
<https://doi.org/10.1098/rspa.1971.0141>.

- (23) Van Der Spoel, D.; Lindahl, E.; Hess, B.; Groenhof, G.; Mark, A. E.; Berendsen, H. J. C. GROMACS: Fast, Flexible, and Free. *Journal of Computational Chemistry*. 2005. <https://doi.org/10.1002/jcc.20291>.
- (24) Oostenbrink, C.; Villa, A.; Mark, A. E.; Van Gunsteren, W. F. A Biomolecular Force Field Based on the Free Enthalpy of Hydration and Solvation: The GROMOS Force-Field Parameter Sets 53A5 and 53A6. *J. Comput. Chem.* **2004**, *25* (13), 1656–1676. <https://doi.org/DOI 10.1002/jcc.20090>.
- (25) Dequidt, A.; Devemy, J.; Malfreyt, P. Confined KCl Solution between Two Mica Surfaces: Equilibrium and Frictional Properties. *J. Phys. Chem. C* **2015**, *119* (38), 22080–22085. <https://doi.org/10.1021/acs.jpcc.5b06880>.
- (26) Heinz, H.; Koerner, H.; Anderson, K. L.; Vaia, R. A.; Farmer, B. L. Force Field for Mica-Type Silicates and Dynamics of Octadecylammonium Chains Grafted to Montmorillonite. *Chem. Mater.* **2005**. <https://doi.org/10.1021/cm0509328>.
- (27) Bayly, C. I.; Cieplak, P.; Cornell, W.; Kollman, P. A. A Well-Behaved Electrostatic Potential Based Method Using Charge Restraints for Deriving Atomic Charges: The RESP Model. *J. Phys. Chem.* **1993**, *97* (40), 10269–10280. <https://doi.org/10.1021/j100142a004>.
- (28) Valiev, M.; Bylaska, E. J.; Govind, N.; Kowalski, K.; Straatsma, T. P.; Van Dam, H. J. J.; Wang, D.; Nieplocha, J.; Apra, E.; Windus, T. L.; de Jong, W. A. NWChem: A Comprehensive and Scalable Open-Source Solution for Large Scale Molecular Simulations. *Comput. Phys. Commun.* **2010**, *181* (9), 1477–1489. <https://doi.org/http://dx.doi.org/10.1016/j.cpc.2010.04.018>.
- (29) Das, S.; Lee, B. H.; Linstadt, R. T.; Cunha, K.; Li, Y.; Kaufman, Y.; Levine, Z. A.; Lipshutz, B. H.; Lins, R. D.; Shea, J. E.; Heeger, A. J.; Ahn, B. K. Molecularly Smooth Self-Assembled Monolayer for High-Mobility Organic Field-Effect Transistors. *Nano Lett* **2016**, *16* (10), 6709–6715. <https://doi.org/10.1021/acs.nanolett.6b03860>.
- (30) Berendsen, H. J. C.; Postma, J. P. M.; van Gunsteren, W. F.; Hermans, J. Intermolecular Forces. *Pullman, B., Ed.; Reidel Publ. Co. Dordr.* **1981**, 331–342. <https://doi.org/papers2://publication/livfe/id/165650>.
- (31) Hess, B.; Bekker, H.; Berendsen, H. J. C.; Fraaije, J. G. E. M. LINCS: A Linear Constraint Solver for Molecular Simulations. *J. Comput. Chem.* **1997**, *18* (12), 1463–1472. <https://doi.org/papers2://publication/livfe/id/165645>.
- (32) Hockney, R. W. The Potential Calculation and Some Applications. In *Methods in Computational Physics*; Alder, B., Fernbach, S., Rotenberg, M., Eds.; Academic Press: New York/London, 1970; Vol. 9.
- (33) Darden, T.; York, D.; Pedersen, L. Particle Mesh Ewald: An N·log(N) Method for Ewald Sums in Large Systems. *J. Chem. Phys.* **1993**, *98* (12), 10089–10092. <https://doi.org/doi:http://dx.doi.org/10.1063/1.464397>.

- (34) Hoover, W. G. Canonical Dynamics: Equilibrium Phase-Space Distributions. *Phys. Rev. A* **1985**. <https://doi.org/10.1103/PhysRevA.31.1695>.
- (35) Parrinello, M.; Rahman, A. Polymorphic Transitions in Single Crystals: A New Molecular Dynamics Method. *J. Appl. Phys.* **1981**. <https://doi.org/10.1063/1.328693>.
- (36) Nosé, S.; Klein, M. L. Constant Pressure Molecular Dynamics for Molecular Systems. *Mol. Phys.* **1983**. <https://doi.org/10.1080/00268978300102851>.
- (37) Daura, X.; Gademann, K.; Schäfer, H.; Jaun, B.; Seebach, D.; Van Gunsteren, W. F. The β -Peptide Hairpin in Solution: Conformational Study of a β -Hexapeptide in Methanol by NMR Spectroscopy and MD Simulation. *J. Am. Chem. Soc.* **2001**. <https://doi.org/10.1021/ja003689g>.
- (38) Kabsch, W.; Sander, C. Dictionary of Protein Secondary Structure: Pattern Recognition of Hydrogen-bonded and Geometrical Features. *Biopolymers* **1983**. <https://doi.org/10.1002/bip.360221211>.
- (39) Touw, W. G.; Baakman, C.; Black, J.; Te Beek, T. A. H.; Krieger, E.; Joosten, R. P.; Vriend, G. A Series of PDB-Related Databanks for Everyday Needs. *Nucleic Acids Res.* **2015**. <https://doi.org/10.1093/nar/gku1028>.
- (40) Humphrey, W.; Dalke, A.; Schulten, K. VMD: Visual Molecular Dynamics. *J. Mol. Graph.* **1996**. [https://doi.org/10.1016/0263-7855\(96\)00018-5](https://doi.org/10.1016/0263-7855(96)00018-5).
- (41) Micsonai, A.; Wien, F.; Kernya, L.; Lee, Y. H.; Goto, Y.; Réfrégiers, M.; Kardos, J. Accurate Secondary Structure Prediction and Fold Recognition for Circular Dichroism Spectroscopy. *Proc. Natl. Acad. Sci. U. S. A.* **2015**, *112* (24), E3095–E3103. <https://doi.org/10.1073/pnas.1500851112>.
- (42) Waite, J. H.; Qin, X. Polyphosphoprotein from the Adhesive Pads of *Mytilus Edulis*. *Biochemistry* **2001**. <https://doi.org/10.1021/bi002718x>.
- (43) Maier, G. P.; Rapp, M. V.; Waite, J. H.; Israelachvili, J. N.; Butler, A. Adaptive Synergy between Catechol and Lysine Promotes Wet Adhesion by Surface Salt Displacement. *Science (80-.)*. **2015**, *349* (6248), 628–632. <https://doi.org/10.1126/science.aab0556>.
- (44) Israelachvili, J. N. *Intermolecular and Surface Forces: Revised Third Edition*; Academic Press, 2011; Vol. 33. <https://doi.org/10.1073/pnas.0703993104>.
- (45) Sedō, J.; Saiz-Poseu, J.; Busqué, F.; Ruiz-Molina, D. Catechol-Based Biomimetic Functional Materials. *Adv. Mater.* **2013**, *25* (5), 653–701. <https://doi.org/10.1002/adma.201202343>.
- (46) Pinnaratip, R.; Bhuiyan, M. S. A.; Meyers, K.; Rajachar, R. M.; Lee, B. P. Multifunctional Biomedical Adhesives. *Adv. Healthc. Mater.* **2019**, *8* (11), 1–17. <https://doi.org/10.1002/adhm.201801568>.
- (47) Degen, G. D.; Stow, P. R.; Lewis, R. B.; Andresen Eguiluz, R. C.; Valois, E.; Kristiansen, K.; Butler, A.; Israelachvili, J. N. Impact of Molecular Architecture and

- Adsorption Density on Adhesion of Mussel-Inspired Surface Primers with Catechol-Cation Synergy. *J. Am. Chem. Soc.* **2019**. <https://doi.org/10.1021/jacs.9b04337>.
- (48) Ahn, B. K.; Lee, D. W.; Israelachvili, J. N.; Waite, J. H. Surface-Initiated Self-Healing of Polymers in Aqueous Media. *Nat. Mater.* **2014**, *13* (9), 867–872. <https://doi.org/10.1038/nmat4037>.
- (49) Ahn, B. K.; Das, S.; Linstadt, R.; Kaufman, Y.; Martinez-Rodriguez, N. R.; Mirshafian, R.; Kesselman, E.; Talmon, Y.; Lipshutz, B. H.; Israelachvili, J. N.; Waite, J. H. High-Performance Mussel-Inspired Adhesives of Reduced Complexity. *Nat. Commun.* **2015**, *6*, 1–7. <https://doi.org/10.1038/ncomms9663>.
- (50) Truex, N. L.; Nowick, J. S. Coassembly of Peptides Derived from β -Sheet Regions of β -Amyloid. *J. Am. Chem. Soc.* **2016**, *138* (42), 13891–13900. <https://doi.org/10.1021/jacs.6b06001>.
- (51) Chiti, F.; Stefani, M.; Taddei, N.; Ramponi, G.; Dobson, C. M. Rationalization of the Effects of Mutations on Peptide and Protein Aggregation Rates. *Nature* **2003**, *424* (6950), 805–808. <https://doi.org/10.1038/nature01891>.
- (52) Yu, J.; Wei, W.; Danner, E.; Israelachvili, J. N.; Waite, J. H. Effects of Interfacial Redox in Mussel Adhesive Protein Films on Mica. *Adv. Mater.* **2011**, *23* (20), 2362–2366. <https://doi.org/10.1002/adma.201003580>.
- (53) Miller, D. R.; Spahn, J. E.; Waite, J. H. The Staying Power of Adhesion-Associated Antioxidant Activity in *Mytilus Californianus*. *J. R. Soc. Interface* **2015**, *12* (111), 20150614. <https://doi.org/10.1098/rsif.2015.0614>.
- (54) Waite, J. H. Mussel Adhesion - Essential Footwork. *J. Exp. Biol.* **2017**, *220* (4), 517–530. <https://doi.org/10.1242/jeb.134056>.
- (55) Wei, W.; Yu, J.; Broomell, C.; Israelachvili, J. N.; Waite, J. H. Hydrophobic Enhancement of Dopa-Mediated Adhesion in a Mussel Foot Protein. *Journal of the American Chemical Society*. 2013, pp 377–383. <https://doi.org/10.1021/ja309590f>.

G. Supplemental figures for Chapter 2

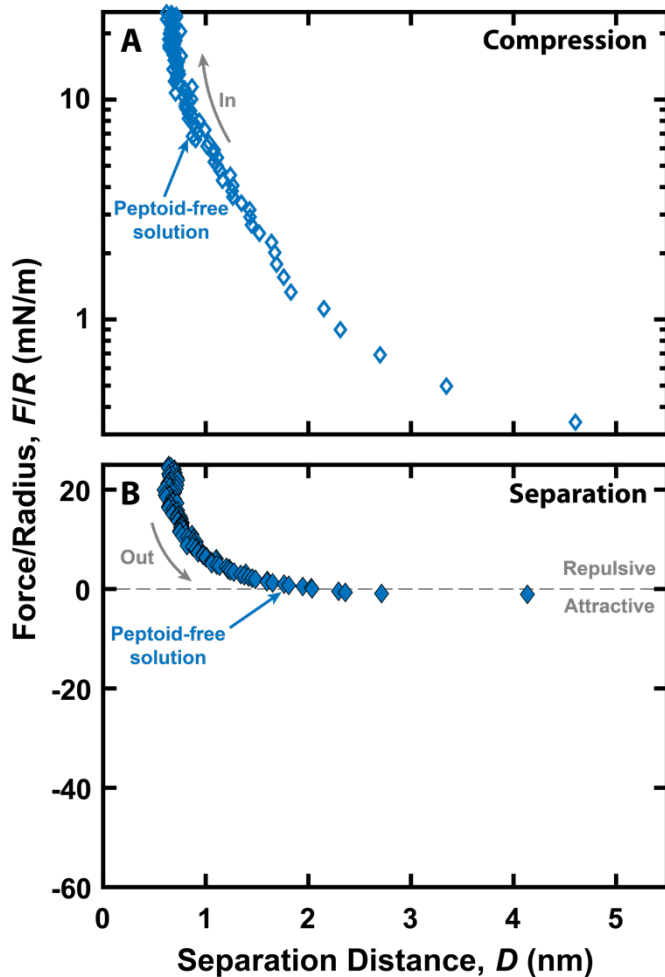


Figure 2.S1. Compression and separation force curves for bare mica. Interacts were measured in the presence of 250 mM KNO_3 , 100 mM acetic acid (pH=2.8).

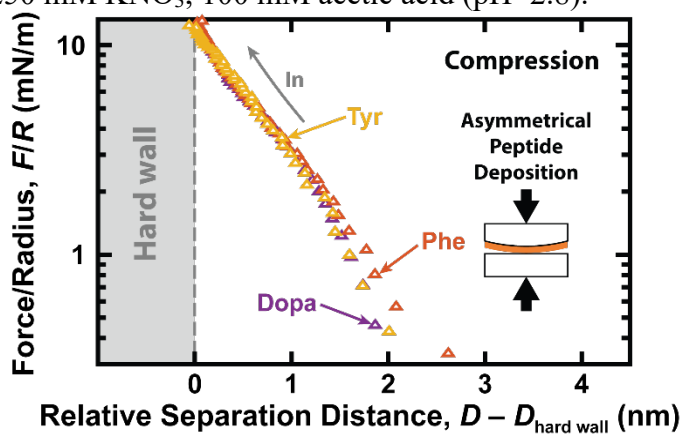


Figure 2.S2. Compression force vs. distance profiles of asymmetrically deposited peptides. adapted from Gebbie *et al.*

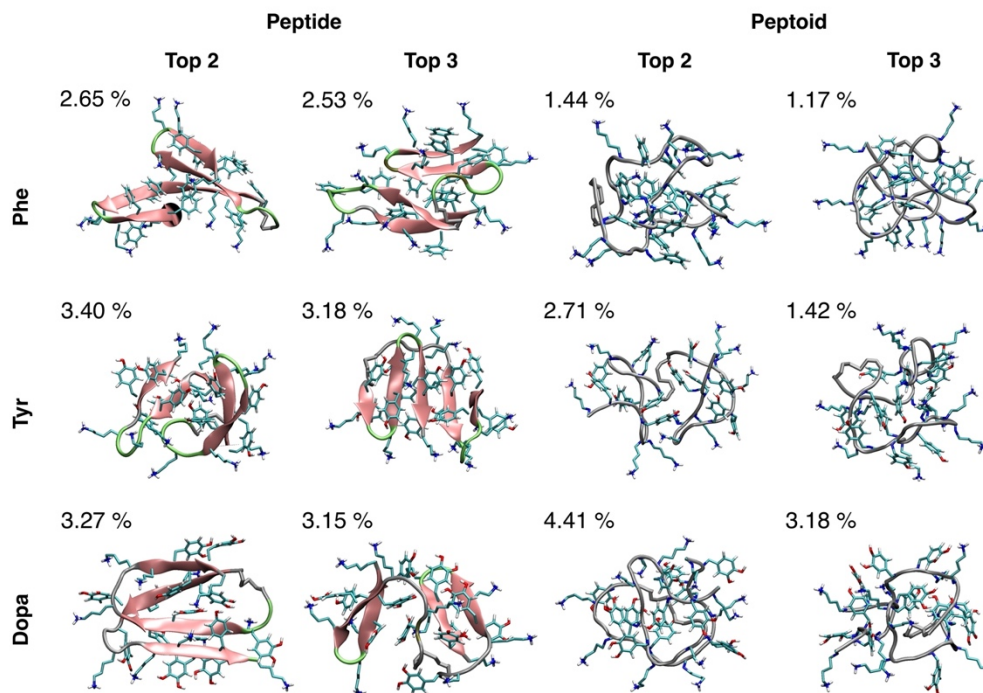


Figure 2.S3 Second and third most representative conformations of peptides and peptoids. Modelled in bulk water from clusters formed within a RMSD cutoff of 1.4 Å for the backbone atoms. The percentage of structures present in each cluster is shown in the *top left* (a total of 15,000 structures were analyzed). The secondary structure is shown (*pink*) with β -sheet formation indicated by wide arrows pointing from the N- to C-terminal. Atoms are color coded as N: *blue*; H: *white*; C: *cyan* O: *red*. Analyses were done for every 20 ps of the last 300 ns of simulation

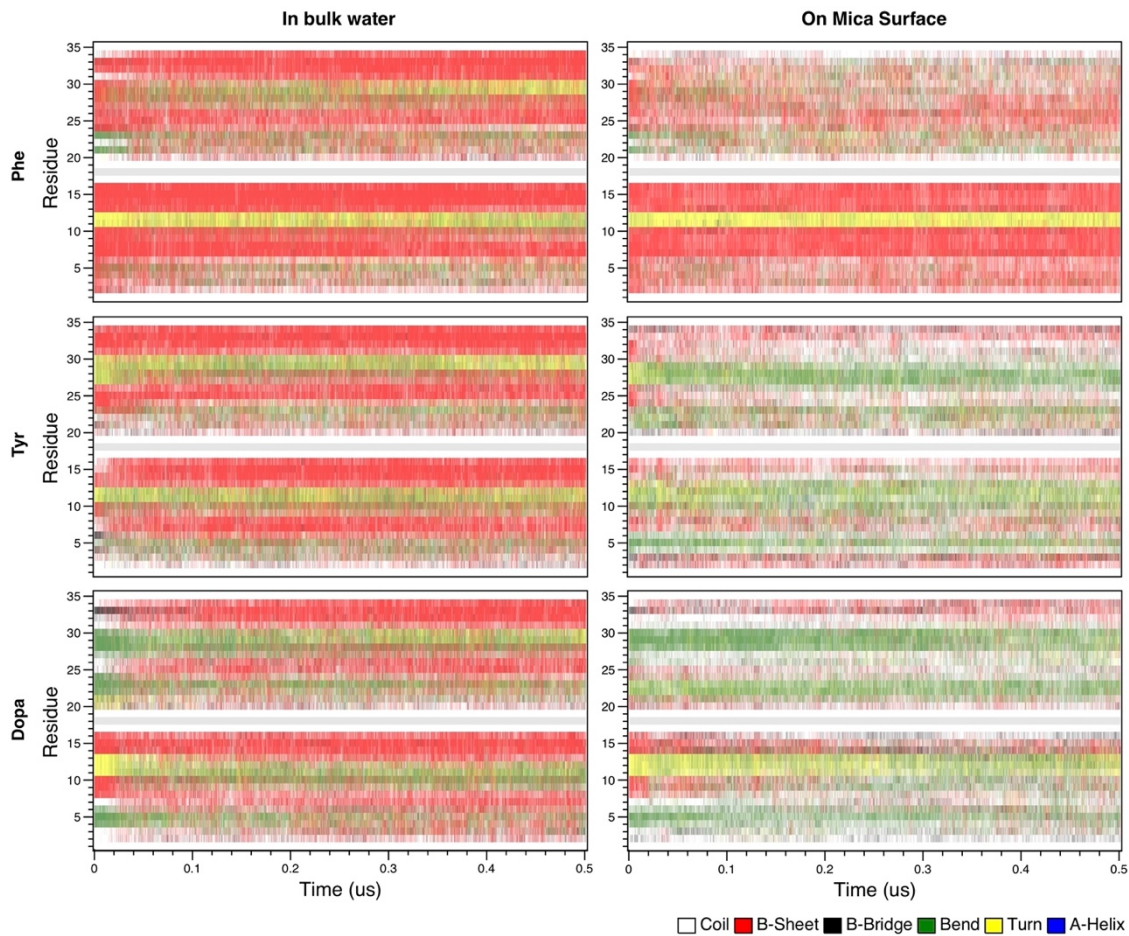


Figure 2.S4 Peptide secondary structure in the presence of mica over time. Secondary structure content adopted by each residue of the bioinspired peptides and peptoids in a bulk water and in the presence of mica surface. Analyses were done for every 20 ps of simulation

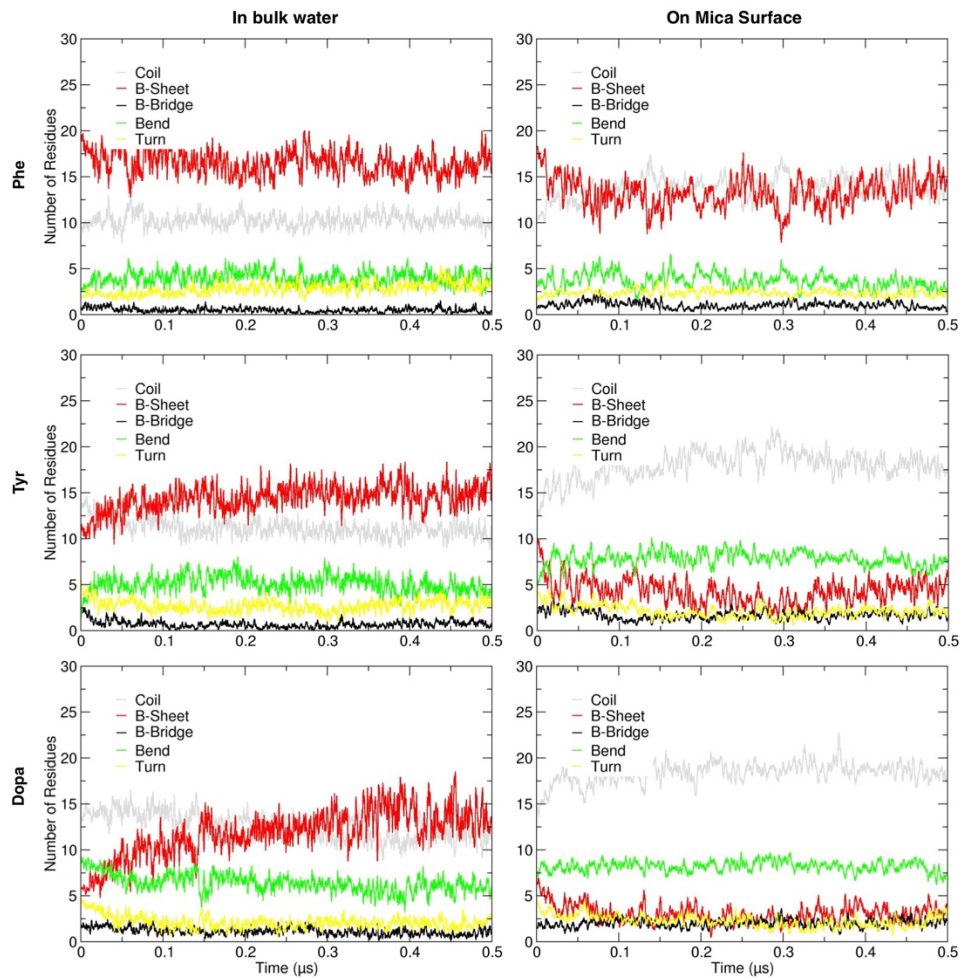


Figure 2.S5 Number of peptide residues adopting secondary structure in water and on mica. Average number of residues adopting a secondary structure along the simulation time. Analyses were done for every 20 ps of simulation and the average calculated by every 100 points.

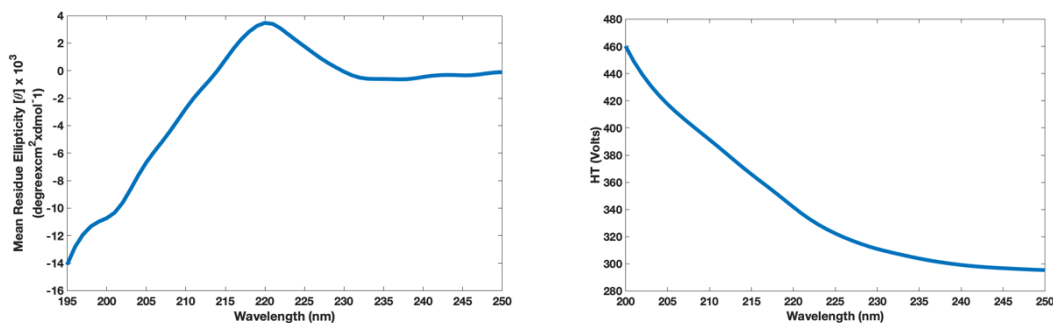


Figure 2.S6 Circular dichroism of Phe-peptide. (left) Circular dichroism spectrum of 20 μ M Phe-peptide in 10mM AcOH (pH = 2.8). (right) HT voltage profile of the Phe-peptide CD measurement.

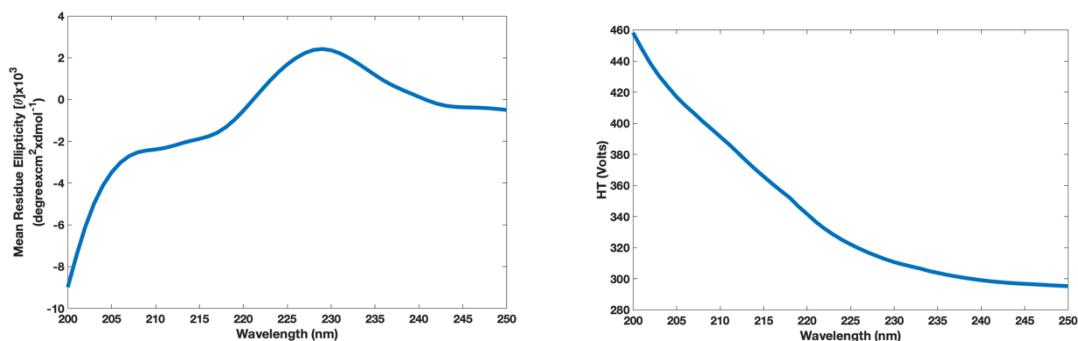


Figure 2.S7 Circular dichroism of Tyr-peptide. (left) Circular dichroism spectrum of 20 μ M Tyr-peptide in 10mM AcOH (pH = 2.8). (right) HT voltage profile of the Tyr-peptide CD measurement.

Table 2.S1 Secondary structure predictions of the Phe and Tyr peptides. Estimations were made using using the BeStSel.

	α -helix(%)	Parallel β -sheet (%)	Antiparallel β -sheet (%)	Turns (%)	Other (%)
Phe	0	0	26	21.1	52.8
Tyr	0	0	40.6	11.8	47.6

Table 2.S2 Number of clusters of likely conformation formed. The RMSD cutoff used was 1.4 Å for the backbone atoms and done excluding the tip residues. Analyses were done for every 20 ps of the last 300 ns of simulation, given a total number of structures of 15,000.

	Bulk Water	Mica
Peptide		
Phe	1773	486
Tyr	1446	485
Dopa	1526	328
Peptoid		
Phe	2594	589
Tyr	1764	525
Dopa	2594	557

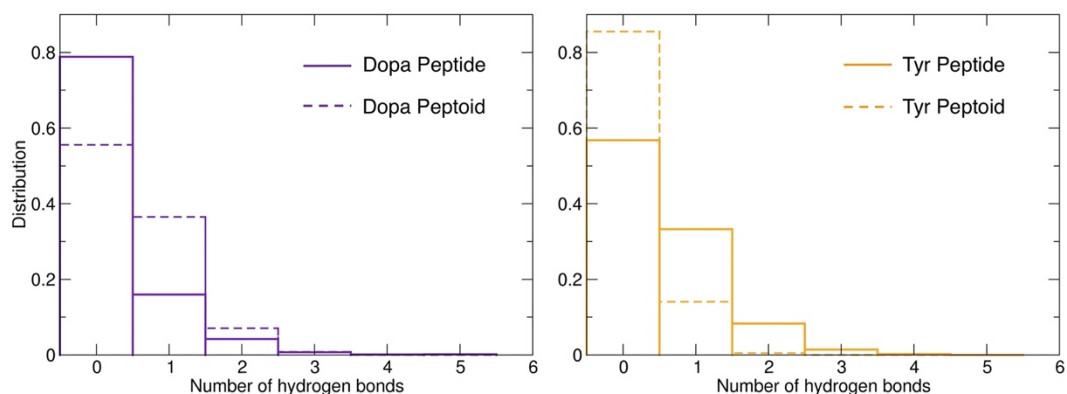


Figure 2.S8. Phenolic hydrogen bonding. Normalized histogram of the number of hydrogen bonds between the hydroxyl groups (from Dopa or Tyr residues) and mica. Hydrogen bonds cutoffs were: 3.5 Å for the distance Donor – Acceptor and 30° for the angle Hydrogen - Donor - Acceptor. Analyses were done for every 20 ps of the last 300 ns of simulation.

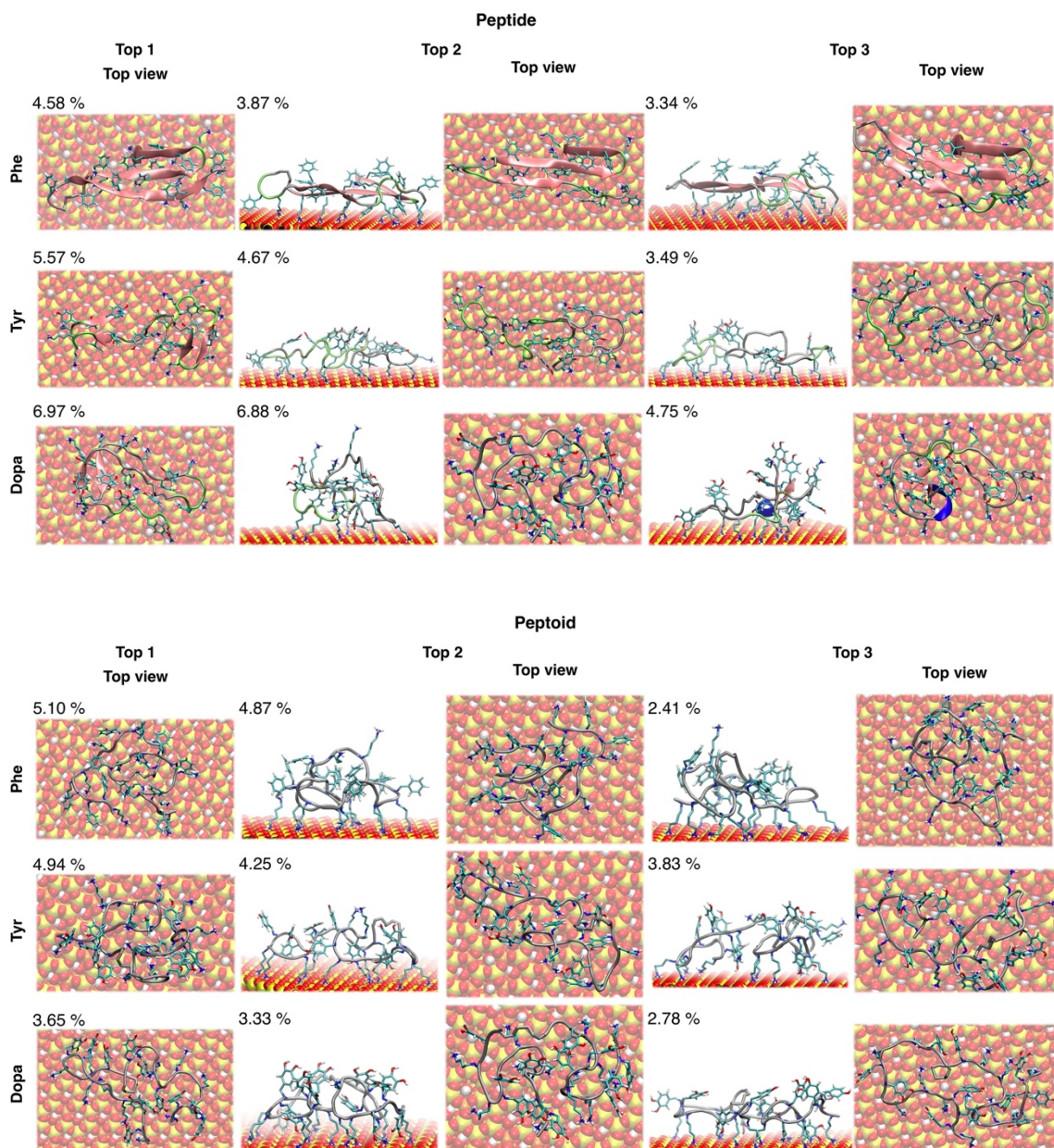


Figure 2.S9. Snapshots of the 3 most representative conformations on mica. From clusters formed within a RMSD cutoff of 1.4 Å for the backbone atoms. The percentage of structures present in each cluster is shown in the *top left* (a total of 15,000 structures were analyzed). The secondary structure is shown (*pink*) with β -sheet formation indicated by wide arrows pointing from the N- to C-terminal. Atoms are color coded as N: *blue*; H: *white*; C: *cyan*; Si: *yellow*; O: *red*; Al: *orange*. Analyses were done for every 20 ps of simulation of the last 300 ns of simulation.

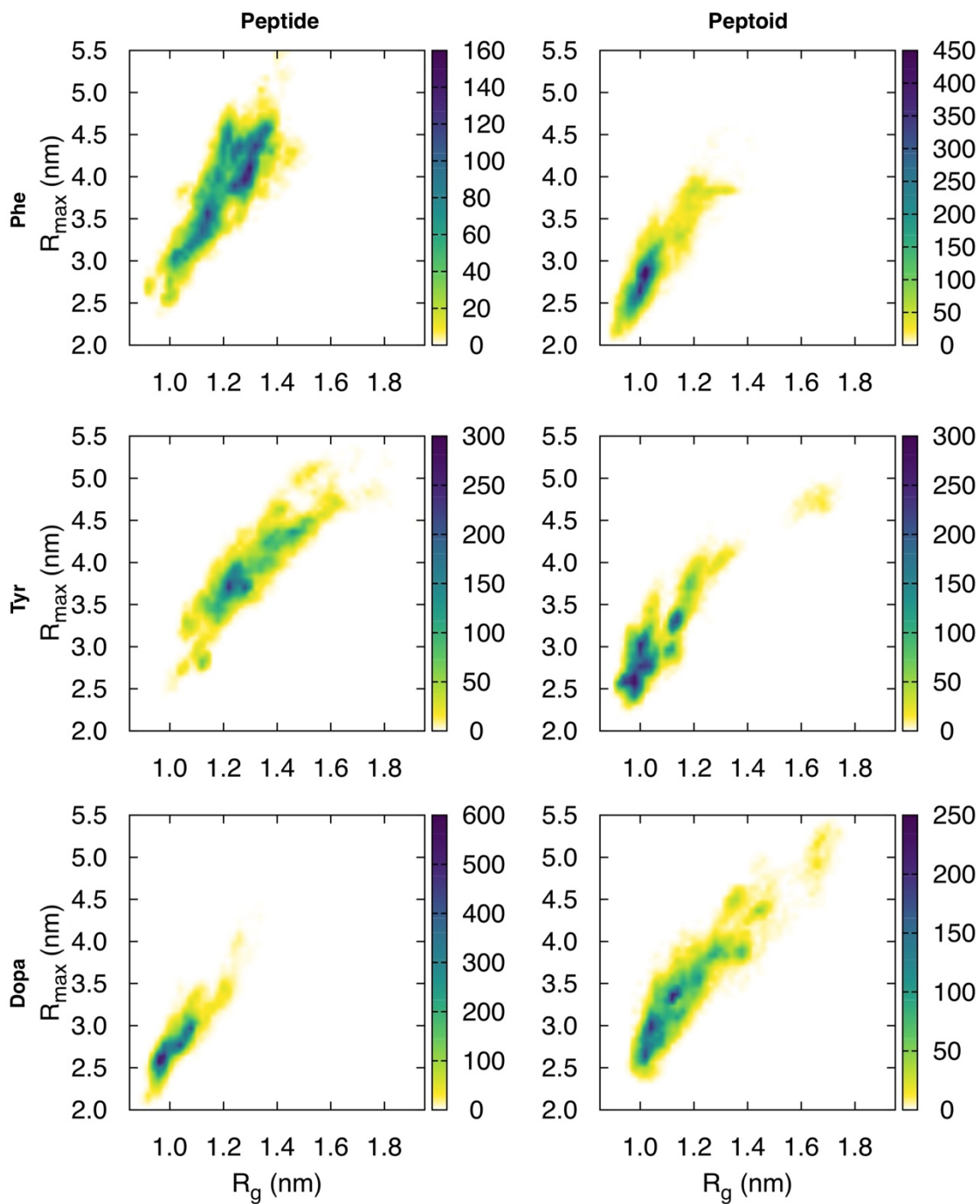


Figure 2.S10. 2D distribution of the radius of R_g vs. R_{max} . These were measured within any backbone atoms of the peptide/peptoid on mica surface. Analyses were done for every 20 ps of the last 300 ns.

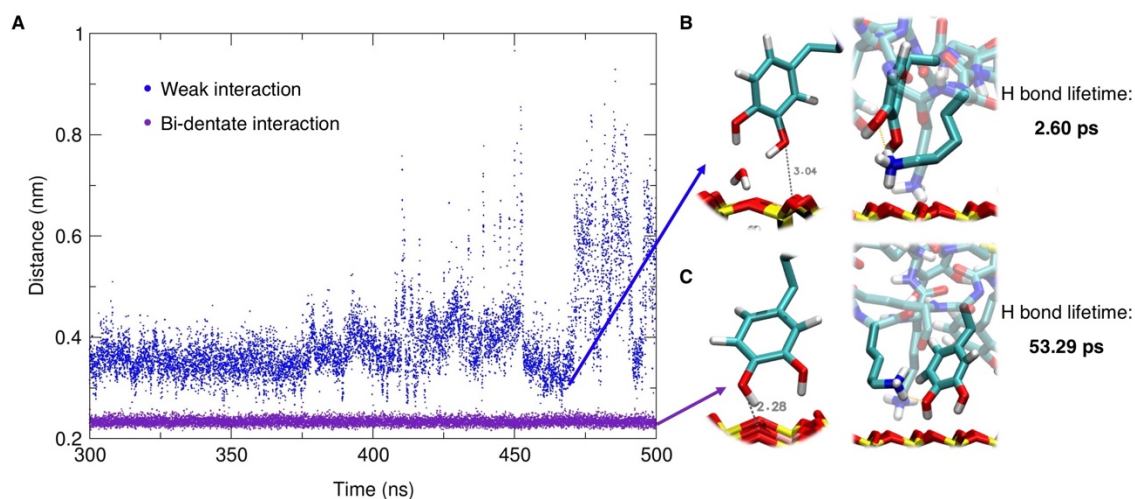


Figure 2.S11 Dopa interactions with mica. A) Minimum distance between any atom of the mica surface and the oxygen atoms of dopa residues. Results obtained by 500 ns of regular MD simulation of Dopa-containing peptide and peptoid. B) Cartoon representations of weak interactions between dopa residues and the mica surface. A minimum distance of 3.04 Å was observed in the case of an interaction between dopa and mica mediated by a water molecule (*left side cartoon*), higher distances can be due interactions mediated by Lys residues (*right side cartoon*). The hydrogen bond lifetime measured in this simulation was 2.6 ps. C) Cartoon representations of a bi-dentate interaction. In this case, the minimum distance between mica and an oxygen atom of dopa was 2.28 Å and the hydrogen bond lifetime was 53.29 ps.

Chapter 3

The glycine/histidine rich structural polypeptide of *Glycera* jaws

A. Abstract

Bloodworm jaws are a composite of protein, melanin, and both mineral and ionic copper. To date, nanomechanical tests have correlated the ionic copper and melanin with hardness and wear resistance but the function of protein has remained uncertain. Here, we characterize a Gly- and His-rich protein called multi-tasking protein (MTP) and, using a recombinant jaw protein, show that it performs five distinct functions critical for jaw assembly, namely *i*) recruiting 22 equivalents of Cu^{2+} , *ii*) mediating a liquid-liquid phase separation of the MTP-copper complex, *iii*) catalyzing the oxidation of 3, 4-dihydroxyphenylalanine (Dopa) to melanin, *iv*) templating the interfacial polymerization of melanin, and *v*) integrating melanin and itself into thin films and fibers. MTP achieves all these by assuming unprecedented roles as a building block, organizer, and fabricator – a processing feat of considerable relevance to the autonomous production of other polymer composites, blends, and/or networks.

B. Introduction

Synthetic hydrogels made from multiple polymer networks are renowned for their strength and toughness.^{1,2} The same is true for anhydrous double polymer networks, though fabrication of these remains challenging.³ As living organisms make both hydrogels and less hydrated varieties of tough polymer networks, a detailed study of formation strategies holds many potential insights. For example, vertebrate cartilage is a high-performance load-bearing hydrogel that is formed and maintained by isolated matrix-embedded cells known as chondrocytes that mediate simultaneous co-deposition and turnover of multiple polymer

networks.⁴ By contrast, in cell-free invertebrate cuticles such as squid beak, a chitinous hydrogel is deposited first by epidermal cells and then infiltrated with liquid-liquid phase-separated proteins that displace water and harden following oxidation.⁵ Here, we elucidate a third, previously unreported strategy in bloodworm jaws in which a suspension of metallo-protein droplets contributes catalytically and structurally to form a second melanin-like network in situ.

The bloodworm *Glycera dibranchiata* (Ehlers, 1868) is a marine polychaete (phylum Annelida) that burrows through intertidal benthic mud to a depth of several meters. The proboscis of each worm is equipped with four black jaws (Figure 3.1, a,b) that grasp and inject venom into other creatures during hunting and combat. The major structural components of *Glycera* jaws are protein (~50% w/w), ionic and mineralized copper (up to 10%) and melanin (~40% w/w).^{6,7} The presence of melanin is not unusual, as melanin is extensively used in biology as a pigment. Jaw melanin, however, is unique in existing as a contiguous material that is ~2 mm in length thereby greatly exceeding the micrometer length scale typically associated with dispersions of melanin pigment found in *Sepia* ink or melanosomes.⁸

Melanin has many desirable properties,⁹ but given that *in vitro* formation typically leads to dispersions of small (~100nm diameter) granules,⁸ applications of melanin in synthetic materials remain limited. The melanin and copper in *Glycera* jaws are correlated with impressive wear resistance,¹⁰ and a deeper understanding of the mechanisms of their formation and function could lead to expanded use of melanin in high-performance materials. Although previous work has shown that the protein composition of whole jaws is dominated by glycine (Gly) (~50 mol%) and histidine (His) (~30 mol%),⁶ the function of these Gly-His rich sequences is currently unknown.

Here, we identify and characterize properties of the primary structural protein in bloodworm jaws, hereafter named Multi-tasking Protein (MTP). *Glycera* MTP is a multifunctional molecule with the ability to chelate copper, phase-separate, catalyze the polymerization of L-3,4 dihydroxyphenylalanine (Dopa) to melanin, and template the synthesis of a macroscopic 2D melanin-protein composite film, all notwithstanding its sequence simplicity. The concerted activities of MTP in the construction of *Glycera* jaw architecture present a compelling opportunity to rethink the design of processing technologies needed for high performance and sustainable composite and blended polymeric materials.

C. Materials & Methods

i. Amino Acid Analysis

Samples for amino acid analysis were hydrolyzed with 6M HCl, 1% phenol, in vacuo at 110°C overnight. HCl and phenol were removed under vacuum with a Savant SpeedVac SC110. After washing the residues with water and methanol, the samples were reconstituted in 0.2N HCl. Amino acid compositions were determined on a Hitachi L8900 amino acid analyzer system.

ii. Transcriptome generation and assembly

Live *Glycera dibranchiata* specimens were purchased from the Bloodworm Depot (Whitefield, ME) and the jaws were dissected immediately. The connective tissue and musculature on the outside of the jaw was carefully removed under a dissecting microscope. Tissue inside the base of the jaw, however, was undisturbed. Samples were stored in RNeasyTM (Invitrogen) and flash frozen in liquid nitrogen. Homogenization of the samples was performed under liquid nitrogen with a mortar and pestle, after which RNA was purified using a Purelink RNA Isolation kit (ThermoFisher Scientific, Waltham, MA) following the

manufacturers instructions. Four jaws from the same worm were used for RNA isolation. Total RNA samples were sent to myGenomics® (Atlanta, GA) and paired end sequenced (2 x 150 bp) on an Illumina Hiseq™ 2500 platform (Illumina, San Diego, CA). The raw sequencing data was analyzed using the Galaxy bioinformatics program.¹¹ We used the read processing tool Trimmomatic to remove adapter sequences and low-quality reads. The trimmed reads were then assembled into mRNA isotigs using the Trinity software package¹² In order to estimate the transcription level of each isotig we used the software RSEM¹³ to correlate trimmed reads with assembled transcripts. To identify candidates for the jaw proteins of *Glycera* we searched for sequences based on three criteria: 1) the presence of a signal peptide, 2) the presence of a stop codon, and 3) glycine and histidine contents of greater than 30 and 20%, respectively.

iii. Polymerase chain reaction validation and molecular cloning

We verified the presence of the *Glycera* jaw protein using polymerase chain reaction (PCR). The cDNA library was prepared with a SuperScript III RT-PCT (Invitrogen) kit following the manufacturer's instructions. The primers used were: (5') CAT ATG GTG CAA GTA AGA AGT GGC GGC and (3') AAG CTT GTG TCT TCG GTG TAG GTG ACA TCC (note: HindIII and NdeI restriction sites were added for further subcloning). The PCR products were cloned into pCR4 vectors using a TOPO-TA cloning kit (Invitrogen, Carlsbad, CA), transformed into chemically competent TOP10 *Escherichia coli* (Invitrogen), and grown on Luria-Bertani (LB) agar plates with kanamycin. Positive clones were grown over night in LB media and the plasmid DNA was purified using a GeneJET Plasmid Miniprep Kit (ThermoFisher) following the manufacturers instructions. The plasmids were sequenced by

Sanger sequencing (Genewiz, Newbury Park, CA). The constructs were subcloned into the pET-26b(+) vector (Novagen) and transformed into TOP10 cells for maintenance.

iv. Recombinant expression and purification

We expressed the protein by freshly transforming the pET-26b(+) construct in BL21-(DE3)pLysS (Promega, Madison, WI) cells according to the manufacturer's instructions. Cells were screened by growth on LB agar with kanamycin and chloramphenicol and colonies were maintained at 4°C. Selected colonies were grown overnight in 10mL of LB media augmented with 0.1% glucose (to further reduce basal expression), kanamycin, and chloramphenicol at 37°C. Saturated cultures were transferred into 1 liter of Terrific Broth supplemented with 0.1% glucose, grown at 30°C to an optical density of ~0.6 at 600 nm. Expression was induced by the addition of isopropyl 1-thio-β-D-galactopyranoside to a final concentration of 1mM. Cells were expressed for ~12 hours, after which they were pelleted by centrifugation (10 minutes, 5000 x g), washed with buffer (20mM Tris, 100mM NaCl, 0.1mM EDTA, pH=7.4) and pelleted by centrifugation (10 minutes, 5000 x g). Cell pellets were stored at -80°C until use. Bacteria were resuspended in lysis buffer (20mM Tris, 100mM NaCl, 7M Urea, pH=7.4) with 100mM imidazole, and lysed via sonication on ice (5x30seconds, 7mW). The cell lysate was centrifuged at 10,000 x g. The supernatant was applied to a HisTrap FF immobilized metal affinity column (IMAC) charged with Ni(SO₄) and equilibrated with lysis buffer. Unbound protein was removed by successive washes of lysis buffer with 100mM and 300mM imidazole. Bound protein was eluted by washing with 500mM imidazole in lysis buffer. Fractions with pure protein were identified by SDS-PAGE, acidified by the addition of 0.1% trifluoroacetic acid, and desalted by reverse phase C8 HPLC. Protein was concentrated with lyophilization, after which it was reconstituted in Milli-Q water and kept at -80°C. We

performed quantitative amino acid analysis to confirm the protein identity as well as estimate protein concentration.

v. Isothermal titration calorimetry

Isothermal titration calorimetry (ITC) was used (NanoITC, TA Instruments, New Castle, DE) to measure the thermodynamics of copper binding to the *Glycera* jaw protein. In general, the sample cell was filled with 950 μL of 10 μM *Glycera* jaw protein freshly dissolved in sample buffer (10 mM Tris, pH=7.4) at a final concentration of 10 μM . A solution of 3 mM CuSO_4 in 10 mM Tris (pH=7.4) was loaded into the syringe. Titrations were carried out as a sequence of 40 injections of 4.86 μL , with the stirring speed set at 250 rpm and the temperature set to 20°C. Control titrations were carried out to account for buffer mismatch (titrating copper solution into buffer only) and heat of dilution (titrating buffer into the protein solution). The final data was fit using the independent model provided in the NanoAnalyze software (version 3.3) and an independent model.

vi. Continuous wave electron paramagnetic resonance

Continuous wave (CW) electron paramagnetic resonance (EPR) was performed on freshly prepared samples of 5 μM MTP, 50 μM CuSO_4 in 50 mM Tris buffer (pH = 7.4). A volume of 0.5 mL was added to a 4 mm inner diameter quartz EPR tube (Wilmad). A Bruker EMXplus EPR spectrometer operating at 9.6 GHz and equipped with a Bruker ER 4119HS-LC High Sensitivity Probehead was used to collect the X-band EPR spectrum. Spectra were acquired at 140K using 2.0 mW microwave power, 6.0 G modulation amplitude, 3000G sweep width, and averaging 32 scans.

vii. Cryogenic TEM

Samples of 5 μM MTP with and without 50 μM CuSO_4 were prepared in 100 mM Tris buffer (pH = 7.4). Typically, 2 μL of sample was pipetted onto a copper grid coated with lacey carbon, blotted with filter paper (Vitrobot Mark IV, FEI), and then quickly submerged in liquid ethane. Samples were loaded with a Gatan cryo transfer holder maintained at -180°C . Imaging was performed with an FEI Tecnai G2 20 transmission electron microscope (TEM) operated at 200kV.

viii. Catechol oxidase activity assay

A 3-methyl-2-benzothiazolinone hydrazone hydrochloride (MBTH)-based assay was used to measure catechol oxidase activity.¹⁴ The buffer for the reaction contained 100mM Tris, 4% DMF (v/v), and 6 mM MBTH. MTP was used at a final concentration of 5 μM and, when indicated, CuSO_4 was added to a final concentration of 50 μM . L-Dopa was the substrate and added at concentrations of 0.01, 0.1, 0.2, 0.5, 1, and 2mM. The final reaction volume was 250 μL . Reactions were carried out at room temperature using a 96-well well plate (Greiner) and each done in triplicate. The reaction was monitored at 505nm every minute with a SpectraMax microplate reader (Molecular Devices). We used the molar extinction coefficient of the Dopachrome-MBTH adduct ($28,900\text{ M}^{-1}\text{ cm}^{-1}$)¹⁵ to report reaction rates as change in concentration with time. The data were fit to the Michaelis-Menten model.

ix. Mass Spectrometry

Matrix-assisted laser desorption/ionization time-of-flight mass spectrometry (MALDI-TOF-MS) was used to assess HPLC fraction purity and was performed on a microflexTM LRF (Bruker). Generally, 2 μL of sample with 8 μL of saturated α -cyano-3-hydroxycinnamic

acid in aqueous 50% acetonitrile and 0.1% TFA were mixed, spotted on a ground steel MALDI target plate, and dried under vacuum.

x. Film growth and fiber drawing

Films were grown by preparing a 1 mL solution with 4.5 μ M protein (0.1mg/mL), 45 μ M CuSO₄, and 500 μ M L-Dopa in 100mM Tris buffer (pH=7.4). Sheet formation was not observed at pH=6 or below. We spread the solution on a clean microscope slide and generally after ~30 minutes the film had formed, identified under a dissecting microscope after agitation of the surface with a clean syringe needle. Samples for SEM and AFM were prepared by dipping a clean silicon coupon on the top of a solution with a freshly prepared film after 30 minutes of reaction. These samples were allowed to dry, washed extensively with water, and dried again under vacuum.

Fibers were prepared from freshly prepared films as described for sheet preparation. After 30 minutes of formation, fibers were drawn by touching a clean metal dissecting probe into the freshly formed film and pulling the probe slowly away from the solution. A slow rate is necessary to maintain fiber integrity. Fibers were stored in a desiccating chamber until tensile testing. Fibers kept in a humidity chamber would partially splay out and regain some sheet character.

xi. Alkaline peroxide degradation and melanin quantification

A spectrophotometric assay of the solubilization of melanin by an alkaline peroxide solution was used to quantify the melanin content of the interfacial product. In the presence of H₂O₂ at alkaline pH at high temperature melanin will degrade into pyrrole-based chromophores.¹⁶⁻¹⁸ The absorption of these products at 560 nm has a linear relation to the amount of melanin degraded.⁷

Aqueous suspensions of synthetic melanin at concentrations of 0.1, 0.25, 0.5, 0.75, and 1 mg/mL were used to generate a standard curve. Melanin was dissolved by the addition of one part 10N NaOH and 2 parts 30% H₂O₂ to 37 parts sample suspended in water followed by incubation at 70°C for 30 minutes. The interfacial films were dissolved in an identical manner to afford a solution at a concentration of 4 mg/mL. The absorbance of each sample at 560 nm were then measured. The best fit line for the melanin standard was forced through zero and gave an $R^2 = 0.9983$.

xii. Scanning Electron Microscopy

Interfacial films were polymerized as described above. The interfacial sheet was transferred to a small silicon coupon by bringing the coupon in contact with the surface of the reaction for 10 seconds. After drying under vacuum, the sample was gently washed 3 times 1 mL of milli-Q water. After attachment to an imaging stub, the sample was sputter-coated with a thin layer of gold for 100s using an Anatech USA Hummer 6.2 coater. A Fei Nano Nova 640 FEG scanning electron microscope (SEM) was used to observe the samples.

xiii. Interfacial rheometry

Interfacial rheology was measured using a double walled ring (DWR) metal geometry attached to a stress-controlled rheometer (AR-G2, TA Instruments). Samples were loaded into a stepped annular trough made from Delrin, with radii as specified previously¹⁹ and a trough depth of 2mm. To probe the evolution of interfacial viscoelasticity, storage (G') and loss (G'') moduli were recorded in response to an inputted small amplitude oscillatory strain with amplitude 1% and frequency 2 Hz. Based on geometric and material parameters, the Boussinesq number was at least $O(10^2)$ which indicates that measurements were appropriately probing interface-dominated behavior. To minimize time between loading the sample and

starting the measurement, the location of the liquid-air interface was first determined for a trough filled with water by carefully adjusting the geometry height until full capillary contact was observed. For samples loaded afterwards, the geometry was immediately moved to the known position of the interface.

xiv. Atomic Force Microscopy

Samples of interfacial films were allowed to form on glass microscope slides for 30 minutes. The films were transferred by contacting a mica sheet with the surface for several seconds to allow the films to adsorb. The films were then allowed to dry and washed with milliQ water. These samples were then imaged using a MFP-3D Bio atomic force microscope (AFM) (Asylum Research, Goleta, CA).

xv. Tensile testing

The ends of dry fibers were clamped with stainless steel grips. We estimated cross sectional area by analyzing diameters of microscope images of each fiber and assuming a cylindrical geometry. The samples were loaded securely between grips were tested using a Nanobionix tensile tester (MTS). The samples were tested at ambient humidity and temperature. Stress-strain curves were taken at a strain rate of 0.1 min^{-1} and each sample was loaded to failure.

C. Results

i. *Glycera* jaws, transcriptomics, and protein sequence

The everted proboscis of a *Glycera dibranchiata* worm in Figure 1a highlights its four black jaws. The jaws are approximately 2mm in length (Figure 3.1a,b) and have impressive mechanical properties that do not depend on mineralization,¹⁰ *Glycera* jaws are highly sclerotized with protein, copper ions/mineral, and melanin distributed throughout the

hierarchical architecture.^{6,7} The protein component has a composition dominated by 2 amino acids: Gly (>50mol%) and His (>30mol%) (Figure 3.1c). Undermined by the high degree of cross-linking in the jaw, protein extractions have consistently resulted in low yields though sufficient amounts of a 30 kDa protein were obtained to prove that its amino acid composition matched that of the jaw.²⁰ From that point on, we have relied on state of the art transcriptomic methods to investigate this peculiar protein.

A transcriptome generated from the jaw pulp of *G. dibranchiata*, (the soft tissue at the immediate base of the jaw and presumably the site of MTP synthesis) provided ~24,000 transcripts, the most highly represented being cytoskeletal proteins such as actin and myosin.

We identified assembled candidate sequences by searching the transcriptome for transcripts rich in both glycine and histidine. The most compelling candidate sequence is shown in Figure 1d and was chosen because it was a fully assembled transcript, containing a start codon, signal peptide, and stop codon. The predicted protein sequence composition also matched the amino acid composition of jaws (Figure 3.1c), and because it showed a similar composition and molecular weight of ~ 30kDa (as determined by SDS-PAGE) to the protein purified from *G. dibranchiata* jaws in previous work.²⁰ We validated the sequence by traditional PCR methods, cloning it from fresh cDNA generated from the jaw pulp with primers outside the coding sequence. The PCR product was sequenced by Sanger methods and successfully cloned expressed in *E. coli*.

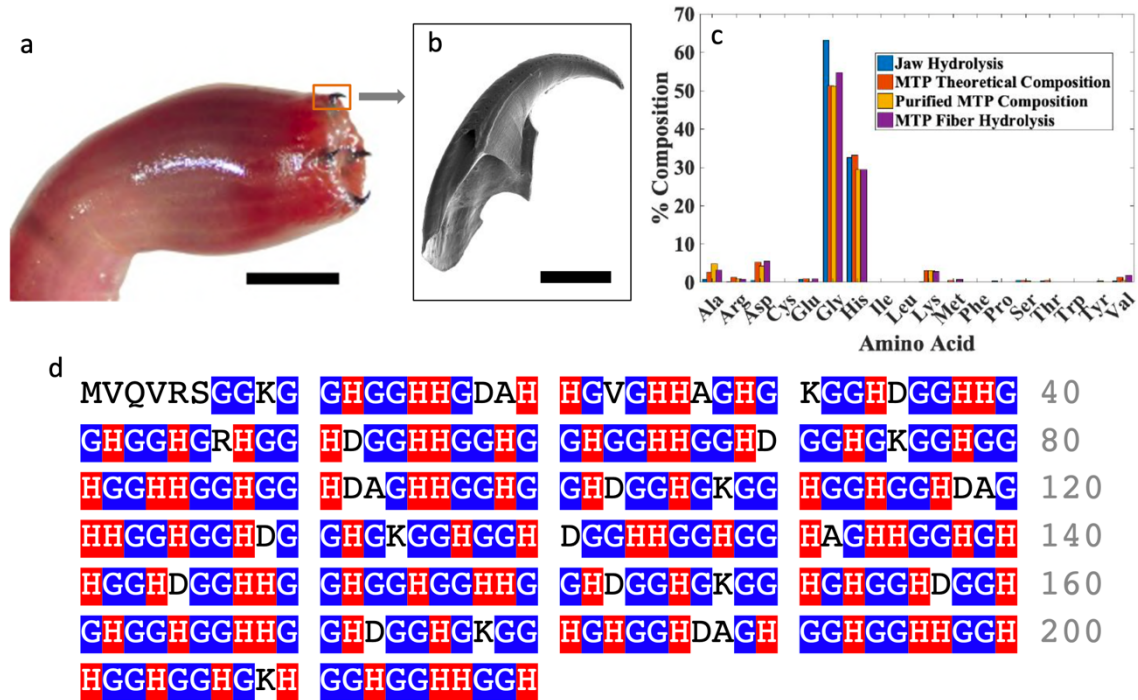


Figure 3.1. Structure and protein analysis of *Glycera* jaw. a) Image of the everted proboscis of *Glycera dibranchia* with its four jaws exposed. Scale bar represents 5 cm. b) Scanning electron microscope image of a *Glycera* jaw. Scale bar corresponds to 0.5mm. c) Amino acid composition of *Glycera* jaws (blue), theoretical amino acid composition of MTP (orange), experimental amino acid composition of purified recombinant MTP (yellow), and amino acid composition of the solid interfacial film formed when MTP, Cu^{2+} , and Dopa are reacted together (purple). d) Sequence of MTP with glycine and histidine residues highlighted in blue and red, respectively, for emphasis.

Consistent with acid hydrolyzed jaw, MTP sequence is dominated by glycine and histidine (over 80%). There are no instances of more than two Gly (G) or His (H) residues in a row, resulting in a sequence made up almost entirely of HGGH, GGH, or HGG repeats, depending on the point of reference. Typical BLAST searches of UniProtKB/Swiss-Prot databases returned no homologous sequences. Not surprisingly, the prevalence of Gly/His in MP does show similarities to that of another polychaete *Nereis virens* jaw protein-1 (Nvjp-1),^{21,22} however, *Glycera* MTP lacks the abundant aromatic residues of Nvjp-1. The unusually high Gly content of MTP suggests flexibility and intrinsic disorder. High Gly content is found in a number of other structural proteins such as plant cell wall glycine-rich proteins (60-

70%),²³ spider silk fibroin (47.3%),²⁴ collagen (~33%), and elastin (~30%).²⁵ Moreover, MTP adds to a growing number of Gly and His rich structural proteins found in invertebrates including polychaete (*Glycera/Nereis*) jaws, squid beaks, *Hydra* nematocyst spines, insect mandibles, and spider fangs are all robust structures both with and without added metal ions.²⁶ The ~40 mol% His content enables a dramatic pH-triggered shift in the total protein charge, ranging from ~90% charged at one pH unit below the pK_a of His (~6.5) and 90% uncharged at one pH unit above the pK_a. Given that proteins are stored at pH 5-6 before secretion and seawater pH is 8.2, the His-dependent pH trigger is a potent one.³¹

ii. MTP structure and copper binding

The influence of pH and copper on MTP structure is shown in Figures 3.S1 and 3.S2. The CD spectrum at pH 5.0 exhibits an ellipticity minimum at 201nm, and maxima at 195 and 220nm. Upon raising the pH to 7.4 the minimum is shifted to 195, and the intensity of the maximum at 220nm increases. The addition of copper at pH 7.4 does not result in an appreciable change in the CD spectrum. Although the CD spectrum does change with increasing pH, deconvolution of the spectra with the program BeStSel²⁷ estimates that all conditions represent a significant amount of random coil (>40%) and β -sheet content (>40%) hence the predicted flexibility is confirmed by CD measurements.

Copper binding ability of the MTP was investigated because the jaw contains significant quantities of copper (up to 10% by weight) that is both ionic and mineral. Isothermal titration calorimetry (ITC) confirmed that MTP has impressive copper binding capacity (Figure 3.2a). The data were fit to an independent model (NanoAnalyze software), which considers each binding site to be equivalent and independent, we found an apparent

equilibrium constant of $K_{ITC} = 7.1 \times 10^5$ M and a binding capacity of $N=22$ equivalents of copper. A white precipitate formed upon addition of excess copper ions.

ITC experiments support the notion that His contributes to copper binding. Under our experimental conditions, the apparent equilibrium constant of MTP with copper compares well with that of ceruloplasmin.²⁸ but is lower than that of other copper transport proteins, such as serum albumins. The more impressive aspect is the copper binding capacity ($N=22$). When normalizing this value to protein MW, MTP binds 1 Cu^{2+} /kDa whereas ceruloplasmin binds 0.04 Cu^{2+} /kDa (assuming $N=9$ Cu^{2+} and $\text{MW}=121$ kDa) and binding stoichiometry for bovine serum albumin is 0.08 Cu^{2+} /kDa (assuming $N = 5$ Cu^{2+} and $\text{MW}=66$ kDa).²⁹

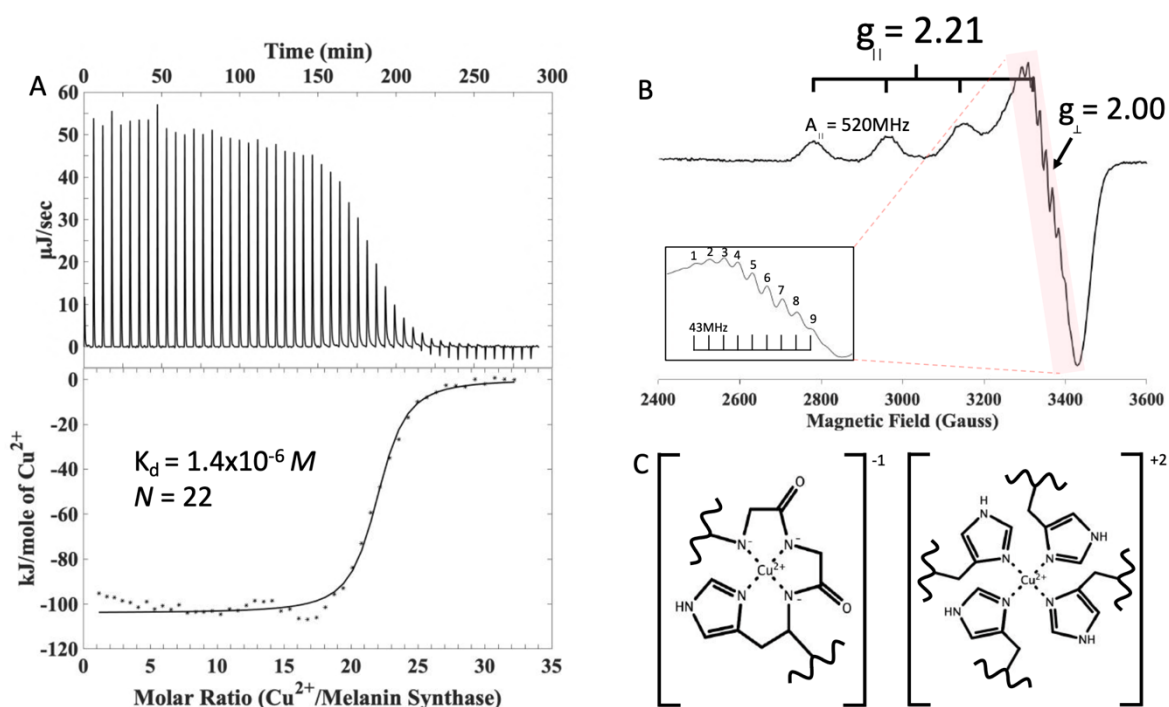


Figure 3.2. *In vitro* characterization of copper binding to MTP. A) ITC thermogram for the titration of 3.3mM CuSO_4 into 0.03mM MTP at pH 7.4. Top panel: raw heat trace. Bottom panel: the integrated peaks (*) and the solid line is the nonlinear least squares fit to a multiple binding site model. B) X-band EPR spectrum of frozen 0.1mM MTP in 100mM Tris and 1mM CuSO_4 . The part highlighted in red is shown in the inset and displays the nine line superhyperfine splitting. C) Possible binding structures of copper to protein either that includes backbone amide bonding (left) or only via histidine side chains (right).

iii. Structure of the Cu-MTP complex

To investigate the structure of MP bound to copper, we performed low temperature X-band continuous wave (CW) electron paramagnetic resonance (EPR) spectroscopy of MP-Cu²⁺ complex in Tris buffer at pH 7.4. The spectrum reveals three clear low field parallel lines with $g_{\parallel} = 2.21$ and $A_{\parallel} = 520$ MHz, with the fourth obscured by the perpendicular portion (Figure 3.2b). Simulation of the perpendicular region indicates a g value of 2.00. The low field edge of the perpendicular region also shows at least nine well-resolved super-hyperfine lines separated by 43MHz (Figure 3.2b, inset).

Although the copper binding properties are entirely predictable from the high histidine content, the coordination mode is not. The ‘GGH’ motifs that make up the vast majority of the protein sequence are reminiscent of Gly/His model peptides that have been studied to mimic the *Amino Terminal Copper and Nickel* (ATCUN) motif³⁰ as well as those synthesized to mimic the active site of Cu, Zn superoxide dismutase (SOD).³¹⁻³³ These peptides generally form square-planar complexes involving one or more Cu(II)-amide bonds. The nine line superhyperfine EPR splitting pattern and our EPR parameters of $g_{\parallel} = 2.21$ and $A_{\parallel} = 520$ MHz are consistent with coupling to four equatorial nitrogens.^{34,35} However, it is unclear how many of these nitrogens are from the backbone or side-chain imidazole groups. Figure 3.2c posits copper complex geometries most consistent with these data.

iv. MTP coacervation

The Cu²⁺-dependent self-assembly of MTP was demonstrated by Cryo-TEM. In the presence of Cu²⁺ ions, MTP readily formed spherical droplets (Figure 3.3 a,b - red arrows). These condensate droplets appeared to have no internal structure and were polydisperse, with diameters ranging from 50 nm to greater than 400 nm. The phase separated material readily

adsorbed to the lacy carbon support of the grids. Figure 3.3b shows two droplets fusing, indicating the fluid-like behavior of the condensed phase. We found no evidence of phase separation in the absence of copper (Figure 3.S3).

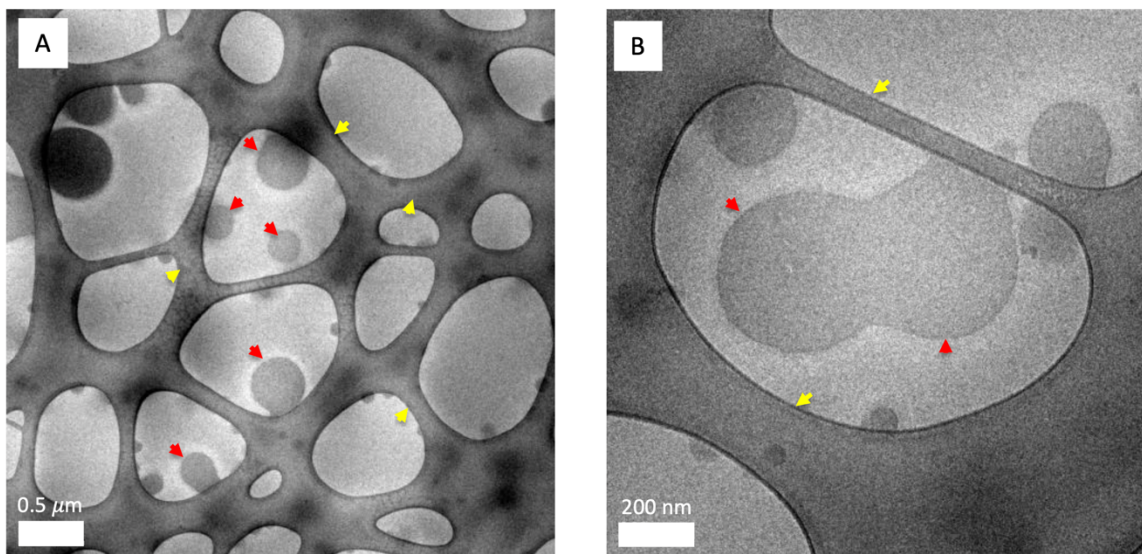


Figure 3.3. Copper induced coacervate phase transition. a) Cryo-TEM image of phase separated droplets (red arrows) that form when 50 μ M CuSO₄ is added to 5 μ M MTP in 50 mM Tris buffer (pH = 7.4) supported on a lacy carbon support (the contiguous phase indicated with yellow arrows). b) Cryo-TEM image showing the fusion of two coacervate droplets (red arrows) indicating their fluid behavior. Again, the lacy carbon support is indicated with yellow arrows.

The copper-induced phase separation was unexpected, even though intrinsically disordered³⁶ and low complexity³⁷ proteins are often correlated with phase separation. Reversible metal-coordination induced coacervation is a known phenomenon but somewhat rare.³⁸ That Cu-MTP apparently forms a condensed liquid phase is indicated by droplet coalescence (Fig. 3.3b) and probably driven by a mechanism that depends on Cu-binding dependent charging: the theoretic isoelectric point of MTP is \sim 7.4, thus is neutral at the reaction pH. However, after binding to Cu²⁺ it will either gain a net positive charge if complexation is solely through imidazole groups, maintain neutrality if 2 amide nitrogens form coordinate bonds, or become net negatively charged if three amide nitrogens are

recruited for the complexation (Figure 3.2c). Thus, the protein will have a combination of both uncharged and charged regions capable of facilitating separation of a dense protein-rich liquid phase. Based on the potential interfacial activity of the copper-bound protein, hydrophobic interactions exposed by His complexation with copper may contribute an additional driving force for phase separation. The droplet affinity for the lacy carbon support (Figure 3.3a,b) is consistent with the low interfacial tension of coacervate phase.³⁹

v. Dopa oxidation

The presence of melanin and copper in *Glycera* jaws coupled with the high His content of MTP prompted investigation of catechol-oxidase (CO)-like activity because the active CO site is characterized by a dinuclear copper center with each copper coordinated by 3 His residues.⁴⁰ An MBTH-coupled assay was used to determine the kinetic parameters of MTP facilitated catechol oxidation (Fig. 3.4). When bound to 10 eq of copper ions and, assuming each bound copper is an reactive active site, MTP was found to have a $V_{\max} = 0.9 \pm 0.02 \mu\text{M}/\text{min}$, $K_m = 410 \pm 8 \mu\text{M}$, and $k_{\text{cat}} = 0.18 \pm 0.002 \text{ min}^{-1}$. Without copper present there was no detectable activity suggesting that copper is necessary for the reactivity of MTP.

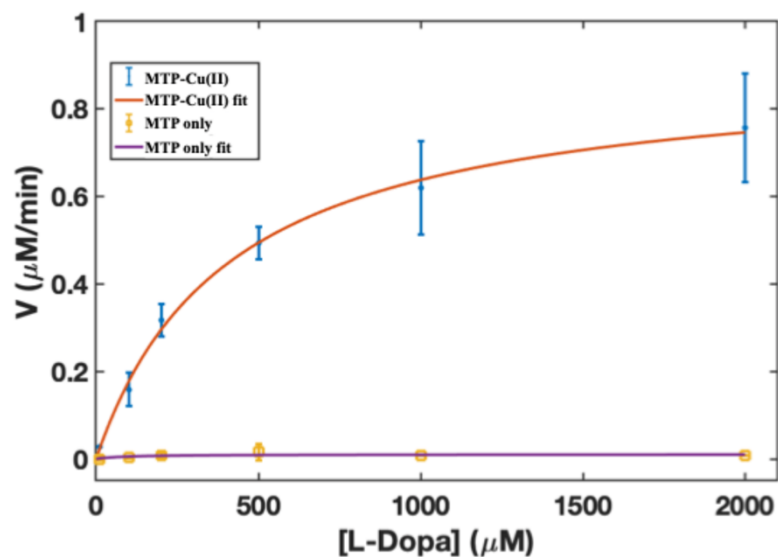


Figure 3.4 Oxidative properties of Cu^{2+} -bound MTP. Reaction rate dependence of L-Dopa oxidation to form the MBTH-quinone adduct carried out in Tris buffer (50mM, pH=7.4) in the presence of $5\mu\text{M}$ MTP and loaded with 10 eq. CuSO_4 (blue dots). The solid red line represents a fit of the data to the Michaelis-Menten equation. Yellow squares are the copper-free MTP reaction rates, with the purple line being the copper-free Michaelis-Menten fit.

Despite our assuming ~ 10 active sites, MTP displays a low reaction rate and an intermediate ability to bind L-Dopa. The slow rate may be adaptive in the jaw system for kinetically controlled growth, as is often necessary for templating complex architectures.⁴¹ It is unlikely that *Glycera* utilizes MTP exclusively to synthesize melanin de novo from Dopa. More plausibly, MTP acts to oxidize the Dopa residues at the growing edge of the jaw thereby enabling cross-link formation between the protein and discrete melanin particles secreted by melanosomes during the formation of a contiguous scaffold. Having a high degree of flexibility and multiple active sites would facilitate this.

vi. Interfacial assembly and viscoelasticity

Interfacial shear rheometry was used to probe the assembly of MTP and the viscoelasticity of resulting films at an air-solution interface (Figure 3.5a). Buffered solutions containing $5\mu\text{M}$ MTP were liquids ($G'' \gg G'$) with very low elastic (G') and viscous (G'') moduli. With

the addition of 50 μM CuSO_4 (10 eq.), however, an interfacial film formed in ~ 1 h. This film likewise showed liquid-like behavior throughout its maturation, but the values of G' and G'' increased steadily, indicating significant thickening of the interfacial viscosity. When 0.5mM L-Dopa was added to a solution mixture of 5 μM MTP, and 50 μM CuSO_4 , the interfacial film persisted, however, it showed signs of structural arrest (within 20 minutes) going from liquid to a viscoelastic film, with $G' \approx G''$.

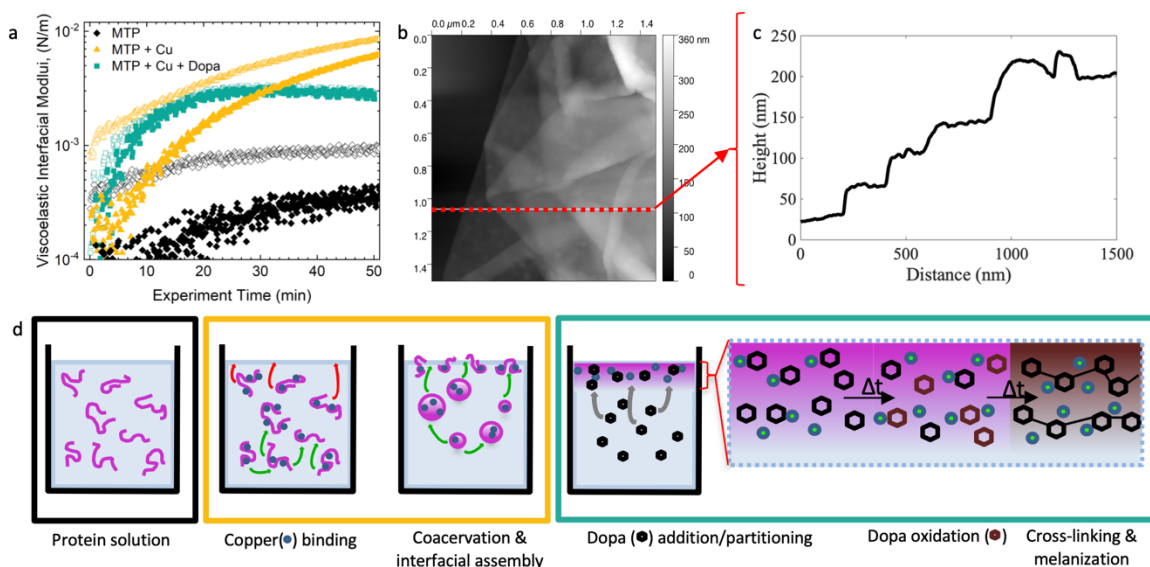


Figure 3.5 Interfacial activity of MTP and film formation. a) Interfacial rheometry: The loss modulus (G'' , open symbols) and storage modulus (G' , filled symbols) as a function of time for 5 μM MTP solutions containing: no copper/Dopa (black), 50 μM CuSO_4 (yellow), or 50 μM CuSO_4 + 500 μM L-Dopa (teal). b) AFM height trace of MTP-melanin films. b) The height profile along the red line in (b) that shows the sheets are ~ 35 -40 nm thick. d) A schematic model depicting the process causing the interfacial responses in (a). Copper binding induces proteins to assemble (red arrows) as well as coacervate and coalesce (green arrows). When present, Dopa molecules partition into the surface layers (grey arrows) where they are oxidized and then crosslink which melanizes the film. The colored boxes around the cartoons are color coordinated with the curves in (a).

Interfacial rheometry experiments were crucial for tracking critical phase transitions in the maturation of MTP-derived films (Figure 3.5d). At pH=7.4 and no copper present, interfacial rheometry revealed a stable liquid behavior in MTP. Upon addition of copper ions

the interfacial viscoelasticity increased steadily while maintaining liquid-like behavior ($G'' > G'$). We propose that this is due to a combination of either charge-neutral coacervate droplets migrating to the hydrophobic air-water interface or the molecular adsorption of copper bound protein complexes.

MTP rapidly formed interfacial films when in the presence of both 10 eq. Cu (II) and 0.5mM L-Dopa at pH 7.4. The equilibrium solution was nearly MTP-depleted within 1h of Cu and Dopa addition as monitored by SDS-PAGE (Figure 3.S4). After ~30 min of reaction, a transparent film formed at the air-water interface that, upon mechanical disruption, folded upon itself to form an insoluble black material. An alkaline-peroxide digestion assay (Materials & Methods) was used to determine that sheets are ~10% melanin by dry weight (Fig. 3.S5). Microscopic inspection of sheets revealed that although individual films were transparent (Fig. 3.S6, red arrows), folded or bundled films appeared black (Fig. 3.S6). Analysis of films by SEM detected large uniform sheets that, due to difficulty in sample manipulation, collapsed into pleated stacks (Fig. 3.S7). Films several square centimeters in area were readily made by spreading the reaction mixture out on glass petri dishes. Furthermore, investigation by AFM showed that these film have a thickness of 37 ± 2 nm (Figure 3.5c).

With Dopa addition and its oxidation to quinones at the protein-rich interface (Figure 3.5d), conditions were sufficient for melanin formation and/or reaction with the lysine or histidine residues of MTP.^{42,43} The change in Dopa-dependent interfacial rheometry, the black color of the bundled sheets (Fig. 3.S6), and the alkaline peroxidation assay (Fig. 3.S5), confirm melanization of the films. This trend was also suggestive of the early stages of jaw formation.

vii. Fiber drawing and mechanics

Because the polymerization was confined to the air-water interface, we attempted to draw fibers from the MTP-melanin film in a manner not unlike the drawing of nylon from interfacial polymerizations.⁴⁴ A large meniscus formed upon contact with a metal probe and persisted during probe withdrawal from the surface of a freshly formed film (Figure 3.6a). The interfacial film folded and compacted as it separated from the bulk and dried in air. Fibers several centimeters in length were readily drawn under these conditions. Typical fiber diameters were 7-11 μm as shown by SEM and light microscopy (Figure 3.6b,c). The SEM image shows fibers with wrinkles that align with the fiber long axis. Amino acid composition remained unchanged during film and fiber formation (Fig. 3.1c, purple bars).

Fibers drawn from melanin-copper-protein films were pulled to failure as shown in Figure 3.6d. The fibers displayed an initial modulus of 1.7 ± 0.5 GPa, a yield strain of $6\pm 2\%$, and a maximum extensibility of $25\pm 5\%$ strain before failing. The average toughness of the fibers was 12.7 ± 3.4 MJ/m³. The properties are summarized and compared with other biological and synthetic fibers (Figure 3.6d; inset Table).⁴⁵⁻⁴⁹ The relatively high stiffness may be due to the cross-linking of protein fibers by melanin despite being present at only 10% by weight. Although this is lower than the roughly 40% melanin levels in native *Glycera* jaws, future work may find ways to increase film melanin content. The large extensibility is inconsistent with a covalently cross-linked system; perhaps, extension or slippage of uncross-linked protein components or the unwinding of bundled sheets are involved. Satisfactory explanation of such properties awaits a better characterization of the relationship between MTP, melanin and copper in the fibers.

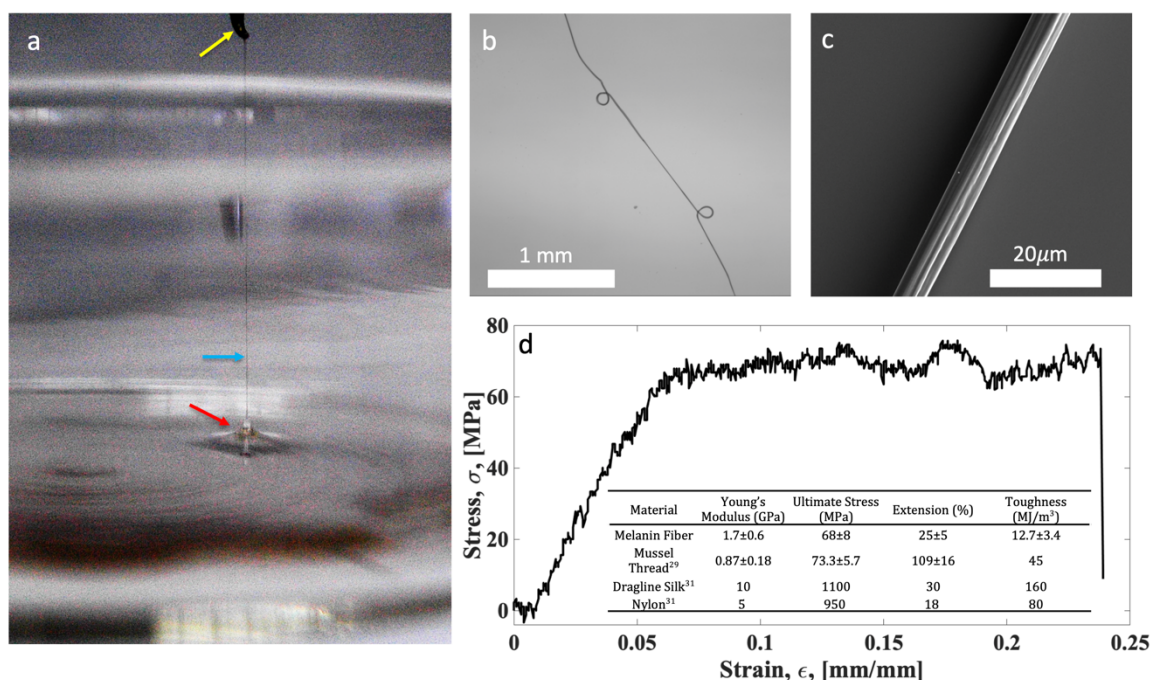


Figure 3.6. Interfacial film formation enables fiber drawing. a) Image of the fiber drawing process. A thick meniscus (red arrow, bottom) forms where the film begins to detach from the solution and collapse into a fiber (blue arrow, middle) after being disturbed by a 1mm steel mechanical probe (yellow arrow, top). b) Optical microscope of melanized-MTP fiber illustrating threads can be pulled to several millimeters in length. c) SEM image of a pulled fiber. Wrinkles are formed that align with the long axis of the fiber in the direction which they were pulled. d) Typical stress-strain curve of melanized MTP fibers. Inset: table comparing the mechanical properties of MTP-melanin fibers with other biological fibers as well as nylon.

D. Discussion

Metal binding proteins are prominent adaptations particularly in natural loadbearing systems²⁶ and are becoming increasingly amenable to bio-inspired translation.⁵⁰ Using recombinant *Glycera* MTP, we have been able to recapitulate important steps *in vitro* that relate to the jaw building process. A key player in this process is MTP which is remarkable for its simple sequence and multi-functionality. Among known functions, phase separation as droplets, film formation, catalysis and structural arrest are all acquired by MTP upon binding copper. High capacity Cu²⁺ binding by MTP is triggered by a pH5.5 to pH7.5 increase, followed in turn by a liquid-liquid phase separation of Cu²⁺-MTP into droplets and a surface

film. Depending on how Dopa partitions with regard to the droplets (Fig. 7a,b), this either constrains the catalyzed oxidation of Dopa to Dopaquinone at the droplet/aqueous phase interface, or within the droplets. Dopaquinone accumulation initiates formation of a second polymer known as melanin. As melanin accrues, the material becomes increasingly solid, enabling, for example, high tensile fibers to be drawn. We propose that the melanin eventually displaces water from the initial hydrogel and in the jaw. The combination of chemical simplicity and functional versatility in MTP holds tremendous potential for bio-inspired and natural materials processing.

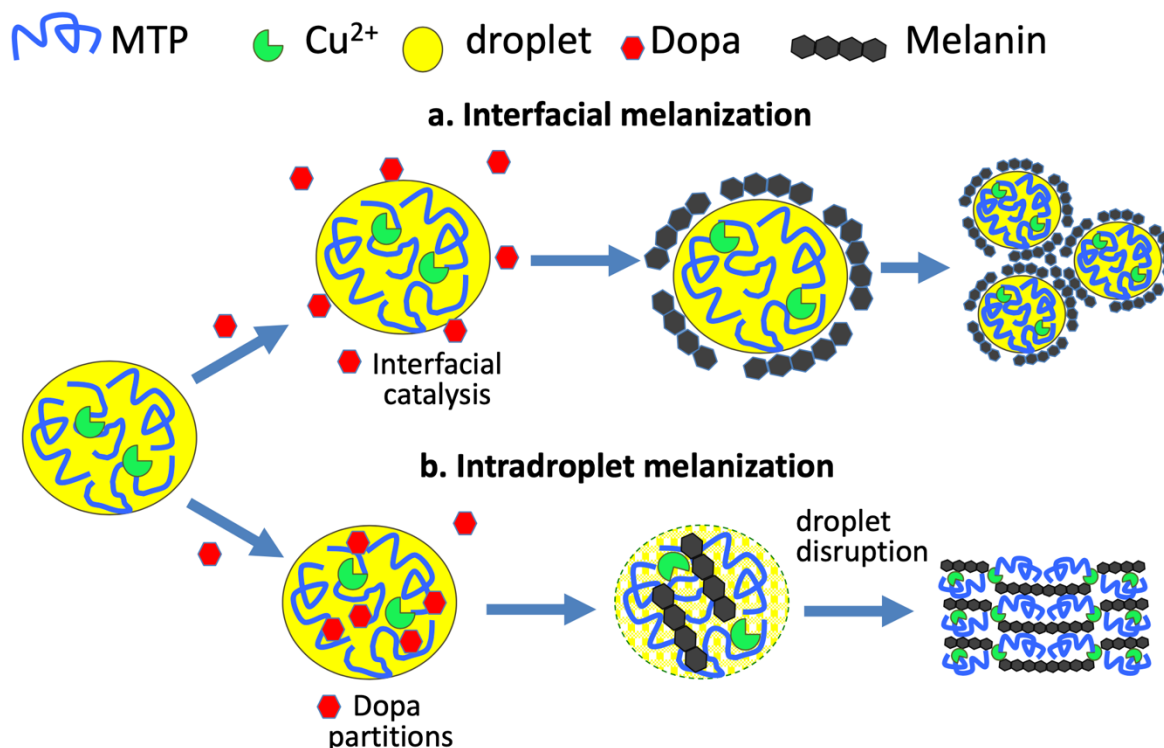


Figure 3.7 Possible modes of MTP melanization depending on Dopa partitioning. a) Dopa does not partition into droplets but is interfacially oxidized to melanin and creates a coating around the droplets. b) Dopa partitions into droplets where it becomes oxidized and accumulates as melanin and disrupts the droplets. Cu ions may also contribute to the interaction between melanin and MTP.

E. Conclusion

The protein component of *Glycera* jaws has an extremely biased composition and is extremely rich in glycine and histidine. Using a transcriptomic approach, we identify MTP as a 22kDa protein whose composition is 50% glycine and 30% histidine and whose sequence is characterized by repeat gly-gly-his motifs. The repeat sequence facilitates high-capacity metal binding, which induces coacervation of MTP. The coacervate droplets assemble at the air-water interface and are capable of inducing oxidation of Dopa, which results in mechanically stable melanized films that are capable of being drawn into threads.

This study provides insight into how bloodworms grow their robust melanin-based jaws. It is likely that MTP both induces crosslinking between melanin in the jaws to induce a contiguous melanin phase in addition to crosslinking itself to the melanin to possibly act as a plasticizer. This paradigm provides the basis for future bioinspired design of melanin-derived materials.

F. References

- (1) Dragan, E. S. Design and Applications of Interpenetrating Polymer Network Hydrogels. A Review. *Chem. Eng. J.* **2014**, *243*, 572–590. <https://doi.org/10.1016/j.cej.2014.01.065>.
- (2) Fan, H.; Gong, J. P. Fabrication of Bioinspired Hydrogels: Challenges and Opportunities. *Macromolecules* **2020**. <https://doi.org/10.1021/acs.macromol.0c00238>.
- (3) Ducrot, E.; Chen, Y.; Bulters, M.; Sijbesma, R. P.; Creton, C. Toughening Elastomers with Sacrificial Bonds and Watching Them Break. *Science (80-.)*. **2014**, *344* (6180), 186–189. <https://doi.org/10.1126/science.1248494>.
- (4) Halloran, J. P.; Sibole, S.; Van Donkelaar, C. C.; Van Turnhout, M. C.; Oomens, C. W. J.; Weiss, J. A.; Guilak, F.; Erdemir, A. Multiscale Mechanics of Articular Cartilage: Potentials and Challenges of Coupling Musculoskeletal, Joint, and Microscale Computational Models. *Ann. Biomed. Eng.* **2012**, *40* (11), 2456–2474. <https://doi.org/10.1007/s10439-012-0598-0>.
- (5) Tan, Y.; Hoon, S.; Guerette, P. A.; Wei, W.; Ghadban, A.; Hao, C.; Miserez, A.; Waite, J. H. Infiltration of Chitin by Protein Coacervates Defines the Squid Beak Mechanical Gradient. *Nat. Chem. Biol.* **2015**, *11* (7), 488–495. <https://doi.org/10.1038/nchembio.1833>.
- (6) Lichtenegger, H. C.; Schöberl, T.; Bartl, M. H.; Waite, H.; Stucky, G. D. High Abrasion Resistance with Sparse Mineralization: Copper Biomineral in Worm Jaws. *Science* **2002**, *298* (5592), 389–392. <https://doi.org/10.1126/science.1075433>.
- (7) Moses, D. N.; Harreld, J. H.; Stucky, G. D.; Waite, J. H. Melanin and Glycera Jaws. *J. Biol. Chem.* **2006**, *281* (46), 34826–34832. <https://doi.org/10.1074/jbc.M603429200>.
- (8) Clancy, C. M. R.; Simon, J. D. Ultrastructural Organization of Eumelanin from *Sepia Officinalis* Measured by Atomic Force Microscopy. *Biochemistry* **2001**, *40* (44), 13353–13360. <https://doi.org/10.1021/bi010786t>.
- (9) Hill, H. Z. The Function of Melanin or Six Blind People Examine an Elephant. *BioEssays* **1992**, *14* (1), 49–56. <https://doi.org/10.1002/bies.950140111>.
- (10) Pontin, M. G.; Moses, D. N.; Waite, J. H.; Zok, F. W. A Nonmineralized Approach to Abrasion-Resistant Biomaterials. *Proc. Natl. Acad. Sci. U. S. A.* **2007**, *104* (34), 13559–13564. <https://doi.org/10.1073/pnas.0702034104>.
- (11) Afgan, E.; Baker, D.; van den Beek, M.; Blankenberg, D.; Bouvier, D.; Čech, M.; Chilton, J.; Clements, D.; Coraor, N.; Eberhard, C.; Grüning, B.; Guerler, A.; Hillman-Jackson, J.; Von Kuster, G.; Rasche, E.; Soranzo, N.; Turaga, N.; Taylor, J.; Nekrutenko, A.; Goecks, J. The Galaxy Platform for Accessible, Reproducible and Collaborative Biomedical Analyses: 2016 Update. *Nucleic Acids Res.* **2016**, *44* (W1), W3–W10. <https://doi.org/10.1093/nar/gkw343>.
- (12) Haas, B. J.; Papanicolaou, A.; Yassour, M.; Grabherr, M.; Blood, P. D.; Bowden, J.; Couger, M. B.; Eccles, D.; Li, B.; Lieber, M.; MacManes, M. D.; Ott, M.; Orvis, J.; Pochet, N.; Strozzi, F.; Weeks, N.; Westerman, R.; William, T.; Dewey, C. N.; Henschel, R.; LeDuc, R. D.; Friedman, N.; Regev, A. De Novo Transcript Sequence Reconstruction from RNA-Seq Using the Trinity Platform for Reference Generation and Analysis. *Nat. Protoc.* **2013**, *8* (8), 1494–1512. <https://doi.org/10.1038/nprot.2013.084>.

- (13) Li, B.; Dewey, C. N. RSEM: Accurate Transcript Quantification from RNA-Seq Data with or without a Reference Genome. *BMC Bioinformatics* **2011**, *12* (1), 323. <https://doi.org/10.1186/1471-2105-12-323>.
- (14) WINDER, A. J.; HARRIS, H. New Assays for the Tyrosine Hydroxylase and Dopa Oxidase Activities of Tyrosinase. *Eur. J. Biochem.* **1991**, *198* (2), 317–326. <https://doi.org/10.1111/j.1432-1033.1991.tb16018.x>.
- (15) Rodriguezlopez, J. N.; Escribano, J.; Garciacanovas, F. A Continuous Spectrophotometric Method for the Determination of Monophenolase Activity of Tyrosinase Using 3-Methyl-2-Benzothiazolinone Hydrazone. *Anal. Biochem.* **1994**, *216* (1), 205–212. <https://doi.org/10.1006/abio.1994.1026>.
- (16) Napolitano, A.; Pezzella, A.; Vincensi, M. R.; Prota, G. Oxidative Degradation of Melanins to Pyrrole Acids: A Model Study. *Tetrahedron* **1995**, *51* (20), 5913–5920. [https://doi.org/10.1016/0040-4020\(95\)00259-B](https://doi.org/10.1016/0040-4020(95)00259-B).
- (17) Ito, S. Reexamination of the Structure of Eumelanin. *BBA - Gen. Subj.* **1986**, *883* (1), 155–161. [https://doi.org/10.1016/0304-4165\(86\)90146-7](https://doi.org/10.1016/0304-4165(86)90146-7).
- (18) Ito, S.; Wakamatsu, K.; Ozeki, H. Spectrophotometric Assay of Eumelanin in Tissue Samples. *Analytical Biochemistry*. 1993, pp 273–277. <https://doi.org/10.1006/abio.1993.1586>.
- (19) Vandebril, S.; Franck, A.; Fuller, G. G.; Moldenaers, P.; Vermant, J. A Double Wall-Ring Geometry for Interfacial Shear Rheometry. *Rheol. Acta* **2010**, *49* (2), 131–144. <https://doi.org/10.1007/s00397-009-0407-3>.
- (20) Dana Novak Moses. Structure, Biochemistry, and Mechanical Properties of Glycera Marine Worm Jaws. **2007**, No. September, 177.
- (21) Broomell, C. C.; Chase, S. F.; Laue, T.; Waite, J. H. Cutting Edge Structural Protein from the Jaws of Nereis Virens. *Biomacromolecules* **2008**, *9* (6), 1669–1677. <https://doi.org/10.1021/bm800200a>.
- (22) Voss-Foucart, M. F.; Fonze-Vignaux, M. T.; Jeuniaux, C. Systematic Characters of Some Polychaetes (Annelida) at the Level of the Chemical Composition of the Jaws. *Biochem. Syst. Ecol.* **1973**, *1* (2), 119–122. [https://doi.org/10.1016/0305-1978\(73\)90025-2](https://doi.org/10.1016/0305-1978(73)90025-2).
- (23) Ringli, C.; Keller, B.; Ryser, U. Glycine-Rich Proteins as Structural Components of Plant Cell Walls. *Cell. Mol. Life Sci.* **2001**, *58* (10), 1430–1441. <https://doi.org/10.1007/PL00000786>.
- (24) Xu, M.; Lewis, R. V. Structure of a Protein Superfiber: Spider Dragline Silk. *Proc. Natl. Acad. Sci. U. S. A.* **1990**, *87* (18), 7120–7124. <https://doi.org/10.1073/pnas.87.18.7120>.
- (25) Brown-Augsburger, P.; Tisdale, C.; Broekelmann, T.; Sloan, C.; Mecham, R. P. Identification of an Elastin Cross-Linking Domain That Joins Three Peptide Chains. *Journal of Biological Chemistry*. 1995, pp 17778–17783. <https://doi.org/10.1074/jbc.270.30.17778>.
- (26) Degtyar, E.; Harrington, M. J.; Politi, Y.; Fratzl, P. The Mechanical Role of Metal Ions in Biogenic Protein-Based Materials DON'T USE FOR THESIS. *Angew. Chemie - Int. Ed.* **2014**, *53* (45), 12026–12044. <https://doi.org/10.1002/anie.201404272>.
- (27) Micsonai, A.; Wien, F.; Kerya, L.; Lee, Y. H.; Goto, Y.; Réfrégiers, M.; Kardos, J. Accurate Secondary Structure Prediction and Fold Recognition for Circular

- Dichroism Spectroscopy. *Proc. Natl. Acad. Sci. U. S. A.* **2015**, *112* (24), E3095–E3103. <https://doi.org/10.1073/pnas.1500851112>.
- (28) Zgirski, A.; Frieden, E. Binding of Cu(II) to Non-Prosthetic Sites in Ceruloplasmin and Bovine Serum Albumin. *J. Inorg. Biochem.* **1990**, *39* (2), 137–148. [https://doi.org/10.1016/0162-0134\(90\)80022-P](https://doi.org/10.1016/0162-0134(90)80022-P).
- (29) Masuoka, J.; Hegenauer, J.; Van Dyke, B. R.; Saltman, P. Intrinsic Stoichiometric Equilibrium Constants for the Binding of Zinc(II) and Copper(II) to the High Affinity Site of Serum Albumin. *J. Biol. Chem.* **1993**, *268* (29), 21533–21537.
- (30) Harford, C.; Sarkar, B. Amino Terminal Cu(II)- and Ni(II)-Binding (ATCUN) Motif of Proteins and Peptides: Metal Binding, DNA Cleavage, and Other Properties. *Acc. Chem. Res.* **1997**, *30* (3), 123–130. <https://doi.org/10.1021/ar9501535>.
- (31) Casolaro, M.; Chelli, M.; Ginanneschi, M.; Laschi, F.; Messori, L.; Muniz-Miranda, M.; Papini, A. M.; Kowalik-Jankowska, T.; Kozłowski, H. Spectroscopic and Potentiometric Study of the SOD Mimic System Copper(II)/Acetyl-L-Histidylglycyl-L-Histidylglycine. *J. Inorg. Biochem.* **2002**, *89* (3–4), 181–190. [https://doi.org/10.1016/S0162-0134\(02\)00365-3](https://doi.org/10.1016/S0162-0134(02)00365-3).
- (32) Paksi, Z.; Jakab, N.; Gyurcsik, B.; Rockenbauer, A.; Gajda, T. Solution Chemical Properties and Catecholase-like Activity of the Copper(. *Dalt. Trans.* **2005**, 3187–3194.
- (33) Bonomo, R. P.; Impellizzeri, G.; Pappalardo, G.; Purrello, R.; Rizzarelli, E.; Tabbi, G. Co-Ordinating Properties of Cyclopeptides. Thermodynamic and Spectroscopic Study on the Formation of Copper(II) Complexes with Cyclo(Gly-His)₄ and Cyclo(Gly-His-Gly)₂ and Their Superoxide Dismutase-like Activity. *J. Chem. Soc. Dalt. Trans.* **1998**, No. 22, 3851–3858. <https://doi.org/10.1039/a804481c>.
- (34) Szabó-Plánka, T.; Peintler, G.; Rockenbauer, A.; Győr, M.; Varga-Fábián, M.; Institórisz, L.; Balázspiri, L. Electron Spin Resonance Study of Copper(II) Complexes of X-Glycine and Glycyl-X Type Dipeptides, and Related Tripeptides. Variation of Co-Ordination Modes with Ligand Excess and PH in Fluid and Frozen Aqueous Solutions. *J. Chem. Soc., Dalt. Trans.* **1989**, No. 10, 1925–1932. <https://doi.org/10.1039/DT9890001925>.
- (35) Peisach, J.; Blumberg, W. E. Structural Implications Derived from the Analysis of Electron Paramagnetic Resonance Spectra of Natural and Artificial Copper Proteins. *Arch. Biochem. Biophys.* **1974**, *165* (2), 691–708. [https://doi.org/10.1016/0003-9861\(74\)90298-7](https://doi.org/10.1016/0003-9861(74)90298-7).
- (36) Uversky, V. N.; Kuznetsova, I. M.; Turoverov, K. K.; Zaslavsky, B. Intrinsically Disordered Proteins as Crucial Constituents of Cellular Aqueous Two Phase Systems and Coacervates. *FEBS Lett.* **2015**, *589* (1), 15–22. <https://doi.org/10.1016/j.febslet.2014.11.028>.
- (37) Martin, E. W.; Mittag, T. Relationship of Sequence and Phase Separation in Protein Low-Complexity Regions. *Biochemistry* **2018**, *57* (17), 2478–2487. <https://doi.org/10.1021/acs.biochem.8b00008>.
- (38) Wang, J.; Cohen Stuart, M. A.; Van Der Gucht, J. Phase Diagram of Coacervate Complexes Containing Reversible Coordination Structures. *Macromolecules* **2012**, *45* (21), 8903–8909. <https://doi.org/10.1021/ma301690t>.
- (39) Hwang, D. S.; Zeng, H.; Srivastava, A.; Krogstad, D. V.; Tirrell, M.; Israelachvili, J. N.; Waite, J. H. Viscosity and Interfacial Properties in a Mussel-Inspired Adhesive

- Coacervate. *Soft Matter* **2010**, *6* (14), 3232. <https://doi.org/10.1039/c002632h>.
- (40) Solomon, E. I.; Sundaram, U. M.; Machonkin, T. E. Multicopper Oxidases and Oxygenases. *Chem. Rev.* **1996**, *96* (7), 2563–2605. <https://doi.org/10.1021/cr950046o>.
- (41) Brutchey, R. L.; Morse, D. E. Silicatein and the Translation of Its Molecular Mechanism of Biosilicification into Low Temperature Nanomaterial Synthesis. *Chem. Rev.* **2008**, *108* (11), 4915–4934. <https://doi.org/10.1021/cr078256b>.
- (42) Miserez, A.; Rubin, D.; Waite, J. H. Cross-Linking Chemistry of Squid Beak. *J. Biol. Chem.* **2010**, *285* (49), 38115–38124. <https://doi.org/10.1074/jbc.M110.161174>.
- (43) Wang, S. X.; Mure, M.; Medzihradzky, K. F.; Burlingame, A. L.; Brown, D. E.; Dooley, D. M.; Smith, A. J.; Kagan, H. M.; Klinman, J. P. A Crosslinked Cofactor in Lysyl Oxidase: Redox Function for Amino Acid Side Chains. *Science (80-)*. **1996**, *273* (5278), 1078–1084. <https://doi.org/10.1126/science.273.5278.1078>.
- (44) Kang, M.; Myung, S. J.; Jin, H.-J. Nylon 610 and Carbon Nanotube Composite by in Situ Interfacial Polymerization. *Polymer (Guildf)*. **2006**, *47* (11), 3961–3966. <https://doi.org/10.1016/j.polymer.2006.03.073>.
- (45) Harrington, M. J.; Waite, J. H. PH-Dependent Locking of Giant Mesogens in Fibers Drawn from Mussel Byssal Collagens. *Biomacromolecules* **2008**, *9* (5), 1480–1486. <https://doi.org/10.1021/bm8000827>.
- (46) Fu, J.; Guerette, P. A.; Pavesi, A.; Horbelt, N.; Lim, C. T.; Harrington, M. J.; Miserez, A. Artificial Hagfish Protein Fibers with Ultra-High and Tunable Stiffness. *Nanoscale* **2017**, *9* (35), 12908–12915. <https://doi.org/10.1039/c7nr02527k>.
- (47) Bell, E. C.; Gosline, J. M. Mechanical Design of Mussel Byssus: Material Yield Enhances Attachment Strength. *J. Exp. Biol.* **1996**, *199* (4), 1005–1017. <https://doi.org/10.1016/j.jembe.2006.10.011>.
- (48) Gosline, J.; Lillie, M.; Carrington, E.; Guerette, P.; Ortlepp, C.; Savage, K. Elastic Proteins: Biological Roles and Mechanical Properties. *Philos. Trans. R. Soc. B Biol. Sci.* **2002**, *357* (1418), 121–132. <https://doi.org/10.1098/rstb.2001.1022>.
- (49) Gosline, J. M.; Guerette, P. A.; Ortlepp, C. S.; Savage, K. N. The Mechanical Design of Spider Silks: From Fibroin Sequence to Mechanical Function. *J. Exp. Biol.* **1999**, *202* (23), 3295–3303.
- (50) Filippidi, E.; Cristiani, T. R.; Eisenbach, C. D.; Herbert Waite, J.; Israelachvili, J. N.; Kollbe Ahn, B.; Valentine, M. T. Toughening Elastomers Using Mussel-Inspired Iron-Catechol Complexes. *Science (80-)*. **2017**, *358* (6362), 502–505. <https://doi.org/10.1126/science.aao0350>.

G. Supplemental figures for Chapter 3

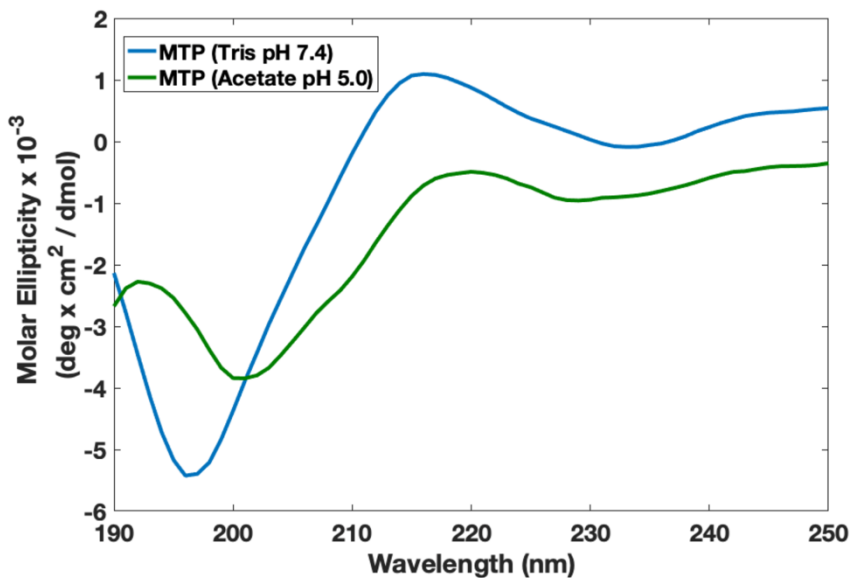


Figure 3.S1 Solution conformation of MTP as a function of pH. The blue curve is 50 μ M MTP in 50mM Tris (pH=7.4). The green curve is 50 μ M MTP in 50mM sodium acetate (pH=5.0).

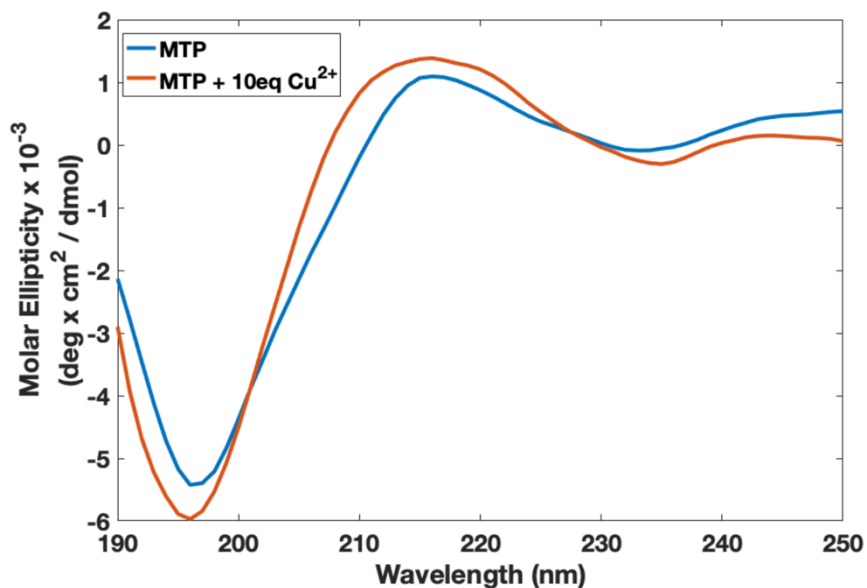


Figure 3.S2 Copper dependence of MTP solution conformation. The blue curve is 5 μ M MTP in 50mM Tris (pH=7.4). The red curve is 50 μ M MTP in 50mM Tris (pH = 7.4) supplemented with 100 μ M CuSO₄

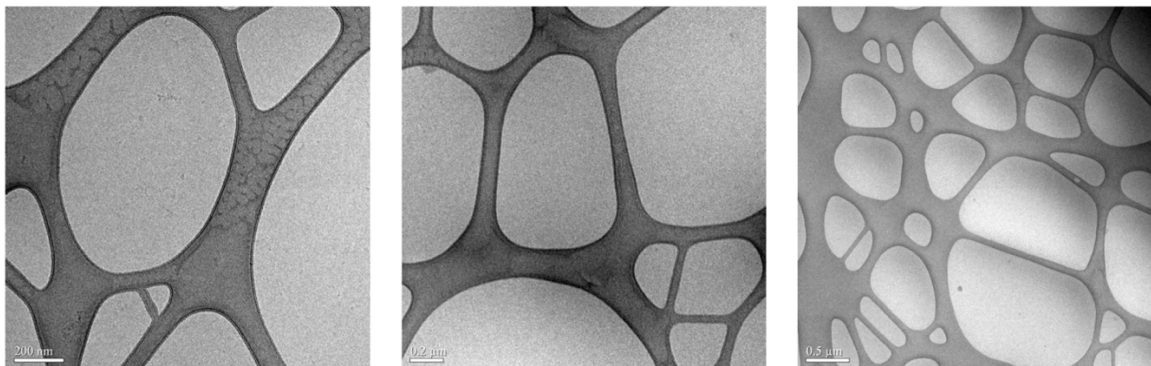


Figure 3.S3 Cryo-TEM of MTP In the absence of Cu^{2+} . The cryo-TEM of $5\mu\text{M}$ MTP in 50mM Tris buffer ($\text{pH} = 7.5$) shows no evidence of phase separation

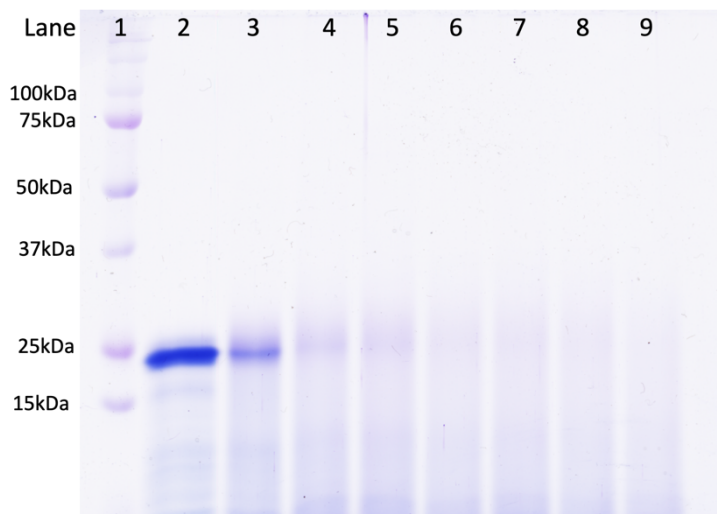


Figure 3.S4 Time course of MTP-melanin reaction monitored by SDS-PAGE. The reaction contained $5\mu\text{M}$ MTP, $50\mu\text{M}$ CuSO_4 , 100mM Tris ($\text{pH} = 7.4$) and 0.5mM L-Dopa. Lane 1 is the reference ladder and lanes 2-9 represent $t = 0, 15\text{min}, 30\text{min}, 45\text{min}, 1\text{ hour}, 2\text{ hours}, 4\text{ hours},$ and 12 hours .

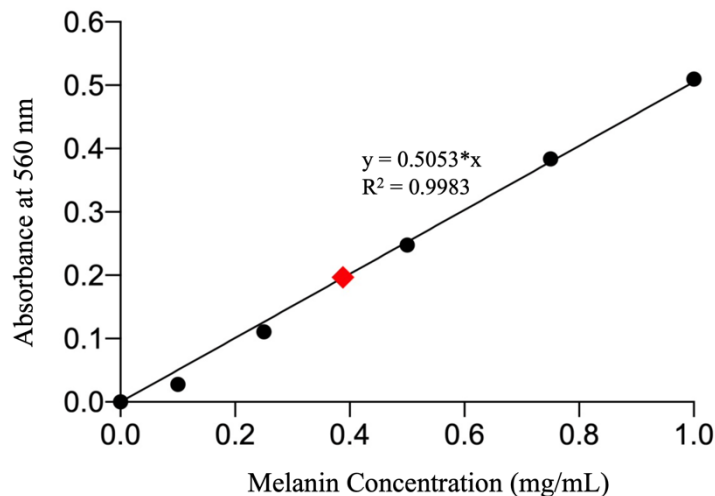


Figure 3.S5 Determination of melanin degradation products. A standard curve was created by dissolving synthetic melanin in alkaline peroxide at 0.1, 0.2, 0.5, 0.75, and 1 mg/mL (black circles) and measuring the absorbance at 560nm, and fit with a best-fit line whose Y intercept was forced to be zero. A sample of washed and isolated MTP-melanin film was similarly prepared at 4 mg/mL and its absorbance measured (red diamond) and its absorbance of 0.197 AU corresponds to a melanin concentration of 0.4mg/mL, indicating the sample is 10% melanin by mass.

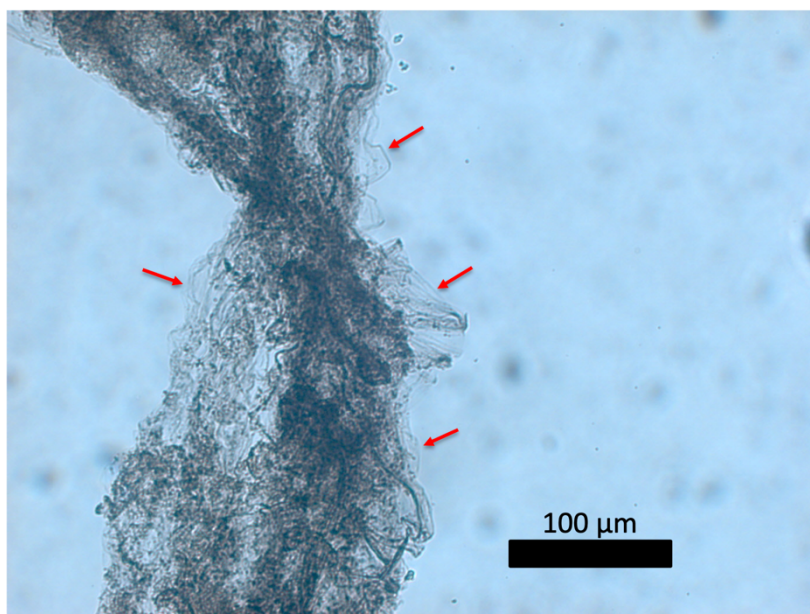


Figure 3.S6 Observation of MTP-melanin film under a light microscope. Interfacial films appear black, which indicates their melanization. The film also exhibits what appears to be semi-transparent folds (indicated by red arrows) around the edges of the film where likely only one layer is present.

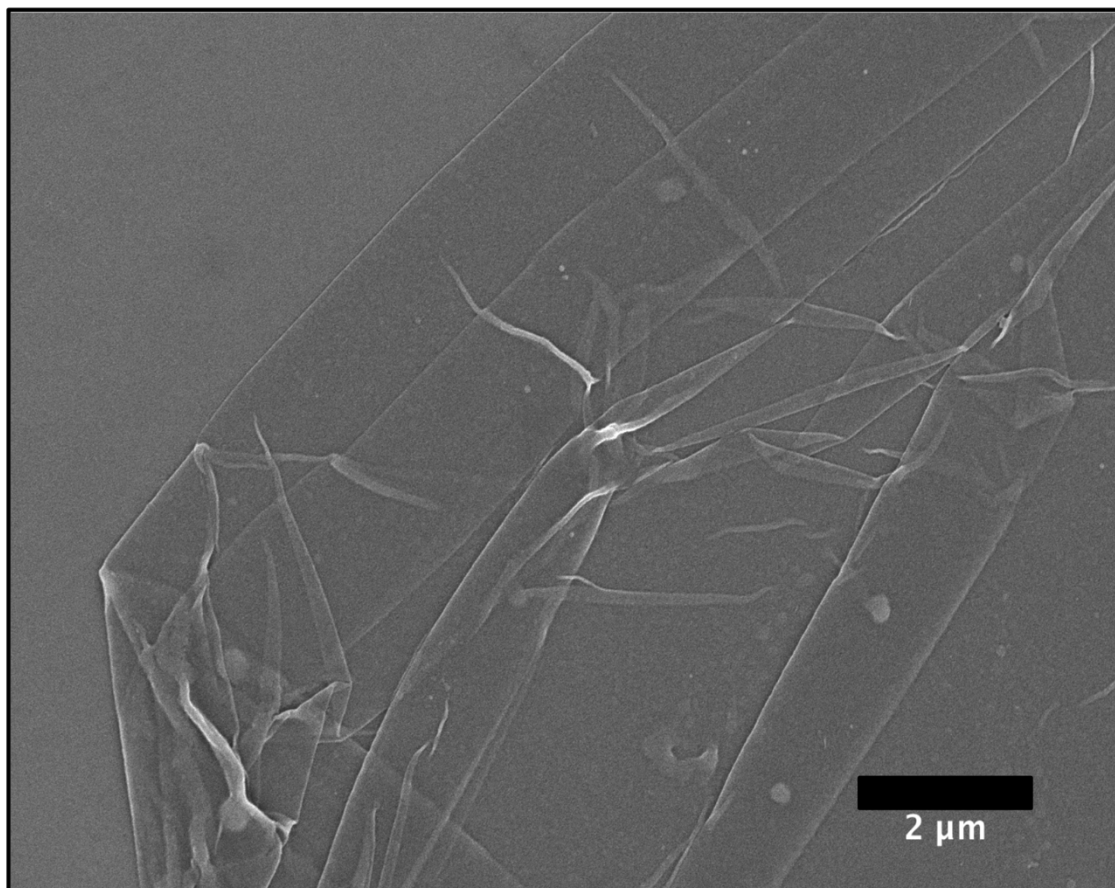


Figure 3.S7 SEM image of an MTP-melanin film. The film was transferred to a silicon substrate after 1 hour of assembly/reaction.

Chapter 4

The biochemistry and mechanics of octopus egg cases

A. Abstract

The role intramolecular crosslinks play in the mechanical response of polymeric systems has seen greater attention in recent years due to their effect on polymer mechanics, but studies have been limited due to synthetic challenges. There are many systems in nature that utilize intramolecular crosslinks, and as a result their contribution to mechanical behavior has been more readily studied in a biochemical context. Herein we find that the reproductive egg case of *Octopus bimaculoides* is an ideal model system for studying the effects on intramolecular crosslinking. The principal component of octopus threads is a protein with 29 repeat epidermal growth factor (EGF) domains, each of which contains 3 intramolecular disulfide linkages, that assembles to form fibrous bundles. Mechanical testing shows that the regularly spaced disulfide linkages result in improved modulus and yields a system that behaves like a semicrystalline elastomer. We perform molecular dynamics and X-ray scattering in this study to show that EGF-like domains deform in response to mechanical strain. The results of this study further the understanding of intramolecular crosslinking and provide a foundation for the mechanical nature of EGF domains.

B. Introduction

Intermolecular crosslink density lies at core of the mechanical properties of polymeric materials.¹ The conventional wisdom on *intramolecular* crosslinks, on the other hand, has been that they contribute minimally to the mechanical properties of synthetic systems² but this has recently been called into question. A study on the bulk mechanical properties of a single-

chain nanoparticle (SCNP) has found that introducing intramolecular crosslinks can result in increased stiffness and extension.³ In view of this, further exploration the mechanical effects of intramolecular crosslinks has much to recommend it, however, the synthesis of SCNPs has a number of limitations including scalability, crosslink selectivity, domain size, and number of available 3D architectures.⁴ In biology, however, intramolecular crosslinks are readily achieved and often are used for mechanical purposes. Thus, we might gain a great deal of inspiration by understanding how biology uses intramolecular crosslinks.

Mechanical studies on immunoglobulin (Ig) domains, which contribute to the strength and elasticity of titin, have shown that intramolecular hydrogen bonds break during domain unfolding in response to strain.^{5,6} Additionally, there have been penetrating studies on the importance of intramolecular interactions in elastin⁷ as well as spider silks.⁸ Another aspect of intramolecular crosslinks is that they reduce the available geometries the system can take on, effectively introducing topological constraints. Proteins that possess non-trivial geometrical motifs in their native state (i.e. the polypeptides are intertwined, or knotted, or have covalent links) that cause them to be self-constrained often yield unconventional mechanical effects. Numerous computational and experimental studies have investigated how topological constraints affect the mechanical response of a protein.⁹⁻¹⁸ However, these studies focus on the response of individual proteins rather than bulk properties. Therefore, it would be advantageous to find system in which correlations between crosslinking, complex topology, and bulk mechanical properties can be investigated. Despite recent interest, however, there are still many motifs left to be studied.

The epidermal growth factor (EGF)-like domain is one such self-constrained motif yet its mechanical behavior is largely unknown.¹⁹ EGF-like domains are relatively short

polypeptides (30-40 length amino acids) that host three intramolecular disulfide (DS) bonds, that in turn create three constrained loops in the native state²⁰ (Fig. 4.1).

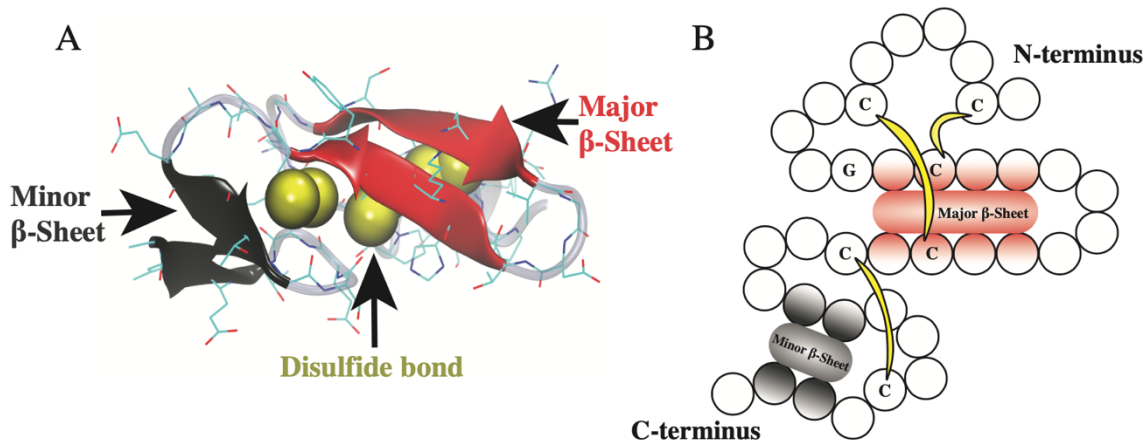


Figure 4.1. The EGF domain. (A) The molecular model of an EGF domain that contains a major β -sheet (red), minor β -sheet (black) and 3 disulfide bonds (yellow spheres). (B) Cartoon representation of the EGF topology with certain conserved residues indicated.

EGF-like domains are commonly featured in a variety of Extracellular Matrix (ECM) and proteins and have number of functions attributed to them, such as cellular recognition and signaling.²¹ The most notable protein rich in these motifs is fibrillin, which, as it contains as many as 47 EGF-like domains, necessarily has a high degree of intramolecular crosslinking.²² Although this would appear to make fibrillin an ideal system to investigate these questions, there are several confounding factors. Fibrillin is typically found in the presence of elastin, to such an extent that fibrillin is suggested to provide a scaffold for elastin deposition.²³ Thus, the association of other proteins overshadows the mechanical response of the EGF-like domains. Additionally, fibrillin features a complex “pseudo beaded string” ultrastructure, the molecular nature of which is disputed.^{24–26} The mechanical response of fibrillin has largely been explained in terms of the ultrastructure and global deformation rather than the segmental rearrangements of the individual EGF motifs. Indeed, mechanical investigations of other

proteins that feature EGF-like domains have largely ignored their contribution.^{27,28} As such, there remains tremendous opportunity for describing how the intramolecular crosslinked, topologically constrained, EGF-like motif contributes to bulk mechanical behavior.

In this study we have identified the reproductive egg cases of *Octopus bimaculoides* as an ideal model system to address the aforementioned opportunity. The cases are robust and must be long-lived as the brooding period is several months.²⁹ We find that the egg cases are predominantly composed of a novel protein, which we term *octovafibrin* (for octopus ovarian fibrous protein) that consists of 29 tandemly repeat EGF units terminated at both ends by lectin binding domains. This system is advantageous because the encasement that tapers at one end to form a thread that provides an ideal geometry for tensile testing. The bulk tensile properties (strain to failure and cyclic) of the egg threads, as well as the associated changes in optical properties were investigated. We employed coarse-grained Molecular Dynamics (MD) simulations to provide a systematic study intended to characterize the influence of the topological constraints and intramolecular of EGF-like motifs, created by the DS bonds, on the mechanical response of the octopus egg threads. To understand the molecular mechanism and the subsequent local structural unfolding by which EGF-like domains respond to mechanical loading, a combination of wide-angle x-ray scattering (WAXS) and molecular modeling techniques were used. Finally, we investigate the effects of the intramolecular DS bonds by analyzing the mechanical response of threads after treatment with a reducing agent.

C. Materials & Methods

i. Egg Thread Collection and Microscopy

Adult *Octopus bimaculoides* specimens were collected near Santa Barbara, CA and kept in an open seawater system at the University of California Santa Barbara. Octopuses were held for several weeks and monitored for egg laying. Once the females laid eggs, the egg bundles were collected and freshly separated under a dissecting microscope to obtain tens of milligrams of isolated egg threads. The egg threads were then rinsed in filtered (0.2 μm) seawater before experiments were conducted.

The egg threads were prepared for scanning electron microscopy (SEM) by fixing in 1% formaldehyde in marine phosphate buffered saline (0.05 M sodium phosphate, 0.45 M NaCl, pH = 7.4), both in the relaxed state and under 100% strain, for 4 hours at 4°C. Next, the egg threads were rinsed with fresh water and then transferred to 100% ethanol through a graded series of solutions. The egg threads were then transferred into 100% hexamethyldisilazane (HMDS) through a series of HMDS/ethanol solutions. Finally, the egg threads were dried directly on SEM stubs covered with carbon tape and silicon wafer, coated with a thin film of gold (JFC-16000 sputter coater, JEOL), and imaged using an FEI Nova Nano 650 FEG SEM operating at 3keV.

Egg threads were prepared for transmission electron microscopy (TEM) by fixing in 2% formaldehyde, and 2.5% glutaraldehyde, in fixation buffer (200 mM sodium cacodylate, 300 mM NaCl, pH 7.2) for 2 hours on ice. The samples were washed 3 times (10 minutes each) in degassed fixation buffer, and then post-fixed in 2% osmium tetroxide in degassed fixation buffer for 2 hours. Following this step, the samples were then washed 4 times (10 minutes each) with room temperature degassed deionized water, and then dehydrated through a graded series of ethanol washes. The sample was then transferred from ethanol to into 100% propylene oxide in a graded solvent series. The samples were submerged in resin diluted in

propylene oxide to infiltrate them with epoxy resin (Embed812, Electron Microscopy Sciences, Hatfield, USA) as follows: 33% (2 hours), 66% (16 hours), and 100% (4 hours). Finally, samples were placed in silicon molds and cured at 60°C for 24 hours. Thin sections (60-80 nm) for TEM, and semi-thin sections (500 nm) for bright field light microscopy were cut on an EM UC6 Ultramicrotome (Leica Biosystems, Wetzlar, Germany). TEM sections were mounted on copper grids (CF200, Electron Microscopy Sciences, Washington D.C., USA) and post-stained with drops of uranyl acetate and lead citrate following standard protocols³⁰.

ii. Biochemical analysis

Fresh egg threads were rinsed in deionized water and placed directly into SDS-PAGE sample buffer (50mM Tris HCl, 10% v/v glycerol, 2% w/v SDS, 0.1% w/v bromophenol blue, pH 6.8) with and without 100 mM β -mercaptoethanol (β -ME), and with and without being heated to 95°C, for 5 minutes. Samples were resolved on 10% Tris-Glycine acrylamide protein gels, at 125V, for 50 minutes. The protein molecular weight was estimated based on a standard protein ladder.

The major protein of the egg thread, *octovafibrin*, was resolved using SDS-PAGE again and the band extracted for an in-gel trypsin digest and prepared for and analyzed by LC/MS/MS following standard protocols described by the University of California San Francisco Mass Spectrometry Facility.^{31,32} Several protein fragments were de novo sequenced based on the fragmentation patterns.

A fresh mature female specimen of *Octopus bimaculoides* was dissected and the oviducal glands were isolated for transcriptomic analysis. RNA was purified from the tissue using a Purelink RNA isolation kit (ThermoFisher Scientific, Waltham, MA) following the

manufacturer's protocol for homogenization with a mortar and pestle, and liquid nitrogen. RNA quality was assessed on a TapeStation 2200 (Agilent Technologies, Santa Clara, CA) and quantified using a Cubit 2.0 Fluorometer. The mRNA was purified using Dynabeads® Oligo (dT)25 (ThermoFisher Scientific), and the RNA library was prepared using the TruSeq Stranded mRNA Library Prep Kit (Illumina, San Diego, CA) and sequenced on a NextSeq 500 (Illumina) running at 150 cycles. The sequencing reads were trimmed using the Trimmomatic processing tool³³ and assembled using the Trinity software package³⁴. The entire transcriptome was searched for transcripts matching the de novo protein fragments determined from mass spectroscopy. One large isotig contained many matching fragments to the de novo-generated sequences and the full open reading frame had approximately the expected molecular weight.

Amino acid analysis (AAA) was performed on a Hitachi L-8900 ninhydrin based amino acid analyzer. Fresh egg threads (1 day old) and aged egg threads (100 days old) were analyzed for quantitative protein and amino acid. The putative 135 kDa gel band was also analyzed for comparison. A freshly run gel was electro-transferred to a PVDF membrane with a transblot apparatus (Biorad) in transfer buffer (25 mM Tris, 192 mM glycine, and 20% v/v methanol) at 25 V for 15 min. The 135 kDa band was cut from the membrane. Protein samples for AAA were hydrolyzed in 6M HCl under vacuum at 110°C for 24 hrs, rinsed multiple times with water and methanol, reconstituted in 0.02M HCl, and loaded onto the system. Inductively Coupled Plasma-Atomic Emission Spectroscopy (ICP-AES) was performed on a Thermo iCAP 6300, with a sample uptake rate of 1.5 mL/min. Egg threads were prepared by hydrolysis in 5% nitric acid and diluted to 1% before analysis. Calcium concentrations in the egg thread were the same as ambient seawater.

iii. Mechanical Testing

Tensile loading and cyclic loading tests were performed on a tabletop tensile tester (Bionix 200 universal testing machine, MTS, Eden Prairie, MN), at a nominal strain rate of 1.0 min^{-1} , using a 10 N load cell and a built-in optical encoder to measure the load and displacement. Command of the motor is performed with the built-in MTS TestSuite software (MTS, Eden Prairie, MN). All mechanical tests were performed with the threads fully submerged in filtered seawater inside an environmental chamber (Bionix 200 universal testing machine, MTS, Eden Prairie, MN). Threads were clamped with stainless steel grips and those under tensile loading experiments are pulled to failure. Threads undergoing cyclic loading are pulled to various strains and returned to zero strain. Threads that broke at the clamp-interface were not recorded. Mechanical tests are run under multiple conditions and configurations. Stress relaxation experiments were conducted in the same manner, samples were adhered to tabs and pulled on at a strain rate of 100 min^{-1} . The strain was held constant for 10 minutes, and stress was recorded over this time. To study the effect of reducing DS linkages, threads were pre-treated in artificial seawater supplemented with a range of DTT concentrations (0.001, 0.01, 0.1, 1.0, and 10mM) for one hour prior to testing. All mechanical data was processed using MATLAB (Mathworks, Natick, MA).

iv. Transparency measurements

The transparency of the egg threads changes during cyclic loading. Photographs of the thread were taken at different strains using a Canon Rebel SLR during successive pulling cycles as described above. The change in contrast relative to the background (Weber contrast) was used to represent change in transparency. The integrated intensity of the threads and background were analyzed using ImageJ (NCBI).

v. Wide angle X-ray scattering (WAXS)

Transmission WAXS experiments were performed at the University of California Santa Barbara Materials Research Lab X-ray diffraction facility. Diffraction patterns were acquired using custom-built X-ray diffractometer equipped with a 50-micron microfocus 1.54 Å Cu X-ray source (Genix from XENOCs SA, France) and an EIGER R 1M solid state detector (Dectris, Switzerland) at a sample-to-detector distance of 157mm.

Threads were pulled to 70% strain and held at this strain while drying using a home-built strain gauge. After drying, the threads remain at 70% strain. Strained threads (10 in total) were bundled together and affixed to the sample holder. Measurements of the unstrained state were performed on 10 pristine threads bundled together. Prior to measurement, the threads were aligned and dried.

vi. Molecular modeling

We provide a coarse-grain (CG) representation of the *Octopus bimaculoides* thread topology and structure by employing an elastic-polymer model with a memory of the thread native state. The native structure of the thread is constructed by connecting 29 aligned EGF-like units. The EGF-like unit was extracted from the crystal structure of the *neurogenic locus notch homolog* protein. The CG model is based on the spatial organization of the C_{α} atoms of the polypeptide. Each amino acid of the thread is represented by a simple monomeric unit with diameter $\sigma = 3.8\text{\AA}$. The monomers are covalently bonded to the first adjacent monomers along the polypeptide chain through a Finite-Extensible-Nonlinear-Elastic (FENE) potential. The monomers are subject to two short-range interactions: i) the steric hindrance interaction that prevents the chain from self-crossing, featured by Weeks-Chandler-Andersen (WCA) potential, and ii) the disulfide bond interaction that is modeled by a strong attractive Gaussian

potential. The elastic-polymer model of the thread is then provided with the bending and torsion potentials that are exerted to the triplets and quadruplets of successive monomers, respectively, whose reference angles are parametrized based on the thread native structure.

D. Results

i. Specimen description

Eggs from the California two-spot octopus (*Octopus bimaculoides*) were used. When laid, multiple octopus eggs are woven together and secured to a green cement (Fig. 4.2, A).

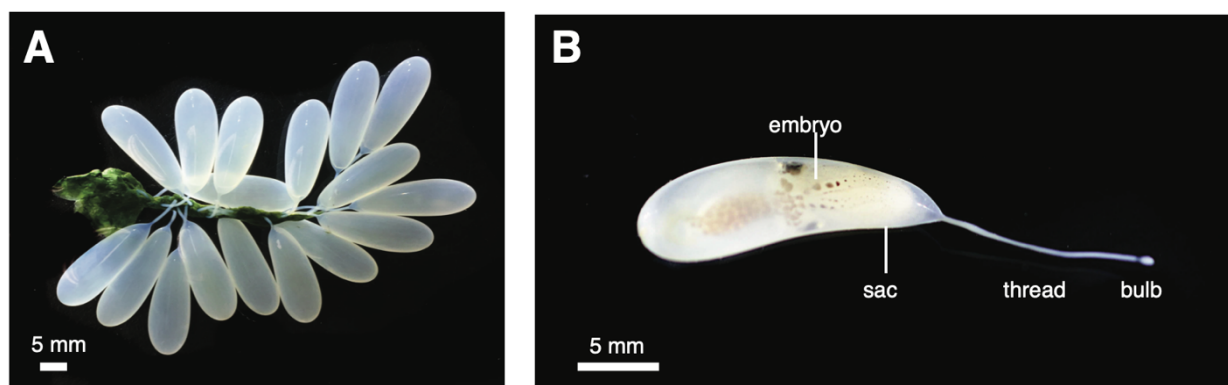


Figure 4.2. Dissecting microscope images of *Octopus bimaculoides* eggs. (a) Multiple eggs are attached to a central, green, cement stalk. (b) Individual eggs are surrounded by a white sac that tapers to a thread and terminates in a small bulb.

Individual eggs consist of a roughly pear-shaped embryo encased in a translucent white sheath. At the base of the eggs, the sheath tapers into an opaque white thread, which is generally 6 to 10 mm in length and 0.4 mm in diameter and terminates as bulb at the end opposite the embryo (Fig. 4.2, B).

The electron microscopy studies reveal the micron and submicron structure in the egg threads. SEM shows that the threads are approximately 400 μm in diameter (Fig. 4.3, A). In a relaxed state, the surface of the egg thread is wrinkled and amorphous (Fig. 4.3, B). Egg threads held at 100% strain, however, show a striated surface with ridges parallel to the axial

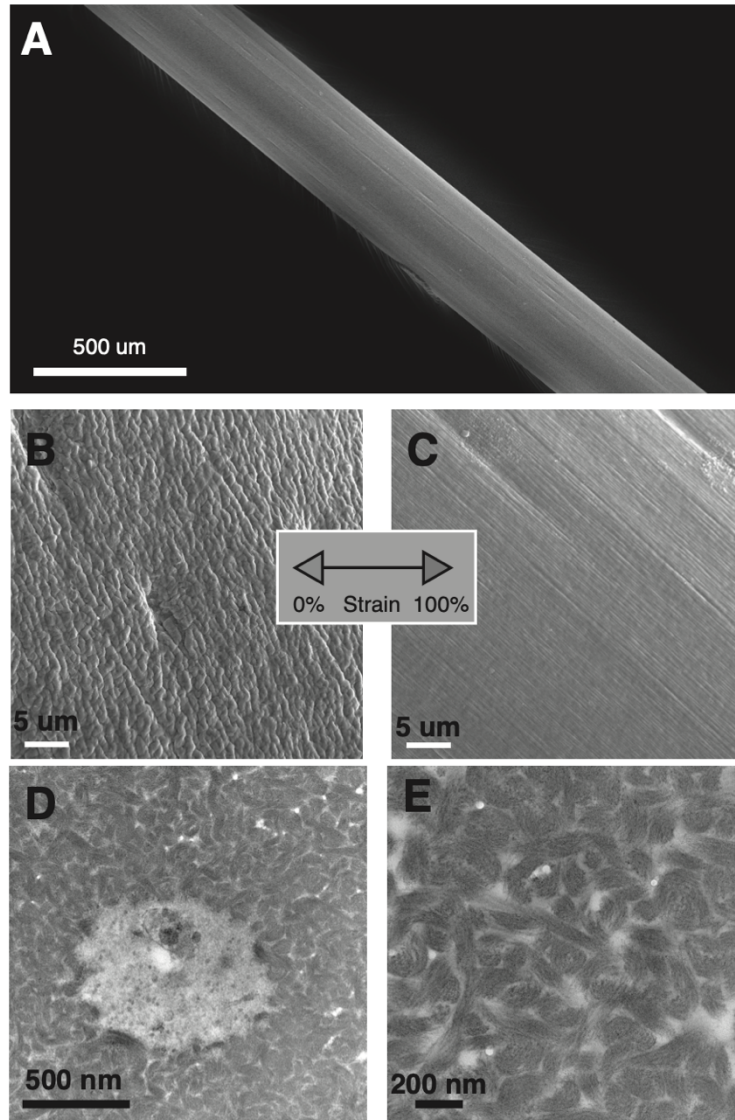


Figure 4.3. Electron microscopy images of octopus threads. (A) Low magnification SEM image of a single, unstrained, octopus thread. (B) SEM image of the surface of an unstrained octopus thread showing a coarse surface. (C) SEM image of the surface of an octopus thread pulled to 100% strain that shows ridges aligned with the long axis of the thread. (D) TEM image of a horizontal cross-section of an unstrained octopus thread. (E) Higher magnification TEM image of the fibrous bundles that are present in the core of the threads.

loading (Fig. 4.3, C). TEM images of transverse sections (Fig. 4.3, D,E) indicate that 200 nm thick fibrous bundles make up the bulk of the egg thread, and surround a small central void that likely forms from the secretion process. Within the bundles, fibers align in the same direction; however, globally, the bundles are isotropic.

ii. Biochemical characterization

Homogenization of the egg threads in Tris buffer at either room temperature or 95°C yields no discernable protein, as analyzed by SDS-PAGE (Supp. Fig. 4.S1, A, lanes 3 and 5). The addition of β -mercaptoethanol (β -ME) however, readily solubilizes the threads to generate a single major protein band (Supp. Fig. 4.S1, A, lane 4). Addition of heat increases the extraction efficiency (Supp. Fig. 4.S1, A, lane 2). The relative mass of the *octovafibrin* was determined from its mobility during SDS-PAGE (Supp. Fig. 4.S1,B). Partial sequences of *octovafibrin* were determined using MS/MS (Table 4.1).

Table 4.1. LC/MS/MS sequences of tryptic *octovafibrin* peptides

m/z	z	Sequence
895.052	3	ESKPYICEICAQGFFGDMCQSR
719.3269	2	VDGSHLYSSCANK
981.4711	2	KVHSHFEWVSCGTPYK
654.3021	3	ANGYICDCIEEYLGKR
746.8271	2	CNLGTCPEIDADK
649.2854	2	FGCLDGWTGER
460.2007	2	DSVGCEPR
1101.53	4	CSSLKGNVWVWLESSFELNYVATHLLDGMASQTDTWVGAK
472.2005	2	SYEGAMNR
663.8494	4	HVKNNLWYSEHPKPSSNVAFIGK
794.8041	2	NDGTCQDMEESFR
858.3525	2	CDCKPGYCGPLCTK
799.3462	2	FTCVCDSGYYGIR
597.2805	3	NGGICIIDGYEYKCK
428.8793	3	CKCPKPYFGK
436.8781	3	CTCKPAYVGPR
506.192	2	HYECSCR
593.2744	2	QGLSFVCSCK
872.6804	3	CRPGYLGTDCSTFDYCSDGPK
542.759	2	NSGTCYVVGK
830.915	2	KGSVYTCICQIGFK
440.6815	2	FTCHCR

These were then used to find the full-length sequence (Fig. 4.4, A) from the *Octopus bimaculoides* transcriptome. A C-type lectin binding domain, followed by 29 consecutive

EGF-like domains, ending in a C-terminal C-type lectin-binding domain (Fig. 4.4, B) define the full *octovafibrin* sequence.

The consensus sequence of the EGF-like domains shows highly conserved cysteines at the 5th, 10th, 16th, 25th, 27th, and 36th positions. A query of this sequence using PROSITE³⁵ indicates that none of the EGF domains are calcium binding. However, the large number of D/N residues in the 3rd position and Y/F residues in the 23rd position is partly consistent with the consensus calcium-binding EGF motif.³⁶ A template-based model of a representative EGF domain is also presented to illustrate the major and minor β -sheets along with the assembly of 29 consecutive EGF domains used for coarse-grain Molecular Dynamics (MD) simulations (Fig. 4.4,B). The similarity between the amino acid compositions of whole threads, the single major 135 kDa protein band extracted from the protein gel indicate that threads are primarily composed of *octovafibrin* assemblies (Supp. Fig. 4.S2,B). The amino acid content does show apparent discrepancy in the cysteine content between the threads, protein extract, and predicted sequence, however this is typical due to the hydrolytic susceptibility of cysteine which is dependent on its oxidation state.³⁷

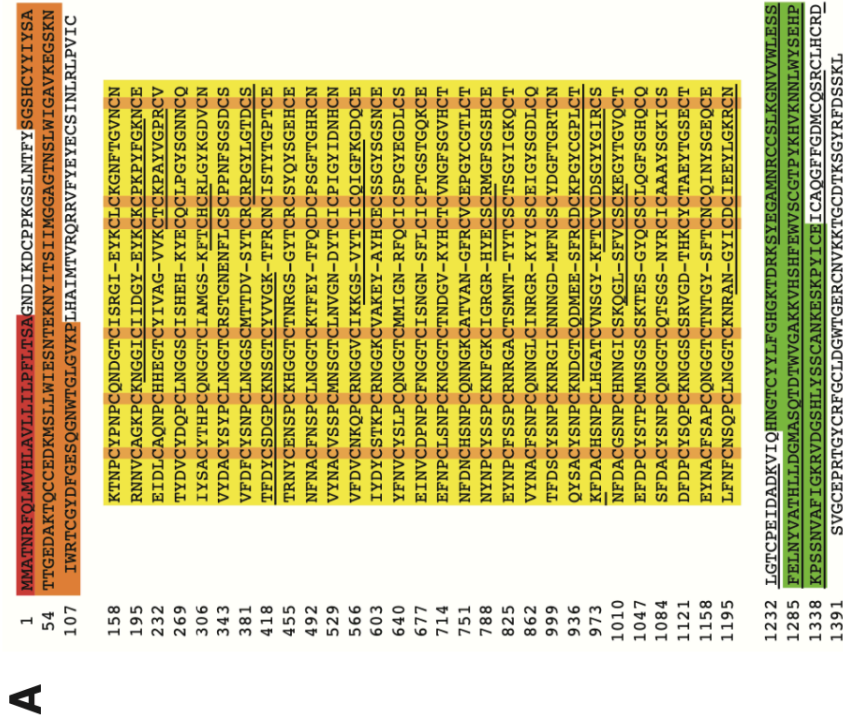


Figure 4.4 Sequence structure, and modelling of octovafibrin. (a) Aligned sequence *ctovafibrin* showing the secretory processing signal peptide in red, an N-terminal C-type Lectin binding domain in orange, 29 EGF domain repeats in yellow, and a C-terminal C-type Lectin binding domain in green. Cysteine residues are emphasized. Partial sequences from MS/MS are underlined. (b) Cartoon representation of *octovafibrin*, underneath which is the EGF sequence logo. Each disulfide is designated by color and given a letter. Blue: DS-A, C6-C16. Pink: DS-B, C27-C36. Orange: DS-C, C27-C36. Below, the template-based EGF molecular model is also shown with DS bonds depicted as yellow spheres. *Octovafibrin* is approximated by linking 29 identical EGF units (bottom).

iii. Mechanical Properties

When strained to failure, octopus egg threads exhibit three distinct regimes: (i) an initial elastic region to about 30% with a modulus of about 8.5 MPa, (ii) a softening region with a decrease in modulus to strains of about 100%, and (iii) a stiffening region that spans to nearly 140% strain whereupon the thread fails (Fig. 4.5, A).

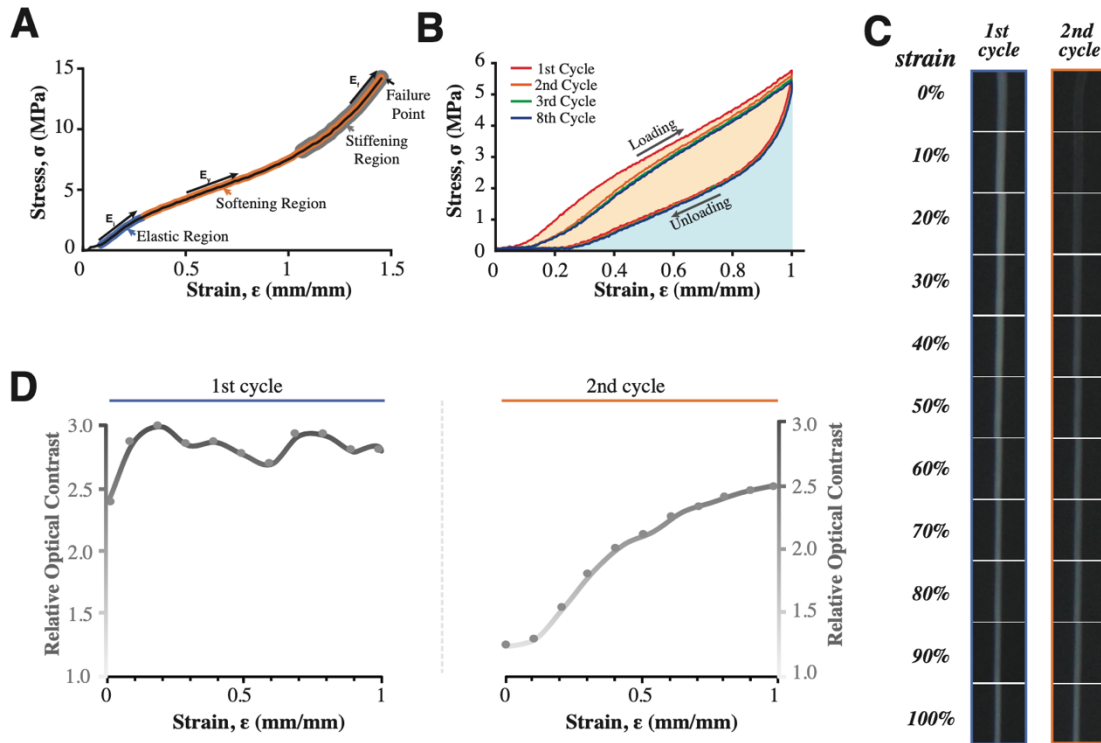


Figure 4.5. Mechanics and optical changes of threads under tensile loading. (A) typical stress-strain curve (strain rate = 1.0 min^{-1}) of an octopus thread shows an initial elastic region (blue), followed by a low modulus softening region (orange) and ending with a stiffening region (grey) prior to failure. (B) Typical stress behavior of an octopus thread under repeated cyclic load. The 1st (red), 2nd (orange), 3rd (green), and 8th (blue) cycles are shown. (C) The left column shows dissecting microscope images of pristine threads at different strain values during an initial load cycle, while the right column shows images of threads during the second load cycle. (D) Plots of relative optical (Weber) contrast as a function of strain during the first (left plot) and second (right plot) loading cycles.

When treating threads with EGTA, which is aimed at removing calcium, we observed no difference in mechanical behavior (Fig. 4.S3). Repeated cyclic loading of a single egg thread shows a decrease in modulus after the first cycle (Fig. 4.5,B). The average toughness

and hysteresis values of threads pulled to 100% strain and returned to 0% strain for 8 cycles are presented in Table 2. Pristine egg threads achieve an average toughness of 2.48 MJ/m³ with 53% hysteresis. During the second cycle the egg thread had a lower toughness of 2.12 MJ/m³ and 48% hysteresis.

Table 4.2. Average toughness and hysteresis values of octopus threads.

Cycle #	Toughness (MPa)	Hysteresis (%)
1	2.48 ± 0.48	52.5 ± 1.1
2	2.12 ± 0.45	48.2 ± 1.8
3	2.04 ± 0.49	47.0 ± 1.0
8	1.99 ± 0.43	46.7 ± 2.0

These values decreased slightly over subsequent cycles. This softening effect occurs after the first cycle and remains constant for the following cycles (2-8), whereas the unloading behavior is the same regardless of cycle number. The strain history, reduced modulus, and softening, are permanent as the thread properties remain unchanged after 24 hours of rest (Fig. 4.S3).

Optical changes in the egg threads were also observed (Fig. 4.5,C-D). Pristine egg threads are white and maintain a constant optical contrast through their first load cycle. Upon unloading, the egg threads become transparent, exhibiting little optical contrast. During the second (and subsequent) load cycles, the egg threads become white again, regaining the optical contrast. Upon unloading, the egg threads return to a transparent state.

Cyclic loading to increasing strains on a single egg thread, for a total of 12 cycles, is shown in Figure 4.S5. The first cycle ends at 10% strain, and the end point of each subsequent cycle is increased by 10% strain. A decrease in the modulus is observed in each subsequent cycle and thus leads to different loading paths (Figure 4.S5,A). An analogous chart constructed of cyclic loading curves of pristine threads pulled to different strain values is presented to show their loading and unloading paths (Fig. 4.S5, B). To probe the viscoelastic

properties of octopus threads, we performed a stress-relaxation experiment (Fig. 4.S5, C). We found that when a thread is held at 70% strain it relaxes to nearly 60% of the maximum stress achieved within 100 seconds.

We used WAXS to probe the strain-related changes in secondary structure. The 2D-WAXS patterns (Fig. 4.6, A,B) show that the threads are largely isotropic, with some anisotropy arising at low q for strained threads. The 1D radial profiles of unstrained and strained threads (Fig. 4.6C) identify three features at $q = 0.445, 0.653, \text{ and } 1.367 \text{ \AA}^{-1}$. We observe that, when strained, the feature at 1.367 \AA^{-1} has reduced intensity relative to the other features. The azimuthal intensity distribution shows that the feature at 0.445 \AA^{-1} aligns in the equatorial direction when the thread is strained.

Because WAXS identifies features at the nanoscale level, changes in secondary structure for EGF domains were modeled because of induced strain. We modeled each possible combination of disulfide (DS) bond reduction, which are portrayed in Figure 4.7A, and the relevant topological constraint is mapped on the lower-righthand corner of each panel.

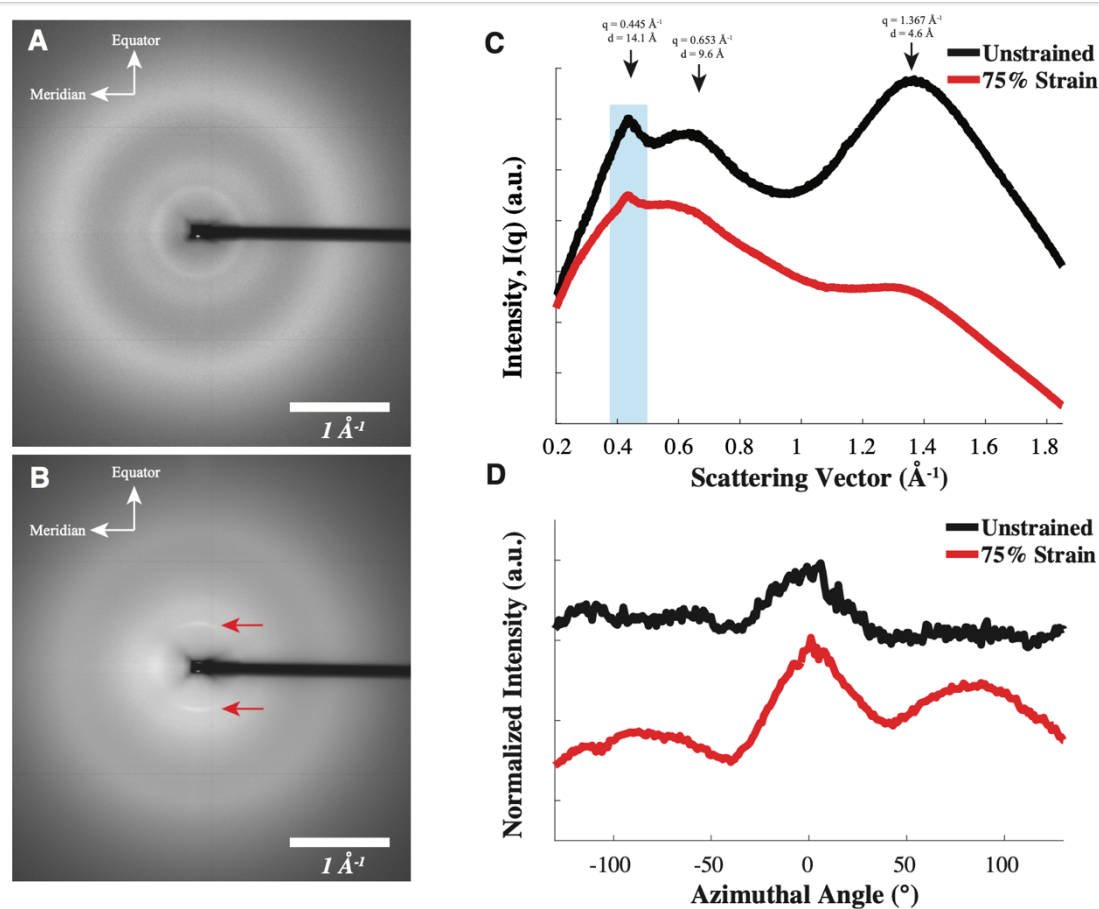


Figure 4.6. WAXS analysis of pristine and strained octopus threads. (A) 2D WAXS pattern of dry, unstrained, octopus threads. (B) 2D WAXS pattern of dried threads at 70% strain. (C) Integrated 1D radial intensity profiles of the unstrained threads (black) and strained threads (red). The shaded blue box indicates the area to generate (D) the 1D azimuthal profile of the peak at $q = 0.445 \text{ \AA}^{-1}$.

We modeled the effect of strain on the secondary structure of individual EGF domains (Fig. 4.7, B,C). When the disulfide (DS) bonds are intact, the minor β -sheet readily unfolds (Fig. 4.7, B, black), whereas the major β -sheet is less disrupted (Fig. 4.7B, red) due to the fact it is constrained by the disulfide bonds. The whole EGF domain partly unfolds (Fig. 4.7B, green). When the DS bonds are reduced, both the major and minor β -sheets unfold, resulting in denaturation of the entire EGF domain.

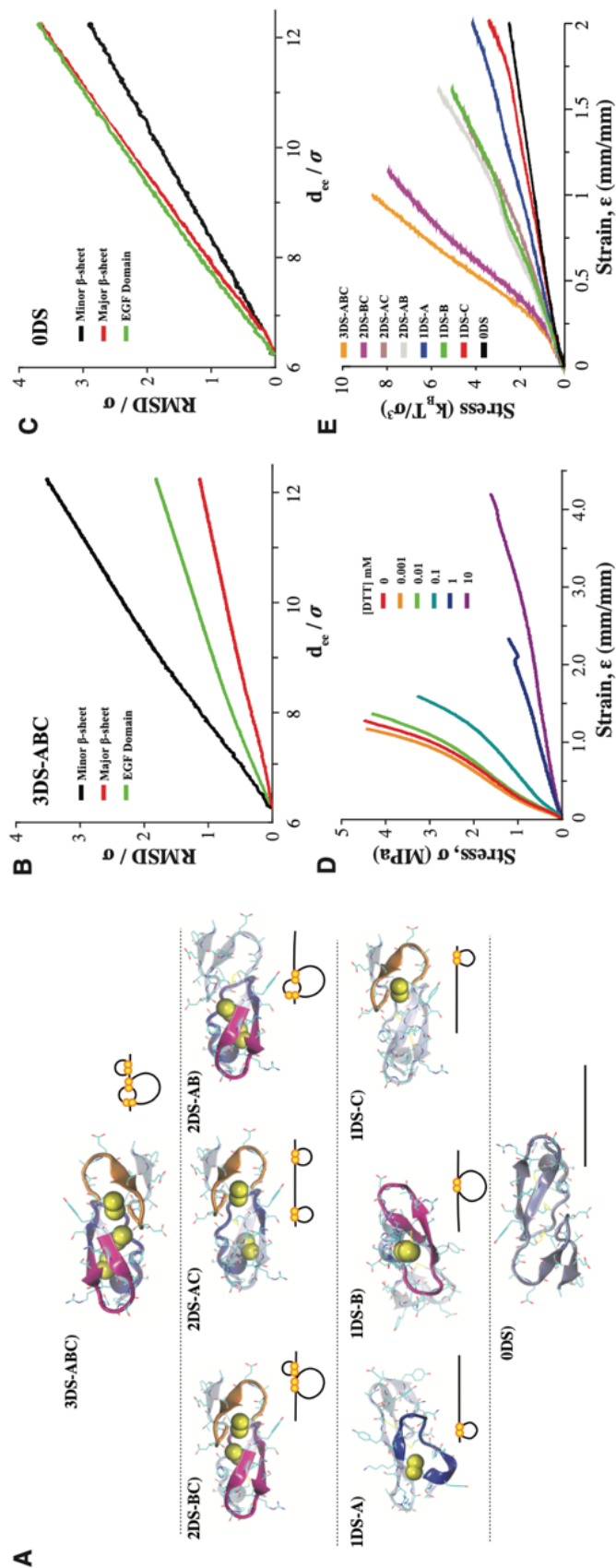


Figure 4.7. Mechanical effects of disulfide reduction. (A) Model and cartoon representations of each possible disulfide bond combination in the EGF domain. (B) CG-MD simulations of *octovafibrin* protein are performed to calculate the RMSD of an intact EGF domain showing the unfolding of the minor β -sheet (black), major β -sheet (red), and entire EGF domain (green) when under strain (50%). (C) Analogous plot to (B) when all disulfide bonds are reduced. (D) Stress-strain curves of octopus threads treated with increasing amounts of DTT (0 – 10mM). (E) CG-MD simulations are performed to characterize the stress strain behavior of individual *octovafibrin* molecules, initiated with 29 repeat EGF-domains.

To further study the effect of DS linkages, thread mechanics were tested after treatment with a wide range of the reducing agent dithiothreitol (DTT) concentrations (0.001mM to 10mM; Fig. 4.7D). Each thread is treated with DTT and loaded to failure. Low concentrations (0.001mM – 0.01mM) of DTT generated little effect on the mechanical behavior compared to native egg threads (Fig. 4.7D, red, orange, green curves). However, at higher concentrations of 0.1mM (teal), 1mM (blue), and 10mM (purple), both the modulus and stress at failure are significantly decreased, while the strain at failure is significantly increased. Threads treated with 0.1mM, 1mM, and 10mM DTT fail at approximate strains of 150%, 230%, and 400%, respectively, vs. native threads which typically fail at strains of 120%.

The effect of DS bonds reduction was computationally studied at the molecular level with CG-MD simulations. The strongest response occurs when all DS bonds of each EGF domains are intact (Fig. 4.7E, orange, 3DS-ABC). When only one DS bond is broken, there are disparate outcomes. When only the DS-A is broken there is a slight reduction in the mechanical properties (Fig. 4.7E, purple [2DS-BC]). However, when either DS-B or -C are broken, there is a significant decrease in modulus and increase in maximum strain (Fig. 4.7E, brown [2DS-AC], grey [2DS-AB]). The highest modulus for when two DS bonds are broken occurs for the case 1DS-B. The modulus is further reduced, and maximum strain increased for the case of 1DS-A and 1DS-C. The lowest modulus is observed when all DS bonds are reduced (case 0DS).

E. Discussion

The tethering egg threads of *Octopus bimaculoides* were found to be dominated by single protein named *octovafibrin*. Based on amino acid analysis, acid hydrolysis, and protein electrophoresis, at least 80% of the organic material in the egg threads is *octovafibrin*.

With 29 repeat EGF-like motifs, *Octovafibrin* enjoys a high degree of intramolecular crosslinking and joins the list of EGF-rich load-bearing ECM proteins. While it is tempting to compare its sequence to fibrillin, the lack of “beads-on-a-string” structures in our TEM (Fig. 4.3, D,E) and the absence of both calcium binding EGF-like and transforming growth factor binding (TB) domains (Fig. 4.4) makes such a comparison tenuous. Fibropellins, proteins that form the apical lamina layer in sea urchin embryos, appear to offer a better comparison. Both *octovafibrin* and fibropellin are present in the reproductive systems of marine invertebrates. Fibropellins also contain up to 21 EGF-like domains that are flanked by an N-terminal C1S-like³⁸ domain and a C-terminal avidin-like domain.³⁹ The flanking domains are thought to be involved in fibropellin assembly/oligomerization in order to form a fibrous network while the repeat EGF domains likely mediate a variety of protein-protein interactions.³⁸ This suggests that *octovafibrin* may assemble in an analogous way with the lectin-binding domains driving protein assembly.

Selectins, which also have terminal lectin-binding domains flanked by an EGF-like domains, may also provide some insight into the design of *octovafibrin*.⁴⁰ In selectins, the lectin binding domains facilitate adhesive interactions between proteins.⁴¹ This comparison also suggests catch bonds may contribute to the mechanical behavior of threads. Catch bonds have the property that their bond strength is increased when mechanical force is applied,⁴²

which creates a compelling situation in which *octovafibrin* align end-to-end in a way that enables interactions that strengthen as the thread is strained.

Our TEM (Fig. 4.3, E) showing that *octovafibrin* assembles to form curved fibrillar structures is morphologically consistent with previous work on a similar invertebrate octopus, *Octopus vulgaris*.⁴³ We take the observation of curved fibrils to indicate that *octovafibrin* has significant flexibility. This is reasonable given that repeat EGF domains have been shown to be flexible.^{41,44} The fibrous stacks also indicate the proteins assemble in a highly ordered fashion.

The mechanical behavior of octopus threads reflects internal structure as the strain to failure and viscoelastic response bear similarity to semicrystalline elastomers.^{45–48} The opacity of pristine threads is the result of semicrystalline nanostructures, where light is scattered at the boundaries between the stacked, amorphous, and void regions. We understand the optical changes as follows. As a pristine thread is loaded the ordered regions are disrupted and the fibers align, as captured by the changes in SEM (Fig. 4.3, B,C), but the threads remain opaque because they likely experience strain induced crystallization. Upon unloading, however, the fibers relax to an amorphous state that results in transparent threads. During the second loading cycle, the optical contrast increases with strain again due to strain-induced crystallization.

Although EGF domains are present in several load-bearing ECM proteins, there has been very little done to investigate strain-induced changes in secondary structure, and *octovafibrin*'s assembly into large monolithic fibers provides an excellent model to pursue this end. We attribute the WAXS features at $q = 1.367 \text{ \AA}^{-1}$ ($d = 4.6 \text{ \AA}$) and $q = 0.653 \text{ \AA}^{-1}$ ($d = 9.6 \text{ \AA}$) to β -sheets,⁴⁹ which are known to be present in EGF domains.²⁰ The source of the feature appearing at $q = 0.445 \text{ \AA}^{-1}$ is unclear, but it may be due to the dimensions of the EGF

domains as the d spacing ($d = 14.1 \text{ \AA}$) is close to the parameters previously measured for crystalline EGF.⁵⁰ Another possibility is that it is due to the distances between fibers. Two behaviors are evident by comparing WAXS of unstrained and strained threads. First, the azimuthal profile of the feature at $q = 0.445 \text{ \AA}^{-1}$ confirms that the proteins reorient under strain so that the EGF domains are packed in a tight, lateral fashion. Second, we find that, straining the threads reduces the relative intensity of the β -sheet features. This is, to our knowledge, the first indication that the secondary structure of EGF domains responds to mechanical tension. Our modeling efforts confirmed this behavior, indicating that the minor β -sheet is readily unfolded because it is not constrained by DS bonds (Fig. 4.7B). The dramatic reduction of the $q = 1.367 \text{ \AA}^{-1}$ indicates that the major β -sheet may also unfold, which would require the breaking of at least one of the DS bonds. Indeed, when all the disulfide bonds were reduced, the entire EGF domain (major and minor β -sheets) readily unfolded (Fig. 4.7C).

Taken together, we propose the following model to explain the mechanical behavior of octopus threads (Fig. 4.8). The individual fibers of pristine threads are an assembly of multiple *octovafibrin* molecules. Fibers are assembled and form many separate semicrystalline domains that are randomly oriented relative to one another. When strain is applied, the fibers are forced to realign in the axis of tension which disrupts the semicrystalline domains. As the thread is further strained, the EGF-like domains are deformed causing the β -sheets to unfold. Once unloaded, the fibers relax to an amorphous state. The response in subsequent strain cycles is then due only to the strain induced alignment as well as the deformation of the EGF domains. The lower modulus and reduced hysteresis of the second loading cycle is then a result of broken crystalline domains as well as increased alignment of the proteins with the axis of tension.

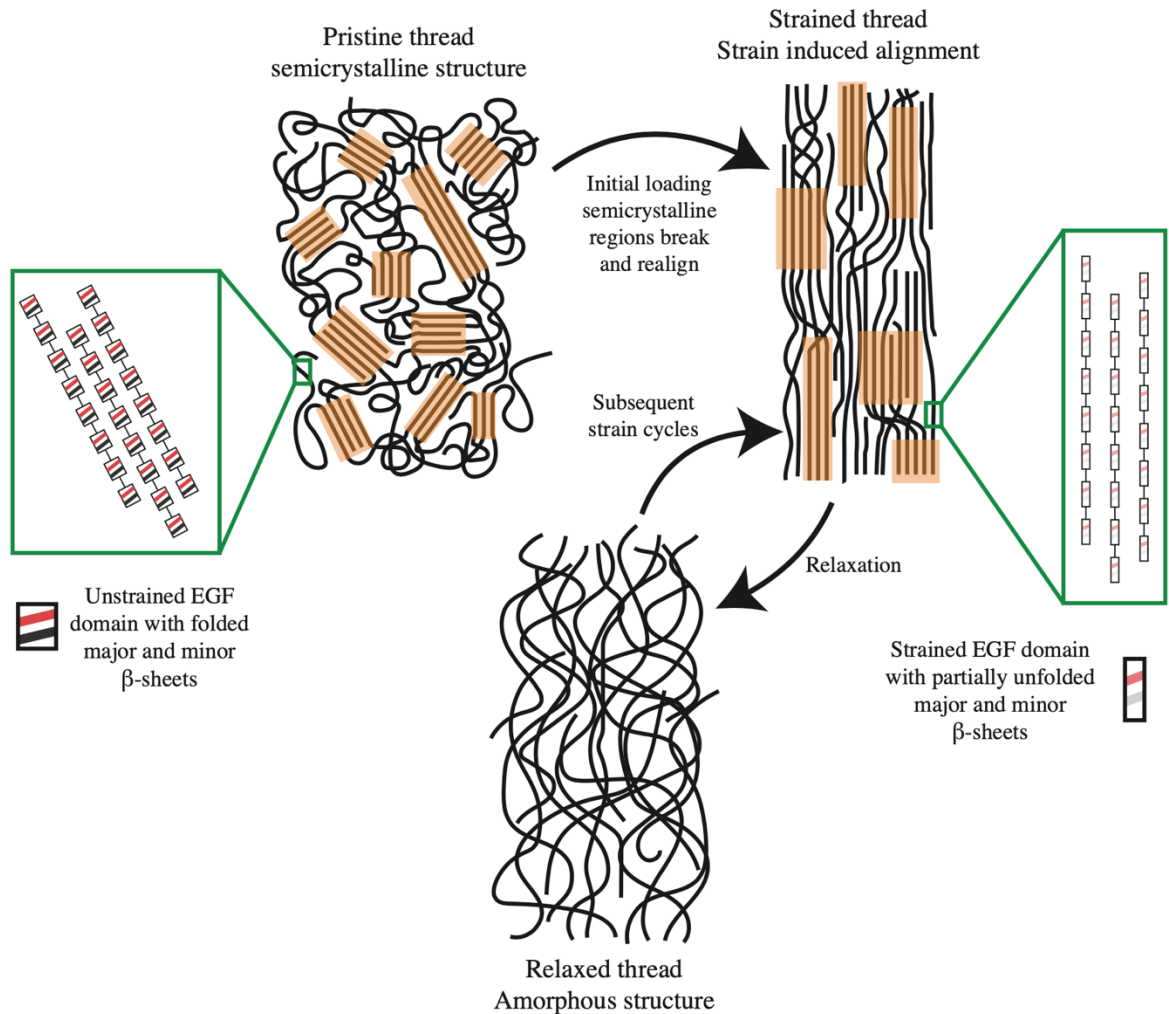


Figure 4.8. Cartoon model depicting molecular rearrangement and deformation during strain. Initially, the thread has domains made of highly aligned fibrils that are composed of several *octovafibrin* proteins. Prior to straining, the major and minor β -sheets of EGF domains (red and black stripes, respectively) are in-tact. Upon straining the aligned domains (orange) break and allow the fibers to reorient themselves with the axis of tension and resulting in strain-induced alignment (orange). Upon relaxation, the fibers relax to an amorphous state.

In light of the fact that intramolecular bonds can generate topologically complex motifs, yielding mechanically sturdy proteins⁵¹ and improved bulk mechanical properties³ this, we sought to analyze the effect of DS bond reduction on thread properties. Interestingly, we observe three regimes in both our experimental and simulated results. The simulation with all three bonds (orange) results in a stress-strain curve remarkably like that of the native

octopus egg threads. The fact that breaking DS-A (the bond between the first and third cysteine) (Fig. 7E, purple), indicates it contributes the least, mechanically speaking. This may be because the remaining DS bonds stabilize both ends of the major β -sheet and at that the portion of sequence constrained by DS-A has some overlap with the sequence constrained by DS-B. However, if either of the DS-B (brown) or DS-C (grey) bonds are broken, one end of the major β -sheet is destabilized, allowing it to unfold, results in a greater extensions due more hidden length being exposed.

DS-B alone (green), yields the highest modulus because it provides the largest constraint to the major β -sheet. When only either DS-A (blue) or the DS-C (red) remain, there is a further decrease in modulus and almost full extension, similar to the response when all DS bonds are broken (black). When fully reduced, the threads exhibit a low modulus and high extensibility, which is behavior typical of un-crosslinked elastomers. In this case we suggest the response is entirely due to the un tangling of protein molecules and the unfolding of β -sheets. Notably, reduced threads regain their original mechanics following equilibration into DTT free water (data not shown) suggesting they readily refold their stable EGF domains. It is unclear if the DS bonds on different EGF-like domains can be equally likely to be reduced by DTT due to their identical exposure. Further study is needed to determine if the various combination of DS bonds of the thread feature different susceptibility to reduction.

The present study's modeling shows that, once elongated, the repeat EGF-like domains result in a high-persistence length polymer. This may be partially responsible for the increased modulus as persistence in length is proportional to Young's modulus.⁵² The possibility of intermolecular DS bonds that would also increase the modulus cannot be

excluded. However, it is reasonable to assume that the EGF-like domains are folded properly, meaning intermolecular DS bonds would be uncommon.

Egg thread mechanics conceivably plays an important role the life history of the octopus. Once the eggs are laid, the mother octopus tirelessly broods her eggs for several months until they hatch, whereupon she expires. She constantly moves about her confined den preening and flushing the developing eggs with jets of water. The mechanical properties of egg threads and cases provide protection against potential predator attack, drag and lift by turbulent/laminar flow, the massaging motions of the mother, and various pathogens⁵³ and must persist during a long brooding period. While we focused on the egg threads in this study for experimental simplicity, both the egg case and threads appear to be formed during a single continuous process and are biochemically seamless.

F. Conclusion

We have studied the biochemical, ultrastructural, and mechanical properties of the reproductive egg threads of *Octopus bimaculoides*. Threads appear to be made of a single protein, *octovafibrin*, that has 29 repeat EGF-like domains flanked on either side by lectin binding domains. The proteins assemble into semi-ordered fibrous bundles. Pristine threads exhibit a response similar to semicrystalline elastomers. The reduction of disulfide bonds results greatly reduced modulus but far greater extension.

This study confirms that intramolecular crosslinks significantly improve the bulk mechanical properties of polymeric systems and may inform on the rational design of new SCNPs. We also conclude that EGF domains are deformable and appear to act like small springs. The DS bond between the first and third cysteine of EGF appears to contribute the most to the mechanical response of these domains. The material appears to be designed with

semicrystalline domains that break sacrificially during the first strain cycle as the fibers experience strain alignment. Of particular interest is whether these results can be similarly observed in other EGF-rich systems, such as fibrillin, which may help understand the use of EGF-like domains in mechanical systems.

G. References

- (1) Tillet, G.; Boutevin, B.; Ameduri, B. Chemical Reactions of Polymer Crosslinking and Post-Crosslinking at Room and Medium Temperature. *Prog. Polym. Sci.* **2011**, *36* (2), 191–217. <https://doi.org/10.1016/j.progpolymsci.2010.08.003>.
- (2) Tonelli, A. E. Effects of Crosslink Density and Length on the Number of Intramolecular Crosslinks (Defects) Introduced into a Rubbery Network. *Polymer (Guildf)*. **1974**, *15* (4), 194–196. [https://doi.org/10.1016/0032-3861\(74\)90031-7](https://doi.org/10.1016/0032-3861(74)90031-7).
- (3) Galant, O.; Bae, S.; Silberstein, M. N.; Diesendruck, C. E. Highly Stretchable Polymers: Mechanical Properties Improvement by Balancing Intra- and Intermolecular Interactions. *Adv. Funct. Mater.* **2020**, *30* (18), 1–8. <https://doi.org/10.1002/adfm.201901806>.
- (4) Frisch, H.; Tuten, B. T.; Barner-Kowollik, C. Macromolecular Superstructures: A Future Beyond Single Chain Nanoparticles. *Isr. J. Chem.* **2020**, *60* (1–2), 86–99. <https://doi.org/10.1002/ijch.201900145>.
- (5) Rief, M.; Gautel, M.; Oesterhelt, F.; Fernandez, J. M.; Gaub, H. E. Reversible Unfolding of Individual Titin Immunoglobulin Domains by AFM. *Science (80-.)*. **1997**, *276* (5315), 1109–1112. <https://doi.org/10.1126/science.276.5315.1109>.
- (6) Marszalek, P. E.; Lu, H.; Li, H.; Carrion-Vazquez, M.; Oberhauser, A. F.; Schulten, K.; Fernandez, J. M. Mechanical Unfolding Intermediates in Titin Modules. *Nature* **1999**, *402* (6757), 100–103. <https://doi.org/10.1038/47083>.
- (7) Schröder, C. U.; Heinz, A.; Majovsky, P.; Mayack, B. K.; Brinckmann, J.; Sippl, W.; Schmelzer, C. E. H. Elastin Is Heterogeneously Cross-Linked. *J. Biol. Chem.* **2018**, *293* (39), 15107–15119. <https://doi.org/10.1074/jbc.RA118.004322>.
- (8) Du, N.; Yang, Z.; Liu, X. Y.; Li, Y.; Xu, H. Y. Structural Origin of the Strain-Hardening of Spider Silk. *Adv. Funct. Mater.* **2011**, *21* (4), 772–778. <https://doi.org/10.1002/adfm.201001397>.
- (9) Chen, H.; Fu, H.; Zhu, X.; Cong, P.; Nakamura, F.; Yan, J. Improved High-Force Magnetic Tweezers for Stretching and Refolding of Proteins and Short DNA. *Biophys. J.* **2011**, *100* (2), 517–523. <https://doi.org/10.1016/j.bpj.2010.12.3700>.
- (10) Lehmann, K.; Shayegan, M.; Blab, G. A.; Forde, N. R. Optical Tweezers Approaches for Probing Multiscale Protein Mechanics and Assembly. *Front. Mol. Biosci.* **2020**, *7* (October), 1–10. <https://doi.org/10.3389/fmolb.2020.577314>.
- (11) Najafi, S. Irreversible Topological Transition of a Stretched Superhelix: The Interplay of Chiralities. *Soft Matter* **2019**, *15* (31), 6258–6262. <https://doi.org/10.1039/C9SM01027K>.
- (12) Kremer, K.; Grest, G. S. Dynamics of Entangled Linear Polymer Melts: A Molecular-dynamics Simulation. *J. Chem. Phys.* **1990**, *92* (8), 5057–5086. <https://doi.org/10.1063/1.458541>.
- (13) Galera-Prat, A.; Gómez-Sicilia, A.; Oberhauser, A. F.; Cieplak, M.; Carrión-Vázquez, M. Understanding Biology by Stretching Proteins: Recent Progress. *Curr. Opin. Struct. Biol.* **2010**, *20* (1), 63–69. <https://doi.org/10.1016/j.sbi.2010.01.003>.
- (14) Galloway, J. Helical Imperative: Paradigm of Growth, Form and Function. In *Encyclopedia of Life Sciences*; John Wiley & Sons, Ltd: Chichester, UK, 2010; pp 1–11. <https://doi.org/10.1002/9780470015902.a0003673.pub2>.
- (15) Wada, H.; Netz, R. R. Stretching Helical Nano-Springs at Finite Temperature.

- Europhys. Lett.* **2007**, 77 (6), 68001. <https://doi.org/10.1209/0295-5075/77/68001>.
- (16) Yogurtcu, O. N.; Wolgemuth, C. W.; Sun, S. X. Mechanical Response and Conformational Amplification in α -Helical Coiled Coils. *Biophys. J.* **2010**, 99 (12), 3895–3904. <https://doi.org/10.1016/j.bpj.2010.10.002>.
- (17) Bolsover, S. R.; Hyams, J. S.; Shephard, E. A.; White, H. A.; Wiedemann, C. G. *Cell Biology*, 2nd ed.; John Wiley & Sons, Inc.: Hoboken, NJ, USA, 2003. <https://doi.org/10.1002/047146158X>.
- (18) Wolgemuth, C. W.; Sun, S. X. Elasticity of α -Helical Coiled Coils. *Phys. Rev. Lett.* **2006**, 97 (24), 248101. <https://doi.org/10.1103/PhysRevLett.97.248101>.
- (19) Engel, J. Common Structural Motifs in Proteins of the Extracellular Matrix. *Curr. Opin. Cell Biol.* **1991**, 3 (5), 779–785. [https://doi.org/10.1016/0955-0674\(91\)90050-9](https://doi.org/10.1016/0955-0674(91)90050-9).
- (20) Wouters, M. A.; Rigoutsos, I.; Chu, C. K.; Feng, L. L.; Sparrow, D. B.; Dunwoodie, S. L. Evolution of Distinct EGF Domains with Specific Functions. *Protein Sci.* **2005**, 14 (4), 1091–1103. <https://doi.org/10.1110/ps.041207005>.
- (21) Campbell, I. D.; Bork, P. Epidermal Growth Factor-like Modules. *Curr. Opin. Struct. Biol.* **1993**, 3 (3), 385–392. [https://doi.org/10.1016/S0959-440X\(05\)80111-3](https://doi.org/10.1016/S0959-440X(05)80111-3).
- (22) Jensen, S. A.; Robertson, I. B.; Handford, P. A. Dissecting the Fibrillin Microfibril: Structural Insights into Organization and Function. *Structure* **2012**, 20 (2), 215–225. <https://doi.org/10.1016/j.str.2011.12.008>.
- (23) Kielty, C. M. Fell-Muir Lecture: Fibrillin Microfibrils: Structural Tensometers of Elastic Tissues? *Int. J. Exp. Pathol.* **2017**, 98 (4), 172–190. <https://doi.org/10.1111/iep.12239>.
- (24) Sherratt, M. J.; Baldock, C.; Haston, J. L.; Holmes, D. F.; Jones, C. J. P.; Shuttleworth, C. A.; Wess, T. J.; Kielty, C. M. Fibrillin Microfibrils Are Stiff Reinforcing Fibres in Compliant Tissues. *J. Mol. Biol.* **2003**, 332 (1), 183–193. [https://doi.org/10.1016/S0022-2836\(03\)00829-5](https://doi.org/10.1016/S0022-2836(03)00829-5).
- (25) Lee, S. S. J.; Knott, V.; Jovanović, J.; Harlos, K.; Grimes, J. M.; Choulier, L.; Mardon, H. J.; Stuart, D. I.; Handford, P. A. Structure of the Integrin Binding Fragment from Fibrillin-1 Gives New Insights into Microfibril Organization. *Structure* **2004**, 12 (4), 717–729. <https://doi.org/10.1016/j.str.2004.02.023>.
- (26) Kuo, C. L.; Isogai, Z.; Keene, D. R.; Hazeki, N.; Ono, R. N.; Sengle, G.; Bächinger, H. P.; Sakai, L. Y. Effects of Fibrillin-1 Degradation on Microfibril Ultrastructure. *J. Biol. Chem.* **2007**, 282 (6), 4007–4020. <https://doi.org/10.1074/jbc.M606370200>.
- (27) Mikulska, K.; Strzelecki, J.; Balter, A.; Nowak, W. Nanomechanical Unfolding of α -Neurexin: A Major Component of the Synaptic Junction. *Chem. Phys. Lett.* **2012**, 521, 134–137. <https://doi.org/10.1016/j.cplett.2011.11.033>.
- (28) Oberhauser, A. F.; Marszalek, P. E.; Erickson, H. P.; Fernandez, J. M. The Molecular Elasticity of the Extracellular Matrix Protein Tenascin. *Nature* **1998**, 393 (6681), 181–185. <https://doi.org/10.1038/30270>.
- (29) Forsythe, J. W.; Hanlon, R. T. Effect of Temperature on Laboratory Growth, Reproduction and Life Span of Octopus *Bimaculoides*. *Mar. Biol.* **1988**, 98 (3), 369–379. <https://doi.org/10.1007/BF00391113>.
- (30) Tao, A. R.; DeMartini, D. G.; Izumi, M.; Sweeney, A. M.; Holt, A. L.; Morse, D. E. The Role of Protein Assembly in Dynamically Tunable Bio-Optical Tissues. *Biomaterials* **2010**, 31 (5), 793–801. <https://doi.org/10.1016/j.biomaterials.2009.10.038>.

- (31) Rosenfeld, J.; Capdevielle, J.; Guillemot, J. C.; Ferrara, P. In-Gel Digestion of Proteins for Internal Sequence Analysis after One- or Two-Dimensional Gel Electrophoresis. *Anal. Biochem.* **1992**, *203* (1), 173–179. [https://doi.org/10.1016/0003-2697\(92\)90061-B](https://doi.org/10.1016/0003-2697(92)90061-B).
- (32) Hellman, U.; Wernstedt, C.; Góñez, J.; Heldin, C. H. Improvement of an “in-Gel” Digestion Procedure for the Micropreparation of Internal Protein Fragments for Amino Acid Sequencing. *Analytical Biochemistry.* 1995, pp 451–455. <https://doi.org/10.1006/abio.1995.1070>.
- (33) Bolger, A. M.; Lohse, M.; Usadel, B. Trimmomatic: A Flexible Trimmer for Illumina Sequence Data. *Bioinformatics* **2014**, *30* (15), 2114–2120. <https://doi.org/10.1093/bioinformatics/btu170>.
- (34) Haas, B. J.; Papanicolaou, A.; Yassour, M.; Grabherr, M.; Blood, P. D.; Bowden, J.; Couger, M. B.; Eccles, D.; Li, B.; Lieber, M.; MacManes, M. D.; Ott, M.; Orvis, J.; Pochet, N.; Strozzi, F.; Weeks, N.; Westerman, R.; William, T.; Dewey, C. N.; Henschel, R.; LeDuc, R. D.; Friedman, N.; Regev, A. De Novo Transcript Sequence Reconstruction from RNA-Seq Using the Trinity Platform for Reference Generation and Analysis. *Nat. Protoc.* **2013**, *8* (8), 1494–1512. <https://doi.org/10.1038/nprot.2013.084>.
- (35) Sigrist, C. J. A.; Cerutti, L.; de Castro, E.; Langendijk-Genevaux, P. S.; Bulliard, V.; Bairoch, A.; Hulo, N. PROSITE, a Protein Domain Database for Functional Characterization and Annotation. *Nucleic Acids Res.* **2010**, *38* (suppl_1), D161–D166. <https://doi.org/10.1093/nar/gkp885>.
- (36) Boswell, E. J.; Kurniawan, N. D.; Downing, A. K. Calcium-Binding EGF-Like Domains. In *Encyclopedia of Inorganic and Bioinorganic Chemistry*; John Wiley & Sons, Ltd: Chichester, UK, 2011; pp 1–19. <https://doi.org/10.1002/9781119951438.eibc0513>.
- (37) Inglis, A. S.; Liu, T.-Y. The Stability of Cysteine and Cystine during Acid Hydrolysis of Proteins and Peptides. *J. Biol. Chem.* **1970**, *245* (1), 112–116. [https://doi.org/10.1016/S0021-9258\(18\)63428-3](https://doi.org/10.1016/S0021-9258(18)63428-3).
- (38) Bisgrove, B. W.; Raff, R. A. The SpEGF III Gene Encodes a Member of the Fibropellins: EGF Repeat-Containing Proteins That Form the Apical Lamina of the Sea Urchin Embryo. *Dev. Biol.* **1993**, *157* (2), 526–538. <https://doi.org/10.1006/dbio.1993.1155>.
- (39) Yanai, I. An Avidin-like Domain That Does Not Bind Biotin Is Adopted for Oligomerization by the Extracellular Mosaic Protein Fibropellin. *Protein Sci.* **2005**, *14* (2), 417–423. <https://doi.org/10.1110/ps.04898705>.
- (40) Springer, T. A. Structural Basis for Selectin Mechanochemistry. *Proc. Natl. Acad. Sci. U. S. A.* **2009**, *106* (1), 91–96. <https://doi.org/10.1073/pnas.0810784105>.
- (41) Lou, J.; Yago, T.; Klopocki, A. G.; Mehta, P.; Chen, W.; Zarnitsyna, V. I.; Bovin, N. V.; Zhu, C.; McEver, R. P. Flow-Enhanced Adhesion Regulated by a Selectin Interdomain Hinge. *J. Cell Biol.* **2006**, *174* (7), 1107–1117. <https://doi.org/10.1083/jcb.200606056>.
- (42) Thomas, W. E.; Vogel, V.; Sokurenko, E. Biophysics of Catch Bonds. *Annu. Rev. Biophys.* **2008**, *37* (1), 399–416. <https://doi.org/10.1146/annurev.biophys.37.032807.125804>.
- (43) Boletzky, S. Nos Connaissances Actuelles Sur Le Développement Des Octopodes.

- Vie Milieu* **1978**, 28/2, 85–120.
- (44) Baldock, C.; Siegler, V.; Bax, D. V.; Cain, S. A.; Mellody, K. T.; Marson, A.; Haston, J. L.; Berry, R.; Wang, M. C.; Grossmann, J. G.; Roessle, M.; Kielty, C. M.; Wess, T. J. Nanostructure of Fibrillin-1 Reveals Compact Conformation of EGF Arrays and Mechanism for Extensibility. *Proc. Natl. Acad. Sci. U. S. A.* **2006**, 103 (32), 11922–11927. <https://doi.org/10.1073/pnas.0601609103>.
- (45) Deplace, F.; Wang, Z.; Lynd, N.; Hotta, A.; Rose, J.; Hustad, P.; Tian, J.; Ohtaki, H.; Coates, G.; Shimizu, F.; Hirokane, K.; Yamada, F.; Shin, Y. W.; Rong, L.; Zhu, J.; Toki, S.; Hsiao, B.; Fredrickson, G.; Kramer, E. Processing-Structure-Mechanical Property Relationships of Semicrystalline Polyolefin-Based Block Copolymers. *J. Polym. Sci. Part B Polym. Phys.* **2010**, 48 (13), 1428–1437. <https://doi.org/10.1002/polb.21969>.
- (46) Men, Y.; Rieger, J.; Strobl, G. Role of the Entangled Amorphous Network in Tensile Deformation of Semicrystalline Polymers. *Phys. Rev. Lett.* **2003**, 91 (9), 1–4. <https://doi.org/10.1103/PhysRevLett.91.095502>.
- (47) Al-Hussein, M.; Strobl, G. Strain-Controlled Tensile Deformation Behavior of Isotactic Poly(1-Butene) and Its Ethylene Copolymers. *Macromolecules* **2002**, 35 (22), 8515–8520. <https://doi.org/10.1021/ma020831k>.
- (48) Hong, K.; Rastogi, A.; Strobl, G. A Model Treating Tensile Deformation of Semicrystalline Polymers: Quasi-Static Stress-Strain Relationship and Viscous Stress Determined for a Sample of Polyethylene. *Macromolecules* **2004**, 37 (26), 10165–10173. <https://doi.org/10.1021/ma049174h>.
- (49) Kreplak, L.; Doucet, J.; Dumas, P.; Briki, F. New Aspects of the α -Helix to β -Sheet Transition in Stretched Hard α -Keratin Fibers. *Biophys. J.* **2004**, 87 (1), 640–647. <https://doi.org/10.1529/biophysj.103.036749>.
- (50) Rao, Z.; Handford, P.; Mayhew, M.; Knott, V.; Brownlee, G. G.; Stuart, D. The Structure of a Ca²⁺-Binding Epidermal Growth Factor-like Domain: Its Role in Protein-Protein Interactions. *Cell* **1995**, 82 (1), 131–141. [https://doi.org/10.1016/0092-8674\(95\)90059-4](https://doi.org/10.1016/0092-8674(95)90059-4).
- (51) Sikora, M.; Sułkowska, J. I.; Cieplak, M. Mechanical Strength of 17 134 Model Proteins and Cysteine Slipknots. *PLoS Comput. Biol.* **2009**, 5 (10), 1–15. <https://doi.org/10.1371/journal.pcbi.1000547>.
- (52) Broedersz, C. P.; MacKintosh, F. C. Modeling Semiflexible Polymer Networks. *Rev. Mod. Phys.* **2014**, 86 (3), 995–1036. <https://doi.org/10.1103/RevModPhys.86.995>.
- (53) Vieites, J. M. *Handbook of Pathogens and Diseases in Cephalopods*; Gestal, C., Pascual, S., Guerra, Á., Fiorito, G., Vieites, J. M., Eds.; Springer International Publishing: Cham, 2019. <https://doi.org/10.1007/978-3-030-11330-8>.

H. Supplementary figures for Chapter 4

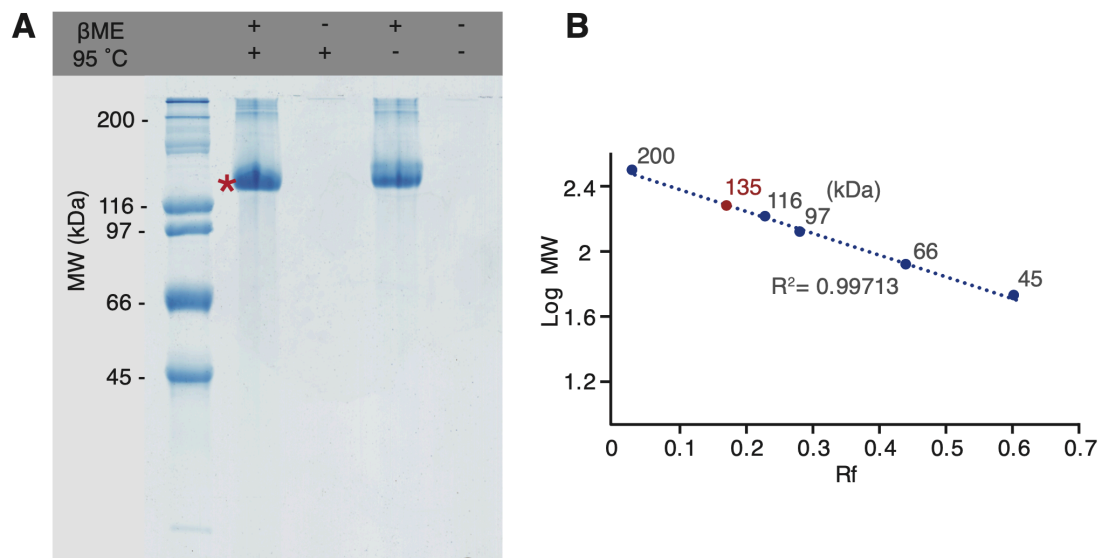


Figure 4.S1. Identification and molecular weight determination of octovafibrin. A) SDS-PAGE illustrating the effect of β -mercaptoethanol and heating on the extraction of octovafibrin. B) plot of $\log(\text{MW})$ vs relative migration distance (R_f) used to determine the molecular weight of octovafibrin.

A

Single Thread Characteristics	
Length (mm)	12 ± 1.5
Diameter (mm)	0.21 ± 0.02
Wet wt. (mg)	0.407 ± 0.012
Dry wt. (mg)	0.350 ± 0.012
Protein (% wt.)	70.1 ± 7.5
Water (% wt.)	13.7 ± 4.7
Calcium (% wt.)	0.034 ± 0.0004
Other (% wt.)	~ 16.8

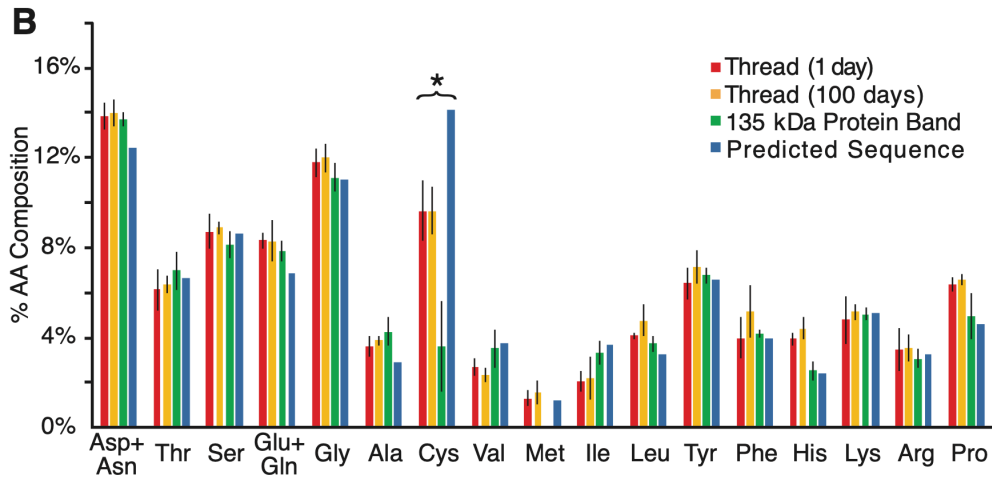


Figure 4.S2. Typical characteristics of octopus threads. A) Table of average thread length, diameter, and weight, as well as protein, water, and calcium content. B) Chart comparing the amino acid profile of hole threads at 1 day, 100 days, the purified 135kDa protein band, and the predicted octovafibrin sequence.

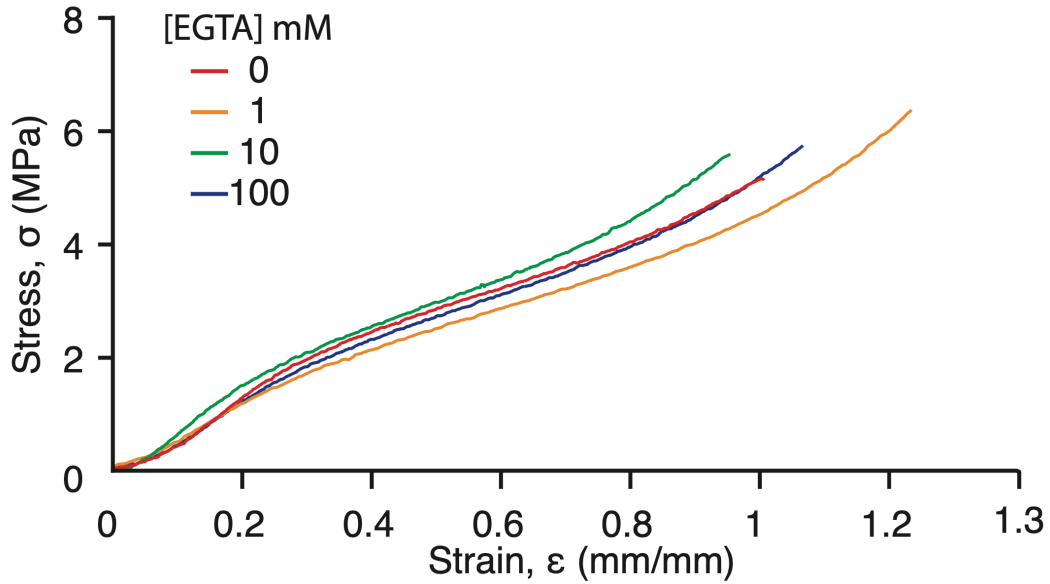


Figure 4.S3. Effect of EGTA treatment on the tensile behavior of threads. Threads were treated with different concentrations of EGTA to remove calcium ions.

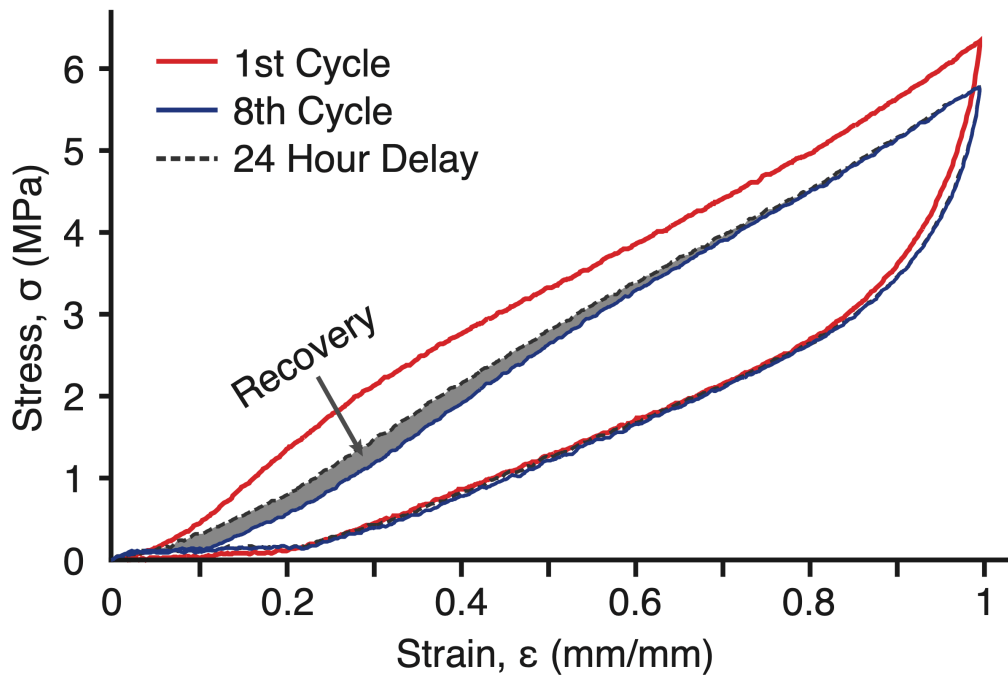


Figure 4.S4. Recovery of octopus threads. Cyclic loading behavior of pristine threads (red), threads having undergone prior cyclic loading (blue), and threads having been given 24 hours to recover (black dashed). The shaded area indicates recovery.

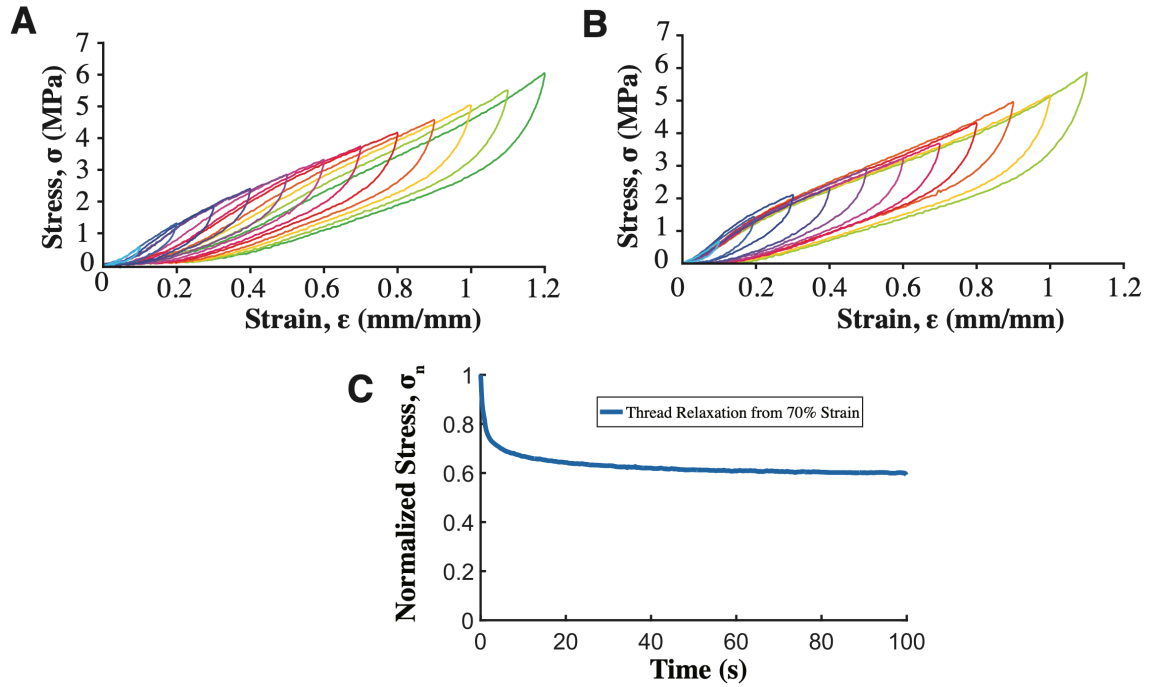


Figure 4.S5. Cyclic loading to increasing strain and stress relaxation of threads. A) Stress-strain behavior of a single thread subjected to repeated cyclic loading to increased strain values. B) Stress-strain behavior of pristine threads pulled to identical strain values as in A. C) Stress relaxation behavior of threads held at 70% strain.

Chapter 5

Conclusions, future directions, and closing remarks

This series of experiments highlight the multifunctionality and importance of low complexity proteins in each system studied. The conclusions and future directions are summarized below.

A. Mussel adhesion

Experiments on peptoid analogs of low-complexity mussel-derived peptides, whose sequences are rich in glycine, lysine, and either phenylalanine, tyrosine, or Dopa, show that the protein backbone can have dramatic effects on deposition and mechanical behavior, despite the sequences being intrinsically disordered. Peptoid backbones are intrinsically more hydrophobic because linkage of functional groups to the backbone nitrogen removes the hydrophilic amide N-H. In contrast to their peptide counterparts, which deposit as hydrated multilayers, the peptoids used in this study deposit as monolayers which allows for differentiation between cohesive and adhesive failure. Symmetrically deposited phe-peptoids generated significant cohesion which supports the importance of cation- π interactions. Additionally, the increased hydrophobicity and inability to form backbone-backbone interactions facilitated greatly improved adhesive and cohesive behavior for Dopa substituted peptoids. This is due the eviction of water from the surface as well as reduction of water near Dopa moieties and is particularly useful considering the negative effect of water on adhesion.¹

This study has important broad implications. When a protein is indicated to be intrinsically disordered, it may lead one to believe that the protein backbone plays a minimal role in its behavior and thus does not need to be considered in a biomimetic design. The results in our investigation suggest otherwise. The three sidechains tested in peptoids have dramatically different outcomes: phenylalanine peptoids provides weak adhesion but strong cohesion, tyrosine peptoids behave remarkably like their peptide counterparts, and dopa peptoids provide much stronger adhesion and cohesion than their peptide counterparts. These results show that the sidechains do define much of the mechanical performance, but that the backbone may be critical to providing the correct context to achieve this performance. Indeed, the more hydrophobic peptoid backbone offers some advantage as it seems to allow dopa residues to form strong cohesive and adhesive bonds.

An obvious extension of this study would be to probe the mechanical properties of the peptide and peptoid films. Atomic force microscopy and quartz crystal microbalance studies would provide excellent complementary information to provide values of film viscosity, modulus, thickness, and density.² Furthermore, the manner in which the peptoid backbone affects the oxidation and metal binding properties of Dopa would be interesting to understand. Oxidized Dopa-peptoid analogs may be unable to tautomerize in the same fashion as their peptide counterparts due to the amide linkage. The oxidative behavior of small molecule catechols as well as mfp-3 was previously studied with potentiometric and spectrophotometric methods.³ The effect of oxidation may also be understood by testing the peptoids at higher pH, similar to the study of mfp-3 by Yu, *et al.*⁴ Finally, to test if the outcomes in this study may be generalized, these experiments can be replicated with other mfp-inspired sequences.

One set of possible sequences are the low- and neutral-pI blocks found in mfp-5 that were studied by Wei, *et al.*⁵

B. *Glycera* jaw

We identified a major protein component of *Glycera dibranchiata* jaws, herein named MultiTasking Protein (MTP), and was showed it to have a low complexity sequence consisting of approximately 50% glycine and 30% histidine residues. The sequence does not appear to be random as it consists mainly of GGH repeat motifs. Despite its low complexity, MTP displays several functions *in vitro*. It the sequence yields high-capacity copper binding which then induces both coacervate formation and provides the ability to induce Dopa oxidation. The metal binding appears to form a square planar complex with a Cu²⁺ center and four imidazole ligands. Coacervation, in this case most likely driven by charge-charge interactions, creates hydrophobic droplets. The metal binding, phase separation, and oxidative properties of MTP appear to work in symphony to generate melanized protein nanosheets at the air-water interface. The model proposed for film formation is as follows: copper binding induces MTP to form coacervate droplets which accumulate spread at the air-water interface due to their hydrophobic properties. Free Dopa molecules then partition into these droplets whereupon oxidation to dopaquinone is facilitated by bound copper ions and available oxygen. Dopaquinone then polymerizes to solidify both the MTP as well as create a second melanin network. These films also exhibit sufficient mechanical strength for tensile fibers to be drawn from the surface.

MTP provides an intriguing case study among low-complexity proteins. The sequence of MTP is a combination of two residues that are commonly found in low-complexity

structural proteins: glycine and histidine. High glycine content may mediate elasticity and strength as is suggested with glycine-rich cell wall proteins.⁶ Metal bound histidine may provide hardness and/or stiffness as is observed in *Nereis* jaws and bioinspired systems.^{7,8} The behavior of MTP further corroborates the structural function Gly and His and its sequence simplicity provides an achievable template for biomimicry.

This being the first investigation into MTP, there are a few obvious follow-up studies. Interfacial rheometry clearly shows that copper-bound MTP assembles at the air-water interface to form a viscoelastic film. Langmuir-Blodgett troughs are ideal for studying the self-assembly of molecules at surfaces.⁹ Using this technique changes in surface pressure as a function of metal ions, salt, or Dopa concentration may be measured.¹⁰ Additionally, Langmuir troughs enable the deposition of films onto surfaces, which can then be analyzed by other techniques such as X-ray scattering¹¹ or atomic force microscopy (AFM).¹²

The studies outlined here can also be repeated with randomized sequences to see which functions rely on the GGH tripeptide as well as investigating the effect of peptide length. MTP is a relatively small protein, meaning synthetic plasmid constructs are affordable. A separate question is whether the effects observed in this study are specific to copper binding. As mentioned previously, the *Nereis* jaw protein (NJP) has a similar amino acid profile, but *Nereis* jaws are enriched with zinc rather than copper. Metal binding induced differential behavior of these proteins: MTP binding with Cu^{2+} results in liquid-liquid phase separation, and NJP binding to Zn^{2+} yields insoluble amyloid-like fibrils.¹³ Given their sequence similarity an AFM investigation would indicate whether this Zn^{2+} -induced fibrillization also occurs with MTP.

Further work can also be done to characterize the biochemistry of *Glycera* jaws. It is unlikely that MTP is the only protein that is present in the jaws. Indeed, the transcriptome revealed another sequence rich in glycine and histidine that included an observed signal peptide (Figure 5.1).

Putative *Glycera* jaw protein

```
MRWLT GSAAL LLLLL CVSLV TAHVV EVRGK RGRGG HQGHR GHGGG YQGGH
                                                                 50
GAGGH GQGGH GGQGG HAAGF WGVEG HGAGQ GGHAG DVAGH GGYDA GGGFK
                                                                 100
GGDDG GHQGG HGGHG GHEEG YGKAG HGEHG GQGHG GQGHG GQGHG GQEHG
                                                                 150
GQGHG GQVGH EGHAG HEAGH GGGGQ GAAKE AGHAD AGHAD KLLLL INRGV
                                                                 200
AGHGG HGGGH GGGHG GGHGG
                                                                 220
```

Figure 5.1. Transcriptome sequence of a second glycine/histidine rich protein from *Glycera* jaw. Underlined residues are the predicted signal peptide.

This sequence displays a more diverse set of amino acids, containing hydrophobic residues as well as several instances in which histidine residues are substituted with glutamine, resulting in GGQGH repeats beginning at residue 130. The choice of glutamine is interesting as glutamine is critical to the activity CBM33 polysaccharide oxygenases, which have copper centers.¹⁴

Another vein of investigation lies in the formation of the jaws. In most organisms, melanin is synthesized in cellular structures called melanocytes. These cells typically synthesize melanin granules packaged in organelles called melanosomes using the enzyme tyrosinase. The melanosomes can then be transported to areas in need of pigmentation. For example, melanosomes are transported via microtubule to keratinocytes to provide hair color. In *Glycera* jaws, it is unclear where the Gly/His rich proteins are incorporated – are they present in the melanocytes or are they synthesized elsewhere? Fluorescence *in situ* hybridization (FISH) would provide an excellent approach to answer this question. Melanocytes are readily identified with light microscopy due to their inherent pigmentation. Thus, by using RNA probes for Gly/His rich sequences, it would be a simple matter to determine whether these proteins are also synthesized in the same structures as melanin.

A further line of inquiry is to determine whether glycine/histidine rich proteins exist in other jawed polychaetes. This question is motivated by the obvious similarities between MTP and NJP, despite the samples coming from separate suborders (Glyceriformia and Nereidiformia, respectively). There are jawed polychaetes more closely related to *Glycera*. *Hemipodia* is one such genus that is also in the suborder Glyceriformia. They have jaws which are morphologically similar to *Glycera* and they are readily found in the beaches of Santa Barbara. Additionally, worms in the family Goniadidae are equipped with rows of jet-black jaw elements. X-ray microanalyses performed on jaws from *Goniada maculata* revealed high magnesium and calcium content rather than copper.¹⁵ The question remains for both *Goniada* and *Hemipodia* jaws: do they share similar mechanical and biochemical properties to *Glycera* jaws? Such a study might resemble the 1973 investigation by Voss-Foucart.¹⁶ A notable observation in their study is that all jaw specimens analyzed, even those from the more distant

order Eunicida, have amino acid profiles strongly biased towards glycine. Scale worms (family Polynoidae) may also be included in this study as their jaws have not been subject to biochemical characterization. A reasonable starting point of this study would be to generate amino acid profiles for each species in addition to their transcriptomes. These transcriptomes may similarly be searched for sequences that code for glycine- and/or histidine-rich proteins. This would provide information into the phyletic relationships between worms and inform on the importance of glycine-rich proteins in load-bearing systems.

C. Octopus eggs

The experiments on *Octopus bimaculoides* threads elucidate their biochemical, structural, and mechanical properties. The primary structural component, herein named octovafibrin, is a highly repetitive protein that has a core sequence of 29 repeat EGF-like motifs and lectin binding domains at the N- and C- termini. The bulk threads exhibit tensile properties similar to semicrystalline elastomers. This behavior appears to arise from the self-assembly of octovafibrin as well as the molecular deformation of individual EGF-like domains. Octovafibrin assembles into fibrous bundles that are largely oriented randomly to one another. When strained the bundles are irreversibly disrupted, which dissipates energy, as they align with the axis of tension. During this process EGF-like domains also dissipate energy as their internal β -sheets unfold in response to strain.

The broader implications of these experiments are twofold. First, they underscore the effect intramolecular crosslinks may have on bulk mechanical properties. The incorporation of intramolecular crosslinks provides a Young's modulus of 8.51MPa, which is over three times greater than the Young's modulus of threads whose intramolecular crosslinks have been

removed, at 2.74MPa. A similar effect is observed in recent work by Galant *et al.*¹⁷ which provides a synthetic foundation for this approach. One disadvantage of their synthetic construct is that mechanical improvements were only observed at temperatures above the glass transition temperature (80°C for their study). Octopus threads, on the other hand, enjoy the mechanical advantage at room temperature. Thus, the architecture of octovafibrin, which has many small and intramolecularly cross-linked domains that are covalently linked in a chain provides an intriguing model for biomimicry.

Second, these experiments provide the first insight into the mechanical behavior of EGF-like domains and thus the role they play in the numerous extracellular matrix proteins in which they are found.¹⁸ To our knowledge there have been no investigations as to how individual EGF-like domains deform under strain. Although single molecule AFM force studies on proteins with EGF-like domains exist, their analyses largely ignored the contribution of EGF-like domains,^{19,20} although this may be due to insufficient forces.²¹ The WAXS analysis of octopus threads demonstrates the EGF-like domains deform under tension and can be understood as stiff springs with some capacity to dissipate energy.

For future experiments, an investigation into post-translational modifications of octovafibrin would be beneficial. EGF-like domains are often glycosylated²² and, although in EGF domains the function is unclear, glycosylation is known to affect assembly of other proteins.^{23,24} Furthermore, C-type lectin binding domains are defined by their carbohydrate binding ability.²⁵ With the latter in mind, evidence of glycosylation would support the hypothesis that selectin-like catch bonds are used by octovafibrin. Detection of such modifications would require chromatographic and mass spectrometric methods as is outlined in the a protocol for glycoprotein analysis provided by Jensen, *et al.*²⁶

The wide angle X-ray scattering (WAXS) data indicates that the β -sheets unfold during strain, but it is unclear whether this process is reversible. To answer this question, dynamic WAXS measurements of individual threads can be collected at a synchrotron source in a similar fashion to the small-angle X-ray scattering (SAXS) measurements collected by Krauss *et al* on mussel threads.²⁷ Additionally, performing scattering experiments on a separate EGF-rich system would indicate whether the behavior EGF domains in octopus threads may be generalized. An ideal system to investigate this would be fibrillin-rich mammalian zonular filaments. Their strain behavior has been monitored with SAXS in several different studies,²⁸⁻³¹ but we find that WAXS analysis, oddly, not been performed. Zonular filaments are composed of fibrillin-rich microfibrils, which are indispensable elastic structures found connective tissue.²⁹ Their principal component is fibrillin, which is an important protein in the ECM that contains over 45 EGF-like domains. Individual fibrillin molecules show reversible behavior to extensions of 50% but this behavior has been attributed to the flexibility of EGF-like linker domains.³⁰ Applying the principles elucidated from octopus threads, it is possible that the EGF-like domains are additionally deformed in this regime to provide increased stiffness and energy dissipation to guard against greater extensions that result in irreversible deformation.

An investigation into the processing and deposition of octopus egg cases would be tremendously worthwhile. In 1903, Bergmann showed that *Octopus* egg cases are formed by the coalescence of granular secretions of the follicular epithelium.³² Many systems in biology are processed as liquid crystals and polarized light microscopy would be ideal to discern if this is the case for octovafibrin.

Although we have investigated the egg cases of an incirrate octopus, there is very little known about the biochemistry of their cirrate counterparts. For incirrate octopuses (such as *Octopus bimaculoides*), the oviducal gland secretes the cement material that forms the central stalk to which eggs are attached. In cirrate octopuses, however, the oviducal gland secretes a hard material that encases each egg.³³ It is unclear, however, if the oviducal secretion represents the entirety of the eggcase or if it simply provides a coating for an underlying viscoelastic matrix that is analogous to what is observed for *Octopus bimaculoides*. Thus, it would be informative to investigate the mechanical properties and biochemistry of cirrate octopus eggs to see if any general conclusions may be drawn.

Finally, we offer a possible method to synthetically mimic this system. This approach would involve a process similar to what is described for typical single-chain nanoparticle syntheses.^{34,35} The critical difference would be installing reactive end groups whose chemistry is orthogonal to the crosslinking that occurs during chain collapse.³⁶ Depending on the chemistry of the reactive end groups, polymerization of the SCNPs can then either be performed in solution prior to film preparation or could be done *in situ* to form a mesoscale pearl necklace, similar to octovafibrin.

D. Final remarks

Nature's ability to form complicated structures with outstanding properties has always been, and will always be, admired by humanity. The apparent complexity of biology, however, will act as a deterrent to many of those who would otherwise be inspired. Hopefully the information provided here has shown that biology is also capable of recognizing the utility of finding simple solutions to complex problems.

E. References

- (1) Lee, B. P.; Messersmith, P. B.; Israelachvili, J. N.; Waite, J. H. Mussel-Inspired Adhesives and Coatings. *Annu. Rev. Mater. Res.* **2011**, *41*, 99–132. <https://doi.org/10.1146/annurev-matsci-062910-100429>.
- (2) Lubarsky, G. V.; Davidson, M. R.; Bradley, R. H. Hydration-Dehydration of Adsorbed Protein Films Studied by AFM and QCM-D. *Biosens. Bioelectron.* **2007**, *22* (7), 1275–1281. <https://doi.org/10.1016/j.bios.2006.05.024>.
- (3) Mirshafian, R.; Wei, W.; Israelachvili, J. N.; Waite, J. H. α,β -Dehydro-Dopa: A Hidden Participant in Mussel Adhesion. *Biochemistry* **2016**, *55* (5), 743–750. <https://doi.org/10.1021/acs.biochem.5b01177>.
- (4) Yu, J.; Wei, W.; Menyo, M. S.; Masic, A.; Waite, J. H.; Israelachvili, J. N. Adhesion of Mussel Foot Protein-3 to TiO₂ Surfaces: The Effect of PH. *Biomacromolecules* **2013**, *14* (4), 1072–1077. <https://doi.org/10.1021/bm301908y>.
- (5) Wei, W.; Yu, J.; Gebbie, M. A.; Tan, Y.; Martinez Rodriguez, N. R.; Israelachvili, J. N.; Waite, J. H. Bridging Adhesion of Mussel-Inspired Peptides: Role of Charge, Chain Length, and Surface Type. *Langmuir* **2015**, *31* (3), 1105–1112. <https://doi.org/10.1021/la504316q>.
- (6) Molecular, P.; Division, B. Glycine-Rich Proteins. **2005**, *120* (7), 169–174.
- (7) Broomell, C. C.; Mattoni, M. A.; Zok, F. W.; Waite, J. H. Critical Role of Zinc in Hardening of Nereis Jaws. *J. Exp. Biol.* **2006**, *209* (16), 3219–3225. <https://doi.org/10.1242/jeb.02373>.
- (8) Khare, E.; Holten-Andersen, N.; Buehler, M. J. Transition-Metal Coordinate Bonds for Bioinspired Macromolecules with Tunable Mechanical Properties. *Nat. Rev. Mater.* **2021**, *6* (5), 421–436. <https://doi.org/10.1038/s41578-020-00270-z>.
- (9) Ariga, K.; Yamauchi, Y.; Mori, T.; Hill, J. P. 25th Anniversary Article: What Can Be Done with the Langmuir-Blodgett Method? Recent Developments and Its Critical Role in Materials Science. *Adv. Mater.* **2013**, *25* (45), 6477–6512. <https://doi.org/10.1002/adma.201302283>.
- (10) You, S. S.; Rashkov, R.; Kanjanaboos, P.; Calderon, I.; Meron, M.; Jaeger, H. M.; Lin, B. Comparison of the Mechanical Properties of Self-Assembled Langmuir Monolayers of Nanoparticles and Phospholipids. *Langmuir* **2013**, *29* (37), 11751–11757. <https://doi.org/10.1021/la4020064>.
- (11) Sukhorukov, G. B.; Feigin, L. A.; Montrel, M. M.; Sukhorukov, B. I. X-Ray and Infrared Study of Langmuir-Blodgett Films of the Complexes between Nucleic Acids and Aliphatic Amines. *Thin Solid Films* **1995**, *259* (1), 79–84. [https://doi.org/10.1016/0040-6090\(94\)06414-8](https://doi.org/10.1016/0040-6090(94)06414-8).
- (12) Nayak, A.; Suresh, K. A. Mechanical Properties of Langmuir-Blodgett Films of a Discogen-DNA Complex by Atomic Force Microscopy. *J. Phys. Chem. B* **2009**, *113* (12), 3669–3675. <https://doi.org/10.1021/jp806600g>.
- (13) Broomell, C. C.; Chase, S. F.; Laue, T.; Waite, J. H. Cutting Edge Structural Protein from the Jaws of Nereis Virens. *Biomacromolecules* **2008**, *9* (6), 1669–1677. <https://doi.org/10.1021/bm800200a>.
- (14) Hemsworth, G. R.; Taylor, E. J.; Kim, R. Q.; Gregory, R. C.; Lewis, S. J.; Turkenburg, J. P.; Parkin, A.; Davies, G. J.; Walton, P. H. The Copper Active Site of CBM33 Polysaccharide Oxygenases. *J. Am. Chem. Soc.* **2013**, *135* (16), 6069–6077.

- <https://doi.org/10.1021/ja402106e>.
- (15) Gibbs, p. e.; Bryan, g. w. A Note on the Elemental Composition of the Jaws of *Goniada Maculata* (Polychaeta: Goniadidae). *J. Mar. Biol. Assoc. United Kingdom* **1980**, *60* (2), 541–542. <https://doi.org/10.1017/S0025315400028563>.
 - (16) Voss-Foucart, M. F.; Fonce-Vignaux, M. T.; Jeuniaux, C. Systematic Characters of Some Polychaetes (Annelida) at the Level of the Chemical Composition of the Jaws. *Biochem. Syst. Ecol.* **1973**, *1* (2), 119–122. [https://doi.org/10.1016/0305-1978\(73\)90025-2](https://doi.org/10.1016/0305-1978(73)90025-2).
 - (17) Galant, O.; Bae, S.; Silberstein, M. N.; Diesendruck, C. E. Highly Stretchable Polymers: Mechanical Properties Improvement by Balancing Intra- and Intermolecular Interactions. *Adv. Funct. Mater.* **2020**, *30* (18), 1–8. <https://doi.org/10.1002/adfm.201901806>.
 - (18) Engel, J. Common Structural Motifs in Proteins of the Extracellular Matrix. *Curr. Opin. Cell Biol.* **1991**, *3* (5), 779–785. [https://doi.org/10.1016/0955-0674\(91\)90050-9](https://doi.org/10.1016/0955-0674(91)90050-9).
 - (19) Mikulska, K.; Strzelecki, J.; Balter, A.; Nowak, W. Nanomechanical Unfolding of α -Neurexin: A Major Component of the Synaptic Junction. *Chem. Phys. Lett.* **2012**, *521*, 134–137. <https://doi.org/10.1016/j.cplett.2011.11.033>.
 - (20) Oberhauser, A. F.; Marszalek, P. E.; Erickson, H. P.; Fernandez, J. M. The Molecular Elasticity of the Extracellular Matrix Protein Tenascin. *Nature* **1998**, *393* (6681), 181–185. <https://doi.org/10.1038/30270>.
 - (21) Jollymore, A.; Lethias, C.; Peng, Q.; Cao, Y.; Li, H. Nanomechanical Properties of Tenascin-X Revealed by Single-Molecule Force Spectroscopy. *J. Mol. Biol.* **2009**, *385* (4), 1277–1286. <https://doi.org/10.1016/j.jmb.2008.11.038>.
 - (22) Wouters, M. A.; Rigoutsos, I.; Chu, C. K.; Feng, L. L.; Sparrow, D. B.; Dunwoodie, S. L. Evolution of Distinct EGF Domains with Specific Functions. *Protein Sci.* **2005**, *14* (4), 1091–1103. <https://doi.org/10.1110/ps.041207005>.
 - (23) Zuo, R.; Liu, R.; Olguin, J.; Hudalla, G. A. Glycosylation of a Nonfibrillizing Appendage Alters the Self-Assembly Pathway of a Synthetic β -Sheet Fibrillizing Peptide. *J. Phys. Chem. B* **2021**, *125* (24), 6559–6571. <https://doi.org/10.1021/acs.jpcc.1c02083>.
 - (24) Bosques, C. J.; Imperiali, B. The Interplay of Glycosylation and Disulfide Formation Influences Fibrillization in a Prion Protein Fragment. *Proc. Natl. Acad. Sci. U. S. A.* **2003**, *100* (13), 7593–7598. <https://doi.org/10.1073/pnas.1232504100>.
 - (25) Drickamer, K. C-Type Lectin-like Domains. *Curr. Opin. Struct. Biol.* **1999**, *9* (5), 585–590. [https://doi.org/10.1016/S0959-440X\(99\)00009-3](https://doi.org/10.1016/S0959-440X(99)00009-3).
 - (26) Jensen, P. H.; Karlsson, N. G.; Kolarich, D.; Packer, N. H. Structural Analysis of N- and O-Glycans Released from Glycoproteins. *Nat. Protoc.* **2012**, *7* (7), 1299–1310. <https://doi.org/10.1038/nprot.2012.063>.
 - (27) Krauss, S.; Metzger, T. H.; Fratzl, P.; Harrington, M. J. Self-Repair of a Biological Fiber Guided by an Ordered Elastic Framework. *Biomacromolecules* **2013**, *14* (5), 1520–1528. <https://doi.org/10.1021/bm4001712>.
 - (28) Haston, J. L.; Engelsen, S. B.; Roessle, M.; Clarkson, J.; Blanch, E. W.; Baldock, C.; Kielty, C. M.; Wess, T. J. Raman Microscopy and X-Ray Diffraction, a Combined Study of Fibrillin-Rich Microfibrillar Elasticity. *J. Biol. Chem.* **2003**, *278* (42), 41189–41197. <https://doi.org/10.1074/jbc.M212854200>.
 - (29) Sherratt, M. J.; Wess, T. J.; Baldock, C.; Ashworth, J.; Purslow, P. P.; Shuttleworth,

- C. A.; Kielty, C. M. Fibrillin-Rich Microfibrils of the Extracellular Matrix: Ultrastructure and Assembly. *Micron* **2001**, *32* (2), 185–200.
[https://doi.org/10.1016/S0968-4328\(99\)00082-7](https://doi.org/10.1016/S0968-4328(99)00082-7).
- (30) Sherratt, M. J.; Baldock, C.; Haston, J. L.; Holmes, D. F.; Jones, C. J. P.; Shuttleworth, C. A.; Wess, T. J.; Kielty, C. M. Fibrillin Microfibrils Are Stiff Reinforcing Fibres in Compliant Tissues. *J. Mol. Biol.* **2003**, *332* (1), 183–193.
[https://doi.org/10.1016/S0022-2836\(03\)00829-5](https://doi.org/10.1016/S0022-2836(03)00829-5).
- (31) Wright, D. M.; Duance, V. C.; Wess, T. J.; Kielty, C. M.; Purslow, P. P. The Supramolecular Organisation of Fibrillin-Rich Microfibrils Determines the Mechanical Properties of Bovine Zonular Filaments. *J. Exp. Biol.* **1999**, *202* (21), 3011–3020.
- (32) Bergmann, W. Untersuchungen Über Die Eibildung Bei Anneliden Und Cephalopoden. *Z. Wiss. Zool.* **1903**, *73*, 278–301.
- (33) Boletzky, S. Encapsulation of Cephalopod Embryos - a Search for Functional Correlations. *Am. Malacol. Bull.* **1986**, *4*, 217–227.
- (34) Frisch, H.; Tuten, B. T.; Barner-Kowollik, C. Macromolecular Superstructures: A Future Beyond Single Chain Nanoparticles. *Isr. J. Chem.* **2020**, *60* (1–2), 86–99.
<https://doi.org/10.1002/ijch.201900145>.
- (35) Chen, J.; Garcia, E. S.; Zimmerman, S. C. Intramolecularly Cross-Linked Polymers: From Structure to Function with Applications as Artificial Antibodies and Artificial Enzymes. *Acc. Chem. Res.* **2020**, *53* (6), 1244–1256.
<https://doi.org/10.1021/acs.accounts.0c00178>.
- (36) Wang, F.; Diesendruck, C. E. Advantages and Limitations of Diisocyanates in Intramolecular Collapse. *Polym. Chem.* **2017**, *8* (24), 3712–3720.
<https://doi.org/10.1039/c7py00712d>.